USING LACTOSE AND ULTRASOUND TO DELIVER CHEMOTHERAPEUITCS

by

Rand Hasan Abusamra

A Thesis presented to the Faculty of the
American University of Sharjah
College of Engineering
In Partial Fulfillment
of the Requirements
for the Degree of

Master of Science in
Biomedical Engineering

Sharjah, United Arab Emirates

May 2019

Approval Signatures

We, the undersigned, approve the Master's Thesis of Rand Hasan Abusamra

Thesis Title: Using Lactose and Ultrasound to deliver chemotherapeutics.

Signature **Date of Signature** (dd/mm/yyyy)

_____ _____

Dr. Ghaleb Husseini
Professor, Department of Chemical Engineering
Thesis Advisor

_____ _____

Dr. Nahid Awad
Senior Research Associate, Biosciences and Bioengineering Research Institute (BBRI)
Thesis Committee Member

_____ _____

Dr. Amer Zakaria
Assistant Professor, Department of Electrical Engineering
Thesis Committee Member

_____ _____

Dr. Hasan Al-Nashash
Director, Biomedical Engineering Graduate Program

_____ _____

Dr. Lotfi Romdhane
Associate Dean for Graduate Affairs and Research
College of Engineering

_____ _____

Dr. Naif Darwish
Acting Dean, College of Engineering

_____ _____

Dr. Mohamed El-Tarhuni
Vice Provost for Graduate Studies

Acknowledgement

Sincere gratitude towards the American University of Sharjah (AUS), the institution that continued to support me and enrich my knowledge since 2008 and offering the graduate assistantship. My professors and advisors in the College of Engineering who showed nothing but encouragement towards my educational journey. AUS, Dr. Hasan Al-Nashash, and the Biomedical and Bioengineering Research Institute for the constant support and rewarding opportunities. The drug delivery under Dr. Nahid Awad, Mr. Vinod Paul and Dr. Mohammad Al-Sayah who were always more than happy to answer my questions and share their experience and knowledge. Most importantly Dr. Ghaleb Husseini, who taught me that hard work, persistence and a positive attitude are the keys to becoming a better student, person and researcher.

Abstract

As the number of cancer patients increase, so does the number of patients that undergo chemotherapy, as well as the suffering, caused by its side effects. To solve this adversity, an innovative form of delivering chemotherapeutics and reducing their adverse effects is envisioned through the use of nanocarriers and ultrasound. Nanocarriers; dendrimers, solid lipid nanoparticles, micelles, and liposomes can be used to exploit passive targeting and the enhanced permeability and retention (EPR) effect found in cancerous tumors. For maximum accumulation at the tumor site, active targeting, and receptor-mediated endocytosis, via the conjugation of specific ligands, including carbohydrates, small molecules, proteins, and antibodies, are utilized. The controlled release of chemotherapeutics at the tumor site is then achieved by an external or internal trigger. Hepatocellular carcinoma has been found to overexpress the Asiaglycoprotein Receptor (ASGPR). Therefore, liposomes are synthesized through the lipid film hydration method and conjugated with Lactobionic acid (LA) as a targeting moiety. Infrared spectroscopy and phenol-sulfuric acid assay confirmed the attachment and molecular structure. Dynamic Light Scattering (DLS) determined the size and dispersity of the lactosylated liposome and NH2 liposomes encapsulating calcein to be 85.7±1.2 nm and 89.2±2.7 nm, respectively. Controlled release of calcein (a model drug), is achieved through low-frequency Ultrasound (US) as an external trigger at 3 power intensities of 7.46, 9.85 and 17.31 mW/cm2. The release mechanism was studied using nine different mathematical kinetic models: zero-order, first-order, Higuchi, Hixon-Crowell, Korsmeyer-Peppas, Baker-Lonsdale, Weibull, Hopfenberg and Gompertz. The release data were found to follow the Weibull model, having the highest coefficient of determination (R^2). Control liposomes followed first-order release Fickian diffusion and LA liposomes had a combined release of Fickian and case II diffusion with a b-value of 1.0 and 0.91, respectively. The results of this thesis show the utility of using targeted liposomes and ultrasound in cancer treatment.

Keywords: ***Drug Delivery; Chemotherapy; Liposomes; Lactobionic Acid Ultrasound; Kinetic modeling***

Table of Contents

List of Figures

List of Tables

List of Abbreviations

ASGPR	Asiaglycoprotein
DDS	Drug Delivery System
US	Ultrasound
HCC	Hepatocellular Carcinoma
EPR	Enhanced Permeability and Retention
DLS	Dynamic Light Scattering
IR	Infrared
DSPE-PEG_{2000}-NH_2	1,2-distearoyl-*sn*-glycero-3-phosphoethanolamine-N-[amino(polyethylene glycol)-2000]
DPPC	1,2-dipalmitoyl-*sn*-glycero-3-phosphocholine
LA	Lactobionic Acid
NHS	N-hydroxysuccinimide (NHS)
EDC	1-Ethyl-3-[3-dimethylaminopropyl)] carbodiimide hydrochloride
PBS	Phosphate Buffer Solution
TEA	Triethylamine
CFR	Cumulative Fraction Release
Dox	Doxorubicin

Chapter 1. Introduction

In this chapter, an introduction will be provided on cancer along with its physical and economical side effects. Furthermore, the research contribution and thesis organization will be discussed.

1.1 Overview

Cancer is one of the most extensively spread and feared diseases, with its uncontrolled nature and unpredicted arrival. According to the World Health Organization (WHO) website, cancer is the second cause of death worldwide with 8.8 million mortalities in 2015 and 9.6 million deaths in 2018. With all the advancements in technology and an extensive amount of research, cancer is still killing 1 in 6 people around the world. The most common type of cancer is prostate cancer for males whereas breast cancer is that for females, but lung cancer is the deadliest form of cancer with 2.9 million cases in 2018 [1]. Furthermore, according to the American Cancer Society, the total medical cost of cancer was 80.2 billion dollars in 2015. The cost includes medical procedures, drugs, treatment of drugs toxicity, and much more [2]. All these statistics show the extensive burden of cancer on the society's well-being whether physical, mental or financial.

Physical, chemical or biological carcinogens interact with our genes on a daily basis causing the abnormal growth of healthy cells into tumors. Cancer destroys the healthy routine of cell rejuvenation and turns it into an uncontrolled division of dysfunctional and mutated cells. Tumors can be malignant or benign in nature; Benign tumors do not spread into surrounding tissues, hence can be surgically removed without harm. On the other hand, malignant tumors are the real threat; they have an erratic behavior and tend to spread to different body organs causing cancer to metastasize [1], [3].

Awareness surrounding cancer has increased over the years and so did the number of people affected by it, hence scientists, researchers, and medical professions are becoming more and more determined to overcome this epidemic. Moreover, individuals are becoming more conscious about their lifestyle decisions that may directly or indirectly affect their likeliness to develop cancer. Smoking habit, balanced

diets, exercise, and annual health checkups are precursors to leading a healthy and long life [4].

Cancer treatments vary widely depending on the type, stage and the location of the tumor; treatment can be focused one treatment pathway or a combination of different approaches, such as surgery, chemotherapy, radiation therapy, immunotherapy, hormone therapy, gene therapy, and stem cell transplantation [5]. The most prevalent form of cancer therapy is chemotherapy that uses anti-neoplastic agents such as Doxorubicin, Fluorouracil, and Cyclophosphamide to eradicate cancer cells. Nonetheless, the nonspecific and non-targeted nature of this treatment has severe adverse effects as seen in Figure 1. Therefore, increasing the chemotherapeutic dose while targeting the tumor site may result in a much more efficient and safer form of cancer treatment [6].

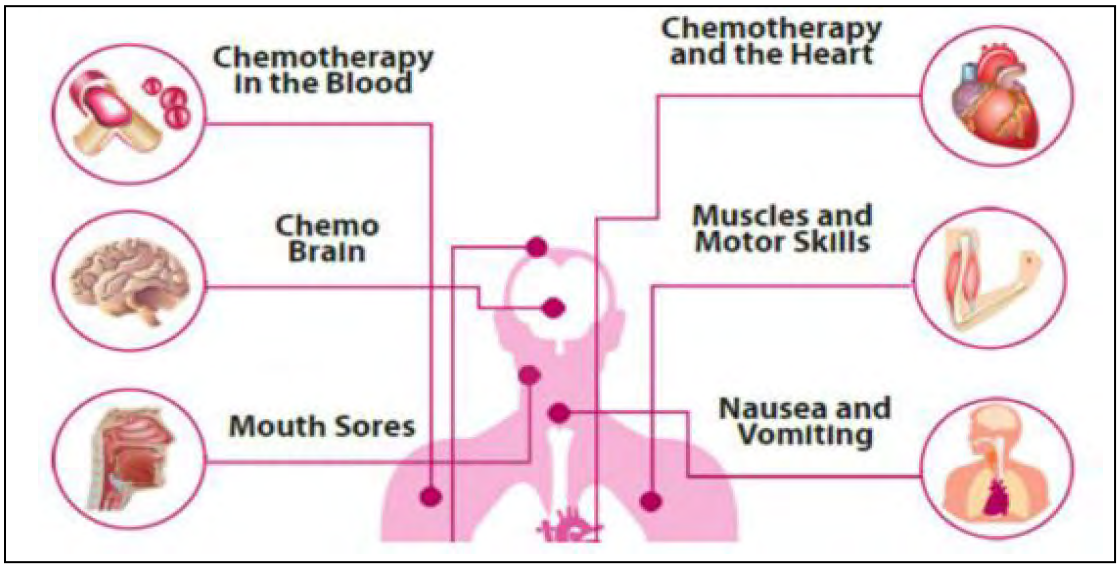

Figure 1: Side effects of chemotherapy [6]

Using this mindset, the use of nanotechnology has been attracting much attention for being an innovative approach in the world of Drug Delivery Systems (DDS). The prefix nano comes from the Greek language meaning dwarf [7], and according to the International Organization of Standardization (ISO), nanomaterial is defined as “material with any external dimension in the nanoscale or having an internal structure or surface structure in the nanoscale” (nanoscale being around 1-1000 nm) [8]. Nanocarriers can be used to encapsulate and transport drugs to cancer tumor sites,

where the efficiency of this transport depends on their small size, ability to be modified and target specific organs by ligand attachment (active targeting), and the irregular cell distribution of tumors allowing them to target and maneuver into the tumor (passive targeting) [9].

According to WHO, hepatocellular carcinoma resulted in 782,000 deaths worldwide making it the third cause of death in underdeveloped countries. The liver is a crucial body organ that detoxifies and metabolizes different substances, hence in the case of targeted nanocarriers their accumulation in the liver is guaranteed [10]. Liver is also part of the Mononuclear Phagocyte System (MPS) where Kupffer cells (a type of white blood cells) are involved in the body defense process. Another unique feature of the liver is the overexpression of the Asialoglycoprotein receptor (ASGPR), each hepatocyte (liver cell) expresses 500,000 ASGPR, which is minimally expressed in other body parts. ASGPR has been found to mainly bind to sugar-based molecules such as glycoproteins, carbohydrates, and sugar isomers [11].

1.2. Research Contribution

For the purpose of this research, liposomes are chosen to encapsulate the model drug calcein while simultaneously actively targeting ASGPR receptors overexpressed on the surface of liver cancer cells through the lactose moiety. Ultrasound will be utilized as an external trigger to control drug release spatially and temporally. This is the first study to combine disaccharides-targeting, liposomes, and ultrasound in drug delivery to treat cancer.

1.3. Thesis Organization

The thesis will be organized as follow. Chapter 2 includes the background and literature review on several forms of nanocarriers, ligands, and triggers. Chapter 3 will then state the objective of the research conducted in this thesis. Chapter 4 presents the details of the materials used, the synthesis scheme utilized to produce the DSPE-PEG_{2000}-Lac liposomes, the liposomal characterization techniques employed (infrared spectroscopy and the phenol-sulfuric acid assay, and dynamic light scattering), and the technical details of the low-frequency ultrasound used to release the model drug and finally, the kinetic models used. Chapter 5 will present the results of this study along

with the research and discussion of outcomes. Finally, the thesis will be concluded (chapter 6) with upcoming work plans for testing and synthesis.

Chapter 2. Background and Literature Review

In this chapter, four different types of nanocarriers will be discussed. Enhanced Permeability and Retention (EPR) effect will be examined as a crucial element in the design of drug delivery systems when chemotherapeutics is to be delivered. Furthermore, active targeting through receptor-mediated endocytosis is explained through four types of ligands, and finally, eight forms of triggering techniques for the controlled drug release will be summarized.

2.1. Nanocarriers

The fight against cancer has pushed scientist and researchers into exploring new, efficient and innovative forms of cancer therapy. Nanomedicine, to deliver chemotherapy, is studied to enhance drug delivery by reducing the side effects experienced by patients and the drug toxicity to non-cancerous cells, and in the process improving drug accumulation and specificity at the tumor site. Nanoparticles with varying physical and chemical forms and dimensions, act as promising carriers for cancer therapeutics through passive and active targeting. Dendrimers, solid lipid nanoparticles, polymeric micelles ,and liposomes, seen in Figure 2, each has its uniqueness in the study of drug delivery using nanocarriers [12].

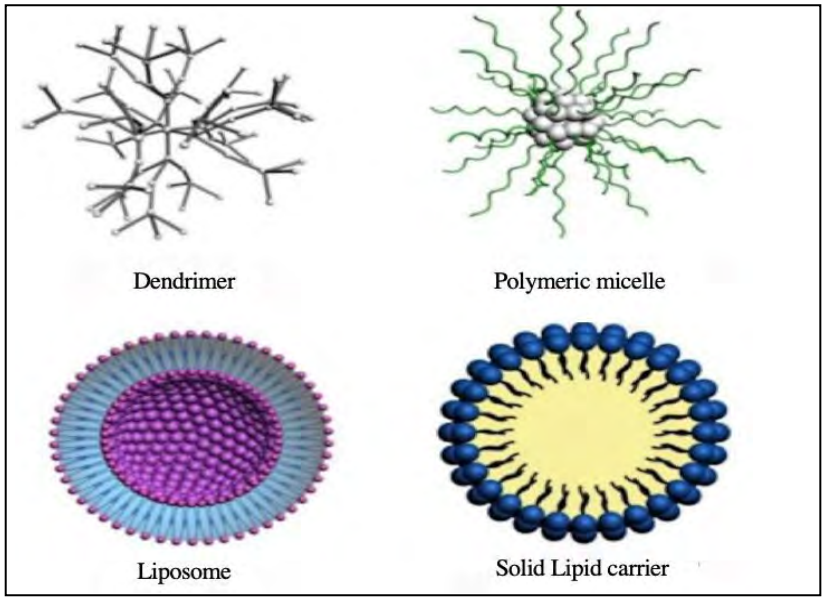

Figure 2: Types of Nanocarriers [12]

2.1.1. Dendrimers. An originally Greek word meaning a tree or branch, attributing it to its highly branched physical structure. It is a three-dimensional structure with a central core and branches ending with various functional groups. Dendrimers can enclose hydrophobic drugs in its branches and inner core while exhibiting water solubility due to its hydrophilic functional groups on the exterior. Dendrimers are most commonly synthesized using either the divergent or the convergent approaches, in which growth begins from the core or the terminal branches, respectively. The unique structural manipulation found in dendrimers makes them excellent vehicles for drug delivery, but cytotoxicity and hemolysis remain challenging issued that need to be addressed. The strong cationic nature of dendrimers interacts with the anionic body membranes causing cell disruption and destabilization [13]. The three most used types of dendrimers are polyamidoamine (PAMAM), Poly (propylene imine) (PPI) and Poly-L-lysine (PLL) dendrimers. Studies by Jevprasesphant et al. and Bhadra et al. [14] showed that modification of PAMAM dendrimers with Polyethylene glycol (PEG) will significantly reduce the toxicity and enhance their drug delivery characteristics [14].

2.1.2. Solid lipid nanoparticles. Solid lipid nanoparticles (SLN), also known as lipospheres, with sizes ranging between 50 and 100 nm, are lipids that are solid state at room and body temperature and used in the production of nanocarriers. The synthesis of solid lipid nanoparticles has been achieved using several routes, using different kinds of lipids including glycerides, fatty acids, and waxes; the hot homogenization and cold homogenization synthesis schemes, being the most popular. Their low toxicity, small diameter and ability to carry lipophilic drugs, have made them desirable carriers for the delivery of chemotherapeutics. Gasco et al. [15] examined the cytotoxicity of SLN encapsulating Dox in comparison to free Dox on two cell lines, and found an increase in cytotoxicity when SLN where used to encapsulate Dox [15], [16].

2.1.3. Micelles. Micelles are amphipathic monomers, consisting of a hydrophilic tail and hydrophobic head. When these structures are dissolved in an aqueous solution they form a spherical monolayer at the Critical Micelle Concentration (CMC) and Critical Micelle Temperature (CMT). Lipophilic drugs can be encapsulated in their core and are surrounded by its hydrophilic outer shell or corona. Once the CMC and CMT are reached, these polymeric chains aggregate to form micelles. The lower the CMC values, the more stable is the nanocarriers. Polymeric micelles have a small

diameter (between 10-200nm), with two or more block co-polymers, and a low CMC value [17]. In ultrasonic drug delivery, the most commonly used type of polymeric micelles is those produced using Pluronic® constructed from hydrophilic and hydrophobic triblock polymers of Poly Ethylene Oxide (PEO) and Poly Propylene Oxide (PPO). The addition of PEO provides stability and more extended blood circulation times. A study by Batrakova et al. [18] found that when using Pluronic® micelles cancer cells were able to overcome the resistance developed to chemotherapeutic drugs [18].

2.1.4. Liposomes. Liposomes are spherical vesicles with a composition similar to the cell membrane. Phospholipid bilayers, primarily composed of a polar hydrophilic head and a non-polar hydrophobic tail, along with cholesterol. The unique architecture of liposomes makes them suitable carriers for hydrophilic drugs in its inner aqueous core and lipophilic drugs in its membrane; with a drug-loading efficiency as high as 0.25 mg drug/mg. Most importantly, liposomes are FDA (Food and Drug Administration) approved, since 1995 which makes them easy to research with a higher probability of commercialization [19]. The number of bilayers and diameter range of the liposome is the basis of liposomes classification as seen in Table 1. For the delivery of chemotherapeutics, the small internal size of Unilamellar Vesicles (ULVs) makes them the most desired form of liposomes, since studies have found that they have a longer half-life compared to larger liposomes. Furthermore, liposomes biocompatibility, ease of synthesis, high drug-loading efficiency and ability to encapsulate both hydrophobic and hydrophilic drugs have made these liposomes an extensively researched and used form of nanocarriers; studies by Herman et al. [20], showed that liposomes encapsulating Dox, had less cardiotoxicity in comparison to free Dox; another study by Zvi et al. [21] showed that liposomes encapsulating Dox had higher accumulation in cancerous muscle tissue than healthy tissue [20], [21].

The main disadvantage of all nanocarriers is their detection by the mononuclear phagocyte system and hence are removed from blood circulation through opsonization. Therefore, the addition of hydrophilic polymers such as Polyethylene glycol (PEG) prolongs the circulation time of liposomes by avoiding the detection by the immune system as a foreign molecule and increases its stability, transforming them into what is known as stealth liposomes [22]. A study by Needham et. al, found that PEGylated

liposomes avoided aggregation and had strong inter-membrane forces thus increasing stability and another study by Blume et. al showed that the addition of PEG to the liposomal structure had increased their blood circulation time through reduced opsonization [23]. Figure 3 shows different additions that can be applied to create the most efficient drug delivery system with liposomes, targeted liposomes will be further explained in the coming sections [24].

Table 1: Liposomes Classification

Liposomes	Bilayers	Diameter(nm)
Multilamellar Vesicles (MLVs)	Multiple	100-1000
Small Unilamellar Vesicles (SUVs)	Single	Less than 100
Large Unilamellar Vesicles (LUVs)	Single	More than 100

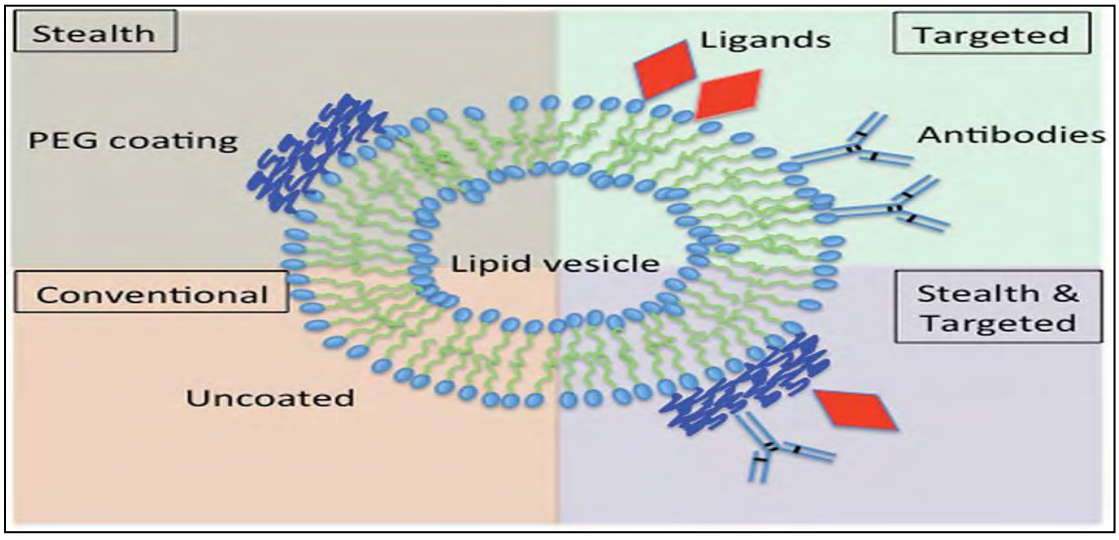

Figure 3: Liposome modifications [24]

2.2. The EPR Effect

The physical differences found between healthy and cancerous cells/tissues present a pathway for an efficient, less toxic and more targeted form of drug delivery.

The fact that cancerous cells experience abnormal growth results in the need for more blood vessels to support their growth. These blood vessels will have a leaky irregular structure and a wide lumen(opening), with their endothelial cells having wider fenestrations and lacking the layer of smooth muscle cells. These physical distinctions will increase the permeability of the nanocarriers (if the size of the vehicle is below 200 nm) into cancerous cells in comparison to healthy cells. Furthermore, biological differences are also found; cancer cells have a dysfunctional lymphatic drainage system. The lack of an efficient immune system allows for the prolonged accumulation of the chemotherapeutics at the tumor site.

The factors mentioned above and others such as an increased Vascular Endothelial Growth Factor, Bradykinin, Nitric oxide, Peroxynitrite, Prostaglandins, and Cytokines results in a phenomenon known as the Enhanced Permeability and Retention (EPR) effect [25].

2.3. Active Targeting

The biological and chemical changes that occur due to the abnormal growth of cells i.e. cancer, will force the cells to overexpress certain receptors to accommodate for the increased need for oxygen, glucose, and nutrients, and to produce enough energy to sustain their growth [26]. The nanocarriers mentioned in section 2.1 are good candidates for utilizing passive targeting. While each carrier has its advantages and drawbacks, still a more specific, and a less toxic approach is desirable. Active targeting is the key to a more successful drug delivery system, in which small molecules (ligands) are conjugated to the surface of the nanocarriers, hence increasing the drug uptake by cancerous cells through receptor-mediated endocytosis [27].

2.3.1. Types of ligands. The types of ligands discussed below are folic acid, antibodies, peptides and carbohydrates.

2.3.1.1. *Folate*. The folate molecule, folic acid or vitamin B9, is a small, low-cost and non-toxic compound, used to target the folate receptor overexpressed on the surface of human cancer cells. The folate receptor is a glycosylphosphatidylinositol conjugated glycoprotein having a molecular weight of around 38-40 kilo Dalton (kD). It is usually overexpressed on the surface of various tumor cells. Several types of

cancer, such as ovarian, breast, lung and brain overexpress the folate receptor, but it has been mainly studied and targeted in ovarian carcinoma treatment [28], [29].

2.3.1.2. ***Antibodies***. Antibodies or Immunoglobulins (Ig) are glycoproteins, IgA, IgD, IgE, IgG, and IgM, which bind to antigens. Monoclonal antibodies can be produced in laboratories and are used in targeting tumor-specific antigens. Monoclonal antibodies and their fragments have been studied as ligands for active targeting, e.g. Herceptin and Rituxumab [6], [30]. Complete antibodies have two binding sites, capable of creating a more stable attachment site, it also increases the risk of being detected and cleared by the immune system. Therefore, antibody fragments have been studied because they exhibit lower immunogenicities [31].

2.3.1.3. ***Peptides.*** Proteins and proteins fragments can be engineered to be used in ligand-mediated targeting, while chemically modifying their amino acid sequence for enhanced stability and tumor specificity. Several peptides have been under research such as Arginine-Glycine-Aspartic acid (RGD) and Luteinizing Hormone Releasing Hormone (LHRH). RGD is recognized by around half of the known transmembrane receptors (integrins), such as those found in breast cancer and glioblastoma. Hormone associated carcinomas overexpress the LHRH receptors, making LHRH a suitable tumor-targeting ligand for prostate and breast cancers [32].

2.3.1.4. ***Carbohydrates.*** Monosaccharides, disaccharides, and polysaccharides are simple and complex sugars, which have been widely incorporated in the production of nanocarriers and pharmaceutical products. Carbohydrates have the advantages of being easily obtainable, biocompatible, biodegradable and nontoxic. Their various types and structures have made them promising ligands for the delivery of anti-cancer drugs through receptor-mediated endocytosis. Overexpressed receptors on cancerous cells, such as cluster determinant 44 (CD44), binds to hyaluronic acid and the Asialoglycoprotein(ASGPR) receptors, associated with human hepatocellular carcinoma(HCC), binds to lactose and pullulan [33]. An *in vitro* study conducted by Zhou et al.[32] showed that Hep-G2 cells (human liver cancer cell line) had a four-time greater cellular uptake of Lactosylated liposomes than non-targeted liposomes [34].

232. Receptor-mediated endocytosis. Choosing the accurate ligand corresponding to the overexpressed cell receptor is needed for a mechanism known as receptor-mediated endocytosis. The binding site of the ligand-attached nanoparticle

will interact with the cell receptor by intermolecular reversible bonds like hydrogen bonds and van der Waals forces, resulting in a receptor-ligand complex. As seen in Figure 4, the key and lock relationship between the ligand and receptor will allow the internalization of the nanocarrier inside the cell by cytoplasmic vesicles, hence increasing the accumulation of the drug-carrying nanoparticles in the tumor site [31], [35].

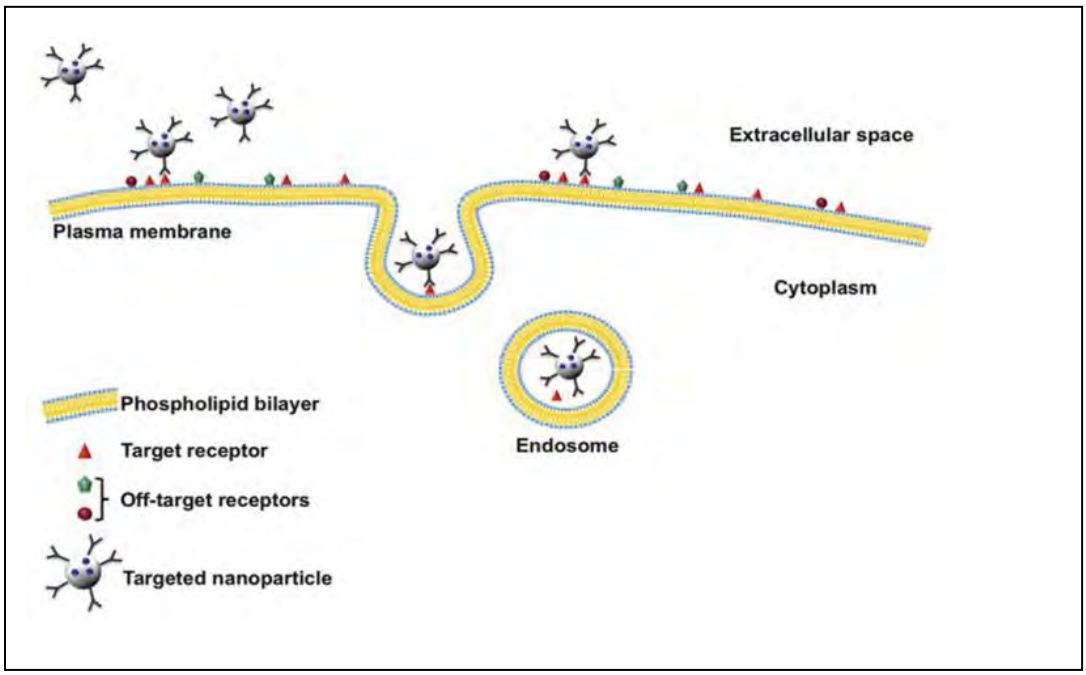

Figure 4: Receptor Mediated Endocytosis [31]

2.4. Triggers

The mechanisms discussed in the previous sections were designated to increase the accumulation of the drug encapsulating nanocarriers at the tumor site while ensuring the decrease in cytotoxicity to other healthy cells. After the successful arrival and accumlation at the tumor site (by receptor-mediated endocytosis), certain triggers can be employed for the drug to be released in a controlled manner (spatial and temporal). Each form of release must be tailored towards the nanocarrier, in order to achieve maximal drug efficiency. In this section, intracellular and external triggers will be discussed as forms of controlled drug release at the tumor site, as shown in Figure 5. Intracellular triggers include pH, enzymes, and redox agents; while external triggers

included but are not limited to heat, electromagnetic waves, magnetic field, light, and ultrasound [36].

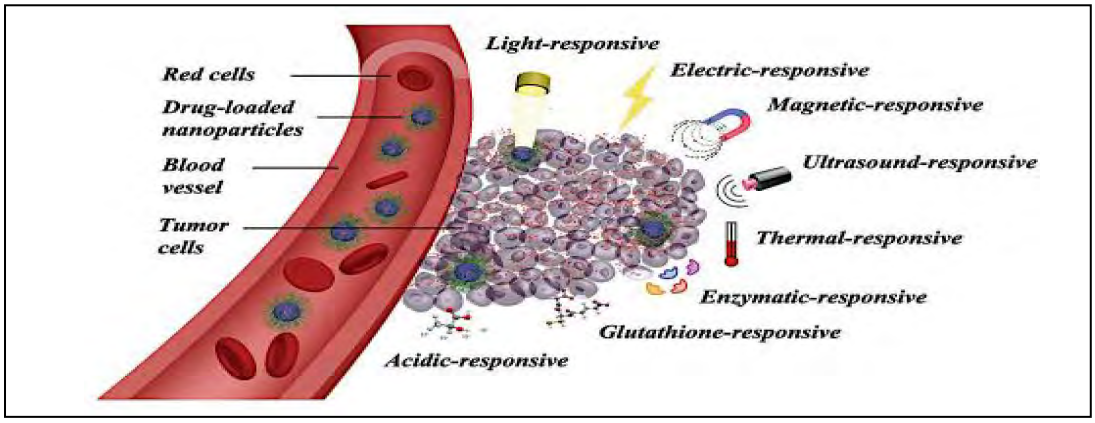

Figure 5: Triggering techniques [36]

241. pH. The uncontrolled growth, division, and metabolism in cancer cells, cause elevated levels of lactic acid at the tumor site. Lactic acid is produced from pyruvic acid which is a result of anaeorobic glycolysis (breaking down of glucose without oxygen) to produce energy when not enough oxygen is found for aerobic respiration [37]; thus increasing the acidity in the tumor site (~pH 6.5) in comparison to healthy cells (~pH 7.4). The low pH will act as a trigger for the release of the chemotherapeutics by the destabilizing of the endosome [36]. For example, specific liposomes can be modified to become pH sensitive, by the use of pH-sensitive lipids, polymorphic lipids or attaching titratable polymers [38].

242. Enzymes. One of the many variations in the biology of healthy and cancer cells is the overexpression of enzymes in tumors. Enzymes like Phospholipases (PLA_2) and Matrix metalloproteases (MMP) serve as triggers for the degradation of the nanocarrier and hence the drug release at the tumor site. PLA_2 act as a catalyst for the hydrolysis of phospholipids into free fatty acids and lysophospholipids. PLA_2 catalytic activity is a function of membrane charge and the state and configuration of the lipid nanocarrier. Combining the previous characteristics and PLA_2 increased activity towards lipid nanocarriers, liposomes or micelles can be engineered, including PEGylated liposomes, to undergo hydrolysis by PLA_2. MMP an enzyme found in several types of cancer (such as brain, lung and cervical cancers), is also studied as an

enzymatic trigger for drug release. For MMP activation, the liposomal membrane of the nanocarrier must include specified lipopeptides to act as the substrate [39].

2.4.3. Redox agents. The unique tumor environment has a different redox state when compared to healthy cells. A reductive and oxidative environment with an increased level of intracellular glutathione (GSH) and intracellular Reactive Oxygen Species (ROS) are used as a stimulus for drug release. GSH is a tripeptide reducing agent with its concentration being about 100 times more in an intracellular environment than an extracellular environment. Therefore, reduction sensitive nanocarrier can be synthesized through the addition of disulfide crosslinkers, or oxidation of thiol groups, or thiol-disulfide exchange reaction to the polymeric nanocarrier. Reactive Oxygen Species (ROS), such as Hydrogen peroxide (H_2O_2) cause oxidative destabilization to the ROS sensitive nanocarriers [40].

2.4.4. Heat. A body temperature of around 37°C is crucial for all the metabolic activities, any disruption to the temperature gradient will result in cellular imbalance and death. Therefore, studies have shown that increasing the temperature level up to 42°C, will result in the death of tumor cells. Hence, hyperthermia is used for both the eradication of tumor cells and as an external stimulus for the drug release from temperature sensitive nanocarriers. For example, Temperature Sensitive Liposomes, are stable at normal body temperature but become leaky when they experience hyperthermia. Another example is polymers with a Low Critical Solution temperature (LCST) which undergo a hydrophilic-hydrophobic transition when exposed to temperatures above their LCST; the phase transition destabilizes the liposomal membrane and releases the drug [38], [41].

2.4.5. Electromagnetic waves. Microwaves can be employed for the release of chemotherapeutics from the nanocarrier once at the tumor site. Hyperthermia is induced by externally focused microwaves. Since the human body is composed of 60% water, applying microwave power will cause a rapid temperature increase. This technique is mostly studied to treat superficial carcinomas such as skin cancer [38].

2.4.6. Magnetic field. An alternating Current Magnetic Field (ACMF), as a stimulus for drug release, is the third external trigger to be discussed here. AMF can be employed to induce hyperthermia, and it can also be used as a separate external trigger for the release of the drug from chemically modified nanocarriers that are sensitive to

AMF. The most commonly used modification is by the addition of the low toxic Iron (III) Oxide Fe_3O_4. The gradual and controlled release of the chemotherapeutics by the utilization of this method is considered to be safe, non-invasive and able to penetrate deep tissue tumors as long as the AMF is less than $5x10^9$ A/m.s [42].

247. Light. The use of light as an external trigger for the release of the encapsulated chemotherapeutics from nanocarriers has also been investigated. Light is a practical stimulus since its wavelength, intensity and application duration can be manipulated to achieve optimal drug release. It can either be used as a form of thermal energy to cause hyperthermia or as a direct stimulus that changes the configuration of the nanocarrier. Nanocarriers can be altered to be sensitive to visible, UV and infrared light, through the addition of a photochromic group [40].

248. Ultrasound. Ultrasound (US) waves are generated when a piezoelectric crystal is exposed to an Alternating Current (AC), converting electrical energy into mechanical energy. US waves are pressure/sound waves having a frequency greater than or equal to 20 kHz, It propagates through the transfer of energy from one molecule to the next, having a sinusoidal and longitudinal pattern alternating between high (upper peak) and low pressure (lower peak) phases through a fluid medium [43]. At the high-pressure points and low-pressure points the molecules compress and stretch respectively.

Ultrasound waves are controlled by four parameters: frequency, power intensity, mode of operation and attenuation. Frequency is the number of sinusoidal waves per second measured in Hz. Power intensity, also known as US density, is the power per cross-sectional area measured in W/cm^2. The mode of operation could be continuous or pulsed; continuous is when the US is applied non-stop for a defined period of time, whereas pulsed is having an “on” and “off” alternations of the US wave [44]. Finally, attenuation refers to losses due to absorption and reflection of energy by the fluid medium. The relation between these parameters is as follows: the higher the frequency, the smaller the wavelength and penetration distance, and the more the attenuation. Therefore, when designing a DDS, experiments must be done to decide the most suitable parameters of the US.

When using US as a trigger for the controlled release of chemotherapeutics, it can be employed in two ways, first for inducing hyperthermia, and the second is through

the phenomena of cavitation. High-intensity focused ultrasound (HIFU) raises the temperature at the tumor site, in the range of 40-42°C, killing the cancer cells. HIFU can also be used as a trigger for temperature sensitive nanocarriers, as discussed in section 2.4.4. Furthermore, US can be used as an externally controlled trigger for release through the principle of cavitation. Cavitation is explained through resonance frequency, when the resonance frequency of the US is the same as the gas bubbles formed in the acoustic field, oscillations along the wave will result in the compression of the bubble at high pressure and decompression at low pressure. This process is known as stable cavitation. The gas bubble can be naturally occurring or introduced at the tumor site. When the tolerance point of the bubble is surpassed, i.e. the bubble is no longer able to compress or stretch, the oscillations will be unstable causing it to burst, this is known as inertial or transient cavitation, as shown in Figure 6 [45]. If the nanocarrier was close to the site of transient cavitation, then the intense shock wave will open the nanocarrier releasing the drug. Furthermore, the shock wave and microjets of liquid will unsettle the surrounding cell membrane of the tumor site facilitating the entry of the drug through the formation of pores in a process known as sonoporation, an illustration is found in Figure 7 [46]

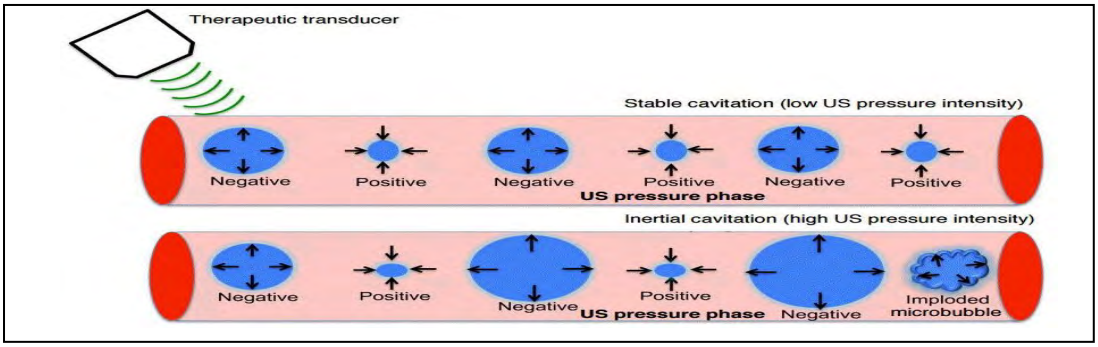

Figure 6: Stable and inertial Cavitation [45]

Another advantageous characteristic of US is its synergistic effect when combined with chemotherapeutics. Studies have shown that this combination will increase the cytotoxicity of the drug [38], [47]. Furthemore, it must be noted that even though US is considred safe, caution must be taken by avoiding long exposure to US and using medically safe frequencies

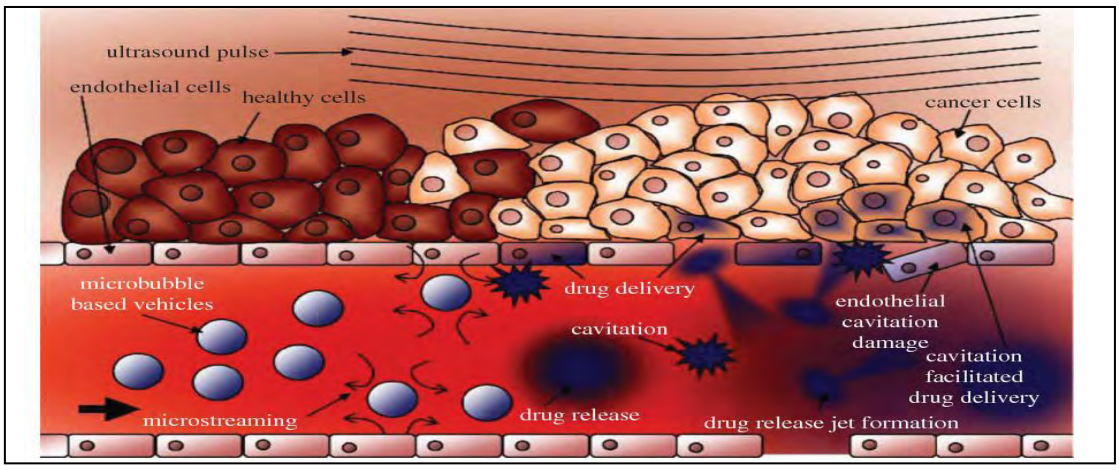

Figure 7: Sonopor ation [46]

An in-vitro study by Schroeder et al. [48], showed the effect of applying pulsed and continuous low-frequency ultrasound (LFUS) at 20 kHz and 3.3 W/m2, on liposomes encapsulating drugs. The study was done using three different drugs: Dox, Methylprednisolone hemisuccinate and Cisplatin. Results have shown that the exposure to LFUS has released 80% of the encapsulated drug due to the increased permeability of the liposomes [48].

Another *in vitro* study by Afadzi et al. [49], and using HeLa cells, utilized liposomes encapsulating Dox exposed to 300 kHz of US with varying power intensities. They studied the role of endocytosis, microbubbles, and sonoporation in enhancing cellular uptake [49].

An *in vivo* study done by Meyhr et al. [50] used nude mice injected with human colon cancer cell line. The study utilized LFUS of 20 kHz on liposomes encapsulating Dox (Caelyx). Two different concentrations of Caelyx, namely 3 mg/kg and 6 mg/kg, were tested and compared to the control group. The results showed a significant difference between the groups treated with the combination of US and Caelyx and control groups. Furthermore, synergism was found between US and the chemotherapeutic drug, and specifically higher synergistic effects were measured at the lower drug concentration of 3 mg/kg [50].

Another *in vivo* study done by Pitt et al. [51], used BDIX rats with bilateral intradermal DHD/K12 tumors. The rats were injected with PC: Cholesterol: DSPE-PEG_{2000}: alpha-tocopherol stealth liposomes encapsulating Dox. Weekly treatments with 15 minutes exposure to 20 kHz were performed for a month on one of the tumor

sites. Results showed a significant statistical difference between the tumors treated with US and non-treated tumors, in the same rat [51].

Chapter 3. Objectives

With the increasing number of cancer-related deaths and highly adverse aftereffects of conventional delivery of chemotherapeutics, enhanced and more effective methods of anti-neoplastic administration must be researched. Focusing on hepatocellular carcinoma, ASGPR as a liver-specific receptor that binds to the lactose molecule is employed to enhance cellular uptake.

The objective of this research is to present an effective and noninvasive form of chemotherapeutic delivery using (i) nanocarriers targeted with the Lactobionic acid moiety and (ii) ultrasound to actively target liver cancer cells. The specific aims of this thesis are:

1. The conjugation of Lactobionic acid with DSPE-PEG_{2000}-NH_2, using EDC and NHS.
2. The synthesis of control and Lactobionic acid liposomes, encapsulating calcein, using the lipid film hydration method with the addition of cholesterol and DPPC.
3. The conjugation confirmation between Lactobionic acid and DSPE-PEG_{2000}-NH_2 through Infrared Spectroscopy and the phenol-sulfuric acid assay.
4. The characterization of the targeted liposomes size and dispersity using Dynamic Light Scattering (DLS).
5. The characterization of the targeted liposomes' lipid content using the Stewart assay.
6. Testing the controlled release using low-frequency ultrasound (US) at 3 power intensities of 7.46, 9.85 and 17.31 mW/cm^2, by measuring the fluorescence intensity of calcein.
7. Modeling release data using nine kinetic models: first-order, zero-order, Higuchi, Korsmeyer-Peppas, Weibull, Gompertz, Hixson-Crowell, Baker-Lonsdale, and Hopfenberg model.
8. Finding the best fit for the acquired release data, through the highest coefficient of determination This will shed light on the mechanism of the release of chemotherapeutics and model drugs from lactose targeted liposomes using acoustic waves.

Chapter 4. Materials and Methods

This chapter includes the methodologies used in, the synthesis of Lactosylated liposomes encapsulating calcein, followed by liposomal characterization using Dynamic Light Scattering (DLS) to determine the particle size, Stewart assay to determine lipid content, Infrared spectroscopy and, phenol-sulfuric acid assay to determine the molecular structure. Furthermore, the release of a model drug using US will be investigated at a low frequency of 20 kHz, at 3 power intensities. Finally, an analysis on modeling using nine kinetic release models will be performed.

Calcein is a model drug that will be used to mimic Dox and will be encapsulated inside the liposome. Calcein is a fluorescent dye with specific excitation and emission wavelength of 495 and 515 nm respectively, making the amount of drug released and encapsulated in the liposomes known by measuring the intensity of the dye by a spectrofluorometer. Calcein self-quenches inside the liposomes, and leaks out with ultrasound then undergo self-quenching again when not being exposed to ultrasound [52].

Liposome synthesis is done using DSPE-PEG_{2000}-NH_2 (1,2-distearoyl-*sn*-glycero-3-phosphoethanolamine-N-[amino(polyethylene glycol)-2000]), with the addition of cholesterol and DPPC(1,2-dipalmitoyl-sn-glycero-3-phosphocholine). DSPE-PEG_{2000}-NH_2 is a stable lipid, sensitive to temperature variations hence appropriate for use with US, cholesterol adds flexibly to the prepared liposomes and Polyethylene Glycol (PEG), is responsible for increasing the circulation time as discussed earlier in section 2.1.4.

Since the lactose molecule does not have the carboxyl group required for the reaction with the amine group of the phospholipid in liposomes, Lactobionic acid is reacted with DSPE-PEG_{2000}-NH_2. The reaction occurs with the aid of 1-ethyl-3-[3-dimethylaminopropyl)] carbodiimide hydrochloride (EDC) and N-hydroxysuccinimide (NHS, $C_4H_5NO_3$) for coupling the carboxylic acid to the amine and stabilization, respectively.

4.1. Materials

Chemicals and lipids used include: Ethanol, Methanol, Dichloromethane, Chloroform, Lactobionic acid, Hydrochloric acid, EDC, NHS, Triethylamine (TEA), Potassium Chloride (KCl), Potassium dihydrogen Orthophosphate (KH_2PO_4), di-

Sodium hydrogen phosphate (Na_2HPO_4), Sodium Chloride (NaCl), DPPC, DSPE-PEG_{2000}-NH_2 (ammonium salt), MES, Sodium Carbonate (Na_2CO3), Sodium Sulfate (Na_2SO_4) , 2-morpholinoethanesulfonic acid are supplied from LABCO L.L.C.

4.2. Preparation of DSPE-PEG_{2000}-NH_2 and DSPE-PEG_{2000}-Lac Liposomes

Lactose ($C_{12}H_{22}O_{11}$) is a disaccharide, consisting of glucose and galactose, but the organic structure of Lactose lacks the carboxyl group which is needed for the formation of the liposomes. Therefore, Lactobionic acid, a sugar acid, consisting of galactose and gluconic acid, and having a carboxylate anion is used instead. Lactobionic acid is formed from the oxidation reaction of Lactose, as seen in Figure 8 [53].

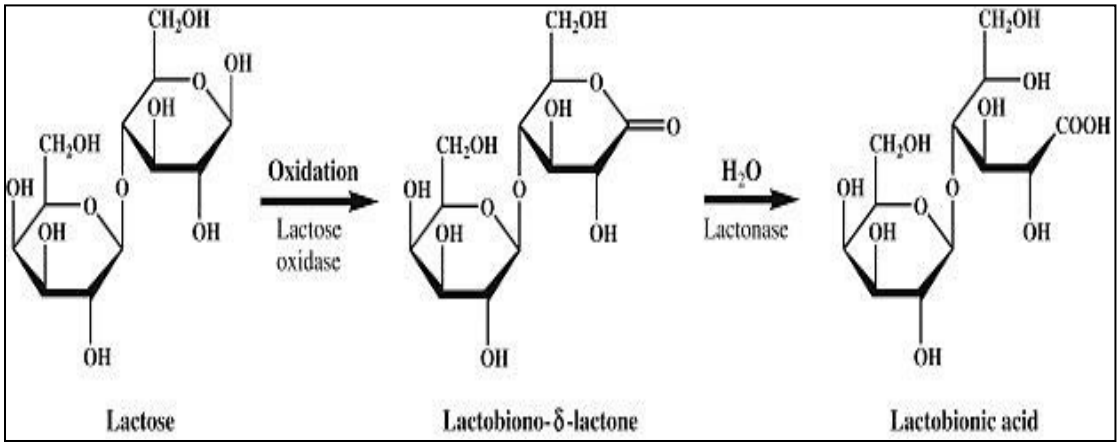

Figure 8 :Formation of Lactobionic acid [53]

EDC, a cross-linking agent, that couples carboxyl and amino groups forming an amide bond. It primarily reacts with the carboxyl group in the Lactobionic acid forming an unstable intermediate ester known as O-acylisourea. The instability is due to the fact that if found in an aqueous solution, O-acylisourea will undergo hydrolyzation, thus leading to the cleavage of the amide bond. For the reasons mentioned above, NHS is added as an activation reagent that will stabilize the reaction, forming a semi-stable amine-reactive NHS ester, which will then react with DSPE-$PEG_{2000,}$ forming DSPE-PEG_{2000}-NH_2 and DSPE-PEG_{2000}-Lac liposomes that are stable at pH 7.4 (pH of the human body) as seen in Figure 9 [54].

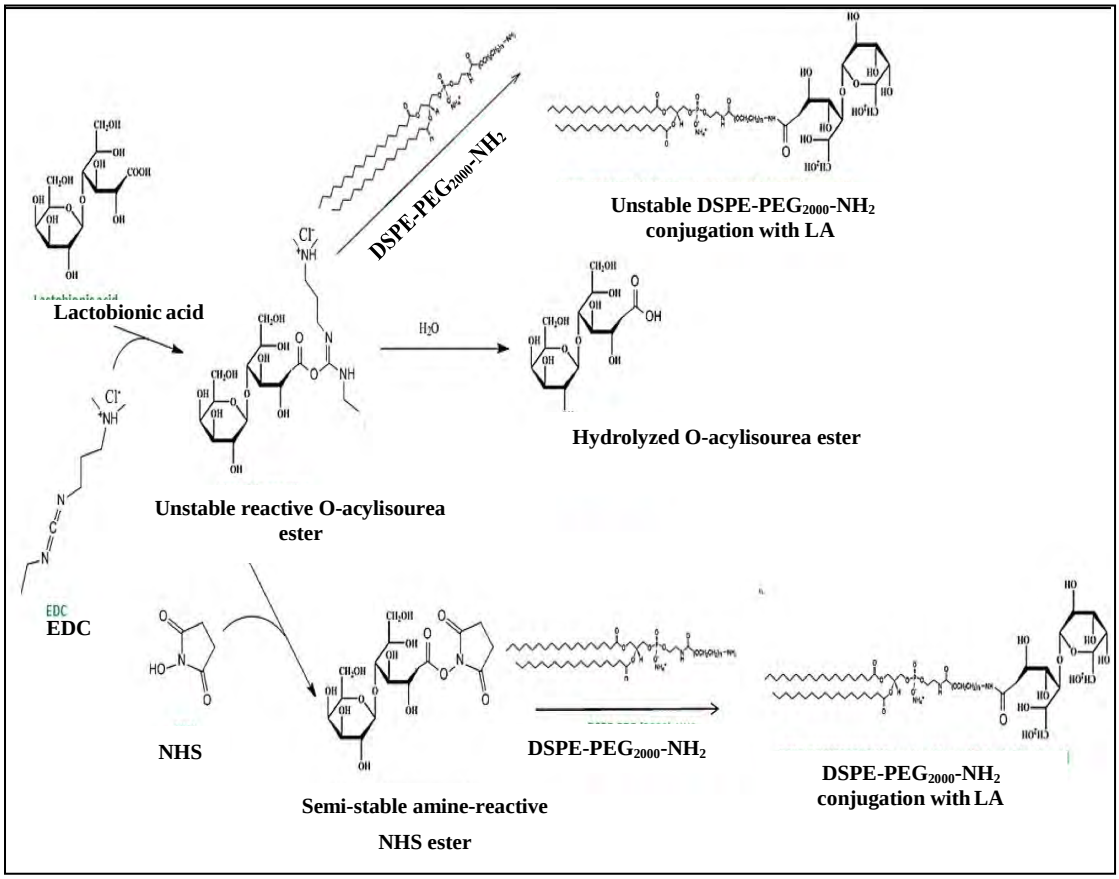

Figure 9: DSPE-PEG_{2000}-NH_2 conjugation with Lactobionic acid [54]

4.2.1. Synthesis of DSPE-PEG2000-Lac. PBS is prepared by adding 8 g, 0.2 g,1.44 g and 0.24 g of NaOH, KCl, Na_2HPO4, and KH_2PO_4 respectively, into 800 mL of deionized water (DIW). The pH must be checked to be 7.4 ± 0.05 with adjustment using HCl if needed; the resultant solution is topped up to a volume of 1 L. MES buffer pH 5.0 is prepared by dissolving 2.4405 g of MES, free acid (2-morpholinoethanesulfonic acid) in 18.75 mL of DIW, following the pH adjustment to 5.0 using 10M NaOH; the resultant solution is topped up to 25 mL using DIW.

The proposed synthesis scheme, having a molar ratio of 5:6.5:6.5:1 of Lactobionic acid, NHS, EDC, and DSPE-PEG-NH_2 respectively, will be as follows. Two solutions will be prepared; the first solution has 32 mg of Lactobionic acid dissolved in 2 mL of MES buffer pH 5.0 and placed in an ice bath for 5 minutes. Afterward, 22.4 mg of EDC and 13.5 mg of NHS are added to solution one and left to stir for around 15 minutes at room temperature. The second solution has 50 mg of DSPE-PEG_{2000}-NH_2 dissolved in 1 mL ethanol and 20 microliters of TEA, when

dissolved 1 mL of PBS is added dropwise to solution two. While continuously stirring the second solution, drops of the first solution will be added. The pH of the resultant solution is increased to 7.5-8.0 using a few drops of 0.1 M NaOH and left stirring at room temperature overnight [34]. The final sample solution is dried under vacuum using a rotary evaporater at 40˚C. The lipid components are extracted three times using a separatory funnel with the aid of dichloromethane and water, the first will only dissolve the lipid components of the sample (i.e DSPE-PEG-LA), whereas water-soluble components such as urea, NHS and EDC will not dissolve in dichloromethane resulting in the formation of two layers, one having a more hazy/milky appearance than the other as shown in Figure 10.

Figure 10: Separatory Funnel

Furthermore, Sodium Carbonate (Na_2CO_3) is added to deprotonate LA and NHS making them more water soluble. After the extraction process, around 1 tablespoon of Sodium Sulfate (Na_2SO_4), a drying agent, is added to the final solution and sodium carbonate to remove any residual solvent. Afterward, the sample is filtered and placed again on the rotary evaporator under vacuum at 40˚C with a small amount of ether or hexane to form a lipid film.

4.2.1.1. ***Phenol-Sulfuric acid test.*** The phenol-sulfuric acid test is a colorimetric quantitative assay test performed to determine carbohydrates concentration. It is widely used due to its simplicity, robustness, and accuracy. As

shown in Figure 11 [55], the basis of this method relies on the notion that when added, concentrated sulfuric acid breaks down poly or disaccharides into monosaccharides that are dehydrated into furfural or 5-hydroxymethyl furfural. The furan derivative will react with phenol forming a colored solution that has an absorbance at 490 nm [56].

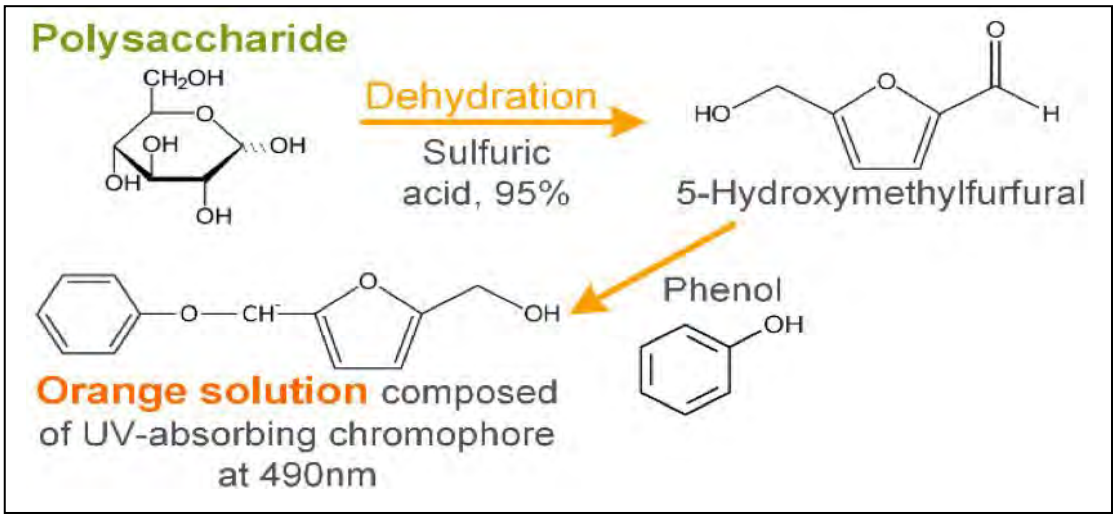

Figure 11: Mechanism of Phenol Sulfuric acid test [55]

2.1 mM Lactobionic acid stock solution is prepared by dissolving 75.2 mg of LA in 100 mL of distilled water. 5% phenol solution is prepared by dissolving 5 g of phenol in 95 mL of distilled water. The first step is performing a calibration curve for Lactobionic acid, 500 µL of 5 % phenol solution are added to 500 µL of Lactobionic acid aqueous solution (at different concentrations, as seen in Table 2) then vortex for 10 seconds. Afterward, 2.5 mL of concentered sulfuric acid and vortex for another 10 seconds (exothermic reaction). The solution should be left at room temperature for 30 minutes and the absorbance can be measured at 490 nm using a spectrophotometer. As seen in Figure 12, the more the carbohydrate concentration, the darker the color will be; hence having a higher absorbance reading, after performing the calibration curve, the same steps were followed as described above. Where for the sample 1 mg of DSPE-PEG-LA is dissolved in 500 µL of distilled water and 1 mg of DSPE-PEG-NH_2 (negative control) is dissolved in 500 µL of distilled water, afterward the phenol solution and sulfuric acid are added in the same concentrations and method as discussed above. A baseline solution is prepared by adding 2.5 mL sulfuric acid to 500 µL of distilled water.

Table 2: Calibration curve values

LA concentration (mM)	LA Stock solution (µL)	Distilled water (µL)
0	0	500
0.05	83	417
0.1	167	333
0.2	333	167
0.3	500	0

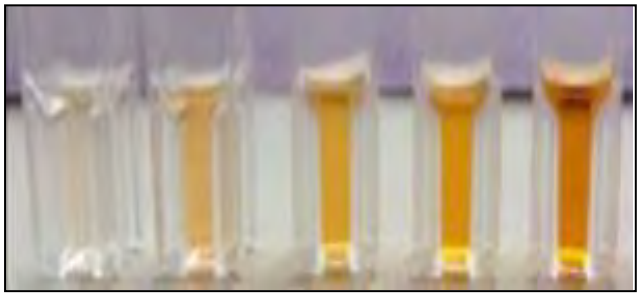

Figure 12: Calibration vials for phenol-sulfuric acid assay

4.2.1.2. ***Infrared (IR) Spectroscopy.*** IR Spectroscopy is used to determine various functional groups, by exciting molecules through infrared radiation. Different functional groups absorb light at different frequencies when exposed to IR radiation. Stronger bonds such as double or triple bonds will vibrate at a wavenumber that is higher than those of weaker bond, hence being able to determine the functional groups present [57]. The spectrophotometer emits infrared radiation on the sample, and the refracted light is detected, processed and displayed in a graph showing the transmittance % on the y-axis and the light wavelength(1/cm) on the x-axis, as illustrated in Figure 13 [58]. The IR Spectroscopy machine used is the FT-IR spectrometer from PerkinElmer (MA, USA).

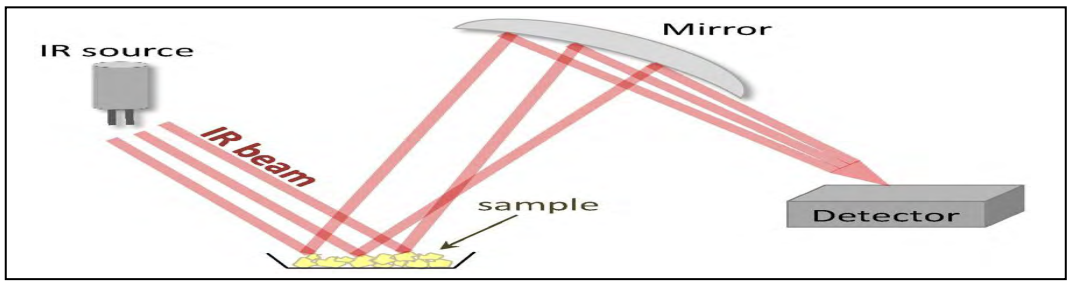

Figure 13: Infrared Spectroscopy [58]

4.2.2. Preparation of DSPE-PEG2000-Lac liposomes encapsulating calcein. The method that will be used is the lipid film hydration method with DSPE-PEG_{2000}-Lac, DPPC, and cholesterol in a molar ratio of 65:30:5 while maintaining the temperature at 60° C throughout the synthesis process. Four mL of chloroform is added to a round bottom flask to dissolve 5.56 mg of DSPE-PEG_{2000}-Lac. Afterward, 4.7 mg and 19.2 mg of cholesterol and DPPC are added, respectively. A rotary evaporator from Stuart equipment (Staffordshire, United Kingdom), is used to evaporate the chloroform at a set speed of 8 (around 152 rpm), under vacuum for 15 minutes at 50 ° C. The evaporation method results in a dry thin lipid layer. Next, a calcein solution is prepared by dissolving 40 mg of calcein disodium salt in 1.87 mL of PBS and 130 µL of 1M NaOH, adjustments using 0.1 M NaOH should be done to obtain a pH of 7.4. The calcein solution is then added to the lipid in the round bottom flask and into the rotary evaporator without vacuum for 50 minutes at a set speed of 5 (around 95 rpm) at 60 ° C, for the hydration step. The well-mixed solution will undergo sonication at 40 kHz using an Agar Scientific Ltd (Essex, United Kingdom) sonication bath for 2 minutes. The sonication is done to decrease the size of the liposomal spheres formed in the previous step. To homogenize the size of liposomes, sample extrusion is performed using an Avanti® Mini-extruder (Alabama, USA) with 0.2 µm polycarbonate filters for 31 times. The final step is filtration, a Sephadex G-100 gel filtration column hydrated with PBS and adjusted to a pH of 7.4, is used to filter the sample. The filtrate should be kept in a refrigerator at 4° C. The synthesis process is illustrated in Figure 14.

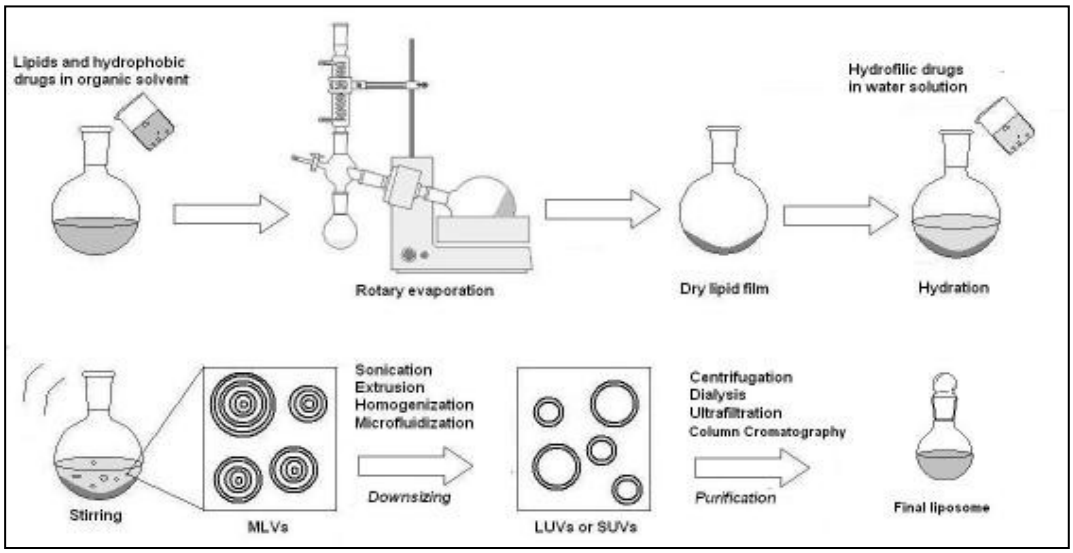

Figure 14: Lipid film hydration method [19]

4.2.3. Preparation of control liposomes of DSPE-PEG2000-NH2 encapsulating calcein. The only difference between preparation of control liposomes and the liposomes synthesized in section 4.2.2, is using DSPE-PEG_{2000}-NH_2 instead of DSPE-PEG_{2000}-Lac.

4.3. Particle Size by Dynamic Light Scattering (DLS)

15 µL of liposomes are diluted in 1 mL of PBS in a test tube, afterward, a portion is placed in the cuvette for analysis at room temperature. The DLS instrument is DynaPro® NanoStar™ from Wyatt Technology Corporation and is used to measure the hydrodynamic radius (R_h) of the liposomes prepared, as well as the molecular mass dispersity of the particles using the Poly Dispersity Index (PD). According to manufacture specifications, a PD % of less than 20 ensures that the particle is monodisperse.

DLS instrument emits a laser, at a wavelength of 658 nm, into the sample placed in the cuvette, Brownian motion of the nanoparticles will cause light to scatter, which is, in turn, sensed by a photon detector at a scattering angle of 90°. The signal is electronically processed, and the size distribution data is calculated and displayed [59].

4.4. Stewart Assay

The Stewart assay, named after John Charles Marshall Stewart, is a colorimetric test that can measure phospholipids concentration between the range of 0.01-1 mg. Ammonium ferrothiocyanate (FTC) reagent is an inorganic compound having a dark red color formed by dissolving ferric chloride hexahydrate and ammonium thiocyanate in DIW, Ammonium ferrothiocyanate forms a complex with phospholipids but does not form a homogenous solution with chloroform. The complex formed readily dissolves in chloroform and its intensity can be read using the Evolution™ 60S Ultraviolet-visible (UV-VIS) Spectrofluorometer from Thermo Fisher Scientific(MA, USA) at a wavelength of 485 nm, and accordingly the phospholipid concentration can be determined by preparing a calibration curve [60].

4.4.1. Stewart assay for standard calibration curve. First, the Ammonium ferrothiocyanate reagent is prepared by dissolving 2.7 g of Ferric Chloride Hexahydrate and 3 g of Ammonium Thiocyanate in a 100 mL of DIW. Afterward, a stock solution having a concentration of 0.1 mg/mL of DPPC in chloroform is prepared. As seen in

Table 3, dilutions (in duplicates) are made to cover the concentration range 0.0025 to 0.025 mg/mL from the stock solution, with a total volume of 2 mL with the addition of chloroform. Furthermore, 2 mL of the previously prepared Ammonium ferrothiocyanate reagent is added to each sample, the resultant solution consists of two visibly separated layers: the upper layer having the dark red Ammonium ferrothiocyanate reagent and the bottom having the chloroform solution with the dissolved complex. The clarity of the bottom layer is related to the amount of DPPC in the solution; the more the DPPC the less clear the solution is. A "blank" solution of 2 mL chloroform and 2 mL Ammonium ferrothiocyanate is also prepared as a baseline solution. Next, the samples are vigorously shaken for 20 s using a vortexer, then centrifuged at 1000 rpm for 10 minutes at 25 ^{o}C to ensure the separation between the two layers. The last steps are i) extracting the solution in the bottom layer using a glass Pasteur pipette, ii) transferring it to a glass cuvette and iii) reading its absorbance at 485 nm. Using the absorbance value of each sample and their equivalent known concentration, a calibration curve of DPPC concentration vs absorbance can be plotted.

Table 3: Stewart assay preparation

Vial	Stock (µL)	FTC (mL)	Chloroform (mL)
1	75	2	1925
2	125	2	1875
3	200	2	1800

4.4.2. Stewart Assay on Samples. After establishing the calibration curve, the prepared control liposomes (NH_2 liposomes) and LA-liposomes can be tested. 50 µL of liposomes are transferred to a 50 mL round bottom flask and then dried under vacuum for 15 minutes at 45 ^{o}C to eliminate any PBS in the liposomes. Afterward, 1mL of chloroform is added to the dried liposomes and sonicated for 20 minutes at 25^{o}C to thoroughly dissolve the dry lipid film in the solvent. In a similar procedure, as discussed in 4.4.1, 6 dilutions will be made (in duplicate) using the liposome solutions of both the control and targeted liposomes; samples will be vortexed, centrifuged and extracted to read their absorbance. The resultant absorbance values can be used to determine the DPPC concentration and hence the lipid concentration in each batch of liposome through the calibration curve.

4.5 Drug Release with Low-Frequency Ultrasound

As discussed in section 2.4.8, US is used for the controlled release of drug from liposomes. For this research, the nanocarriers synthesized are subjected to low-frequency ultrasound (20 kHz), to observe the principle of cavitation, at three different power intensities, namely 7.46, 9.85, and 17.31 mW/cm^2 (the setting on the transducer being 20%,25%, and 30%). The mode of operation will be in pulses to avoid hyperthermia. Calcein has fluorescence properties which can be detected by a Spectrofluorometer. A QuantaMaster QM 30 Phosphorescence Spectrofluorometer from Photon Technology (California, USA) and a US probe model VC130PB from Sonics & Materials Incorporated (Connecticut, USA) will be used.

75 µL of liposomes are diluted in 3 mL of PBS in a cuvette. The cuvette is then placed for analysis in the Spectrofluorometer. The US probe is placed in the cuvette, and a baseline line reading is acquired for the first 1.10 min, before US is applied, afterward, US is turned on while alternating between turning it off for 10 seconds and on again for 20 seconds (the total duration is 5 minutes and 20 seconds). The initial fluorescence level is low since calcein self-quenches at high concentrations. The "pulsed" application is to avoid the damaging hyperthermic effects of prolonged US exposure. With each pulse, the structural integrity of the liposome will be affected hence gradually releasing its content with time, which is reflected by increased fluorescence intensity. On the other hand, during the off period of US, the fluorescence does not increase (indicating no release). The increased fluorescence intensity will follow this behavior until a maximum release is reached at equilibrium. Finally, 50 µL of Triton X-100, a detergent, is added to the sample to lyse the liposomes resulting in 100% release of the encapsulated calcein. After the normalization of the data the Cumulative Fraction Release can be calculated using Equation (1):

$$CFR = \frac{*+,-+./,0\ 1,,/2-,341.-5/+-\ /+,-+./,0}{*+,-+./,0\ 1,677\%\ 9\text{-}5\text{-}1.-341.-5/+-\ /+,-+./,0} = \frac{12:;+.:<=9;>\ 9\text{-}5\text{-}1.-=\ 1.,/2-.(@_A)3/+/,/15=9;>\ 12:;+.(@_C)}{,:,15=9;>\ 12:;+,(@_D)} \quad (1)$$

4.6. Statistical Analysis

Results obtained from all tests will be statistically analyzed using functions available on Microsoft Excel. Finding the average, standard deviation and comparison

between two samples using t-test while assuming equal variances will be used. A p-value less than 0.05 will be considered to indicate a significant difference between two values hence rejecting the null hypothesis.

4.7. Release Kinetics

In drug delivery systems, the controlled release of the drug from the nanocarrier is an extremely important component of the technology. But the behavior of the release in terms of duration and rate is equally important. A successful drug release behavior aims at reducing the side effects and enhance drug efficacy. Therefore, mathematical kinetic modeling is a vital step to obtain the optimum form of controlled drug release. In this research, nine model dependent methods will be tested and fitted to obtain the best fit line. These models are Zero- order, First-order, Higuchi, Hixon-Crowell, Korsmeyer-Peppas, Baker-Lonsdale, Weibull, Hopfenberg and Gompertz [61], [62].

4.7.1. Zero-order model. In this model, the dissolution drug profile is slow and independent of concentration; the amount of released drug (C) per unit time (t) is constant (zero-order release constant k_o), as seen in Equation (2). Applying mathematical integration to Equation (2), by setting the time limit for 0 to t and the amount of released drug from the initial drug amount (C_o) to amount of drug released at time t (C_t), will result in Equation (3)

$$\frac{=@(,)}{=,} = k_7 \tag{2}$$

$$C, = C: + k:\mathrm{t} \tag{3}$$

Therefore, using the zero-order model for the normalized release data can be plotted as the Cumulative Fraction Release (CFR) versus time in seconds with a positive slope of $\frac{\mathrm{G^C}}{@_\mathrm{D}}$ by relating Equation (3) to CFR calculation found in Equation (1), as seen in Equation (4).

$$CFR = \frac{\mathrm{G^C}}{@_\mathrm{D}}\mathrm{t} \tag{4}$$

4.7.2. First order model. Drug release having a first-order kinetic model will follow the first order Equation (5), with k being the first order release constant and C the drug amount. For this release kinetics, the amount of drug per unit time is dependent on concentration, unlike the zero-order model.

$$\frac{=@}{=,} = -kC \tag{5}$$

Applying mathematical integration to Equation (5), by setting the time limit from 0 to *t* and the amount of released drug from the initial drug amount (C_o) to amount of drug released at time *t* (C_t), will result in Equation (6)

$$ln\frac{@^{A}}{@_{C}} = -kt \tag{6}$$

Through mathematical manipulation of Equation (6) and by relating it to CFR calculation found in Equation (1), a relation is obtained in Equation (7), which can be further manipulated in order to be linearized and the release data can be plotted as the natural logarithm of (CFR) versus time in seconds, as seen in Equation (8)

$$CFR = \frac{@^{L}}{@_{D}}(e^{3G,} - 1) \tag{7}$$

$$ln(CFR) = ln\,0\frac{@^{L}}{@_{D}}P - kt \tag{8}$$

4.7.3. Higuchi model. The Higuchi model describes the drug release from a matrix system, which in this research is liposomes. In this model, several assumptions have been made, such as constant drug diffusion, drug particle size is smaller than the encapsulating liposomes and one-dimensional release. Equation (9) represents the Higuchi model, where *C* is the amount of released drug/unit area *A* at time *t*, *D* is the diffusion coefficient for the drug particle in liposomal solution, C_0 is the initial drug amount and C_s is the drug solubility in the liposomal solution:

$$C = AR\overline{D(2C_U - C.)C.t} \tag{9}$$

The Higuchi constant (k_h) is defined as $AR\overline{D(2C_U - C.)C.}$ resulting in Equation (10):

$$C = k_V\sqrt{t} \tag{10}$$

Through mathematical manipulation of Equation (10) and by relating it to CFR, a relation is obtained in Equation (11), The drug release data can be plotted as Cumulative Fraction Release (CFR) versus square root of time in seconds with a slope of $\frac{G^{X}}{@_{D}}$:

$$CFR = \frac{G^{X}\sqrt{}}{@_{D}} - \frac{@^{L}}{@_{D}} \tag{11}$$

4.7.4. Hixson-Crowell model. This model represents the behavior of released drug when there is a change in the surface area and diameter of a spherical particle. Equation (12) demonstrates the Hixon-Crowell model, where W_0 is the initial weight fraction of drug, W_t is the dissolution weight fraction of drug at time t and k is the surface-area constant:

$$W_0^{1/3} - W_t^{1/3} = k_{HC}t \quad (12)$$

Through mathematical manipulation and by relating it to CFR, Equation (12) can be employed to plot the release data as $[100* (1\text{-}CFR)^{1/3}]$ versus time in seconds from the following Equation (13):

$$100(1 - CFR)^{1/3} = 1 - k_{HC}t \quad (13)$$

4.7.5. Korsmeyer-Peppas model. The model, which follows power-law kinetics, explains the drug release from a polymeric system through Equation (14), where M_t/M_∞ is the fraction of drug release, t is time, n is the release exponent, and k is the release constant:

$$\frac{M_t}{M_\infty} = kt^n \quad (14)$$

Through mathematical manipulation, drug release data can be plotted as the natural logarithm of CFR versus the logarithm of time in seconds using the following Equation (15) with a slope of n.

$$log(CFR) = log(k_{cd}) + n\,log(t) \quad (15)$$

4.7.6. Baker-Lonsdale model. The Baker-Lonsdale model represents the release from spherical homogenous packed matrices, as shown in Equation (16), where M_t/M_∞ is the fraction of drug release, t is time, n is the release exponent, and k_{BL} is the Baker-Lonsdale release constant:

$$\frac{3}{2}\left[1 - \left(1 - \frac{M_t}{M_\infty}\right)^{2/3}\right] - \frac{M_t}{M_\infty} = k_{BL}t \quad (16)$$

By assuming that initially there is no drug release, one can imply that $CFR = \frac{M_t}{M_\infty}$, transforming Equation (16) into:

$$\frac{3}{2}\left[1 - (1 - CFR)^{2/3}\right] - CFR = k_{BL}t \quad (17)$$

Where $k_{4i} = \frac{[1^{m@_{mn}}}{9^{g}_{L}@_{L}}$ in terms of D_2 is the diffusion coefficient, $C_{2.}$ is the drug solubility in the matrix, r_7 is the radius of the spherical matrix, C_7 is the initial concentration of the drug in the matrix. Therefore, the release data can be plotted as 1.5*[1-(1-CFR)$^{2/3}$]-CFR versus time in seconds with a slope of k_{BL}.

4.7.7. Weibull model. The Weibull model can be applied to different drug release curves, and is related to fractal kinetics, starting with the differential Equation (18), where M_t is the drug released at time t, M_∞ is the total amount of drug released, t is time, b is the shape of the dissolution curve, a is time-dependent scale parameter that can be found from a calibration curve at t=1, and T is lag time and is mostly assumed to be zero.

$$M_{,} = M_{q}[1 - exp^{3\frac{(AuD)^{v}}{w}}] \quad (18)$$

Through mathematical manipulation, Equation (18) can be used to plot the release data as log [–natural logarithm (1-CFR)] versus log time in seconds with a slope of b and a y-intercept of -log(a).

4.7.8. Hopfenberg model. This model describes oily polymers that undergo erosion and degradation while keeping surface area constant. For this research, a spherical polymer will be studied. Equation (19) represents the model:

$$\frac{M_t}{M_\infty} = 1 - [1 - \frac{G^{C_o}}{@_C 1_C}]^{+} \quad (19)$$

Where M_t/M_∞ is the fraction of drug release, t is time, and k_o is the corrosion rate constant, C_o is the initial drug concentration, a_o is the initial radius of the sphere and n takes a value of 3 for a spherical polymer. By assuming that initially there is no drug release, one can imply that $CFR = \frac{M_t}{M_\infty}$, and by equating k_{HF} to $\frac{G_{C_o}}{@_C 1_C}$, Equation (19) is transformed into:

$$CFR = 1 - [1 - k^{\wedge}{}_{y}]^{[} \quad (20)$$

Through mathematical manipulation, Equation (20) becomes Equation (21) hence a plot 1-(1-CFR)$^{1/3}$ versus time in seconds will have a slope of $k_{HF.}$

$$1 - (1 - CFR)^{\frac{\setminus}{]}} = k^{\wedge} < t \quad (21)$$

4.7.9. Gompertz model. Explains the dissolution profile *in vitro*, for an intermediate drug release rate. Equation (22) represents the Gompertz model:

$$X(t) = X_{\_1\{} exp\ [-\alpha e^{\}5:>\text{,}}] \qquad (22)$$

Where *X(t)* is the fraction of drug release at time *t*, X_{Max} is the maximum fraction of drug release, α is the portion of the undissolved drug, β is the shape parameter of dissolution rate/unit time and *t* is time. Through mathematical manipulation, Equation (22) can be used to plot (ln [-ln (CFR)]) versus log time in seconds.

Chapter 5. Results and Discussion

In this chapter, the results of the experiments done will be displayed and analyzed

5.1. Attachment Confirmation

5.1.1. Phenol-Sulfuric acid assay. As discussed in section 4.2.1.1 the phenol-sulfuric acid assay test is a commonly used colorimetric assay test used to quantify the concentration of carbohydrates in a given sample by performing a calibration curve and reading the absorbance at 490 nm. Zeng et. al has used this assay to confirm the galactose residues after conjugating Lactobionic acid to gold nanoparticles [63]. The assay was performed for three different batches of DSPE-PEG_{2000}-Lac and the results are shown in Table 4 along with the calibration curves (Figures 15-17) obtained that are later used to calculate the mass of LA in the sample. The phenol-sulfuric acid test has confirmed the attachment of Lactobionic acid inside the sample with minimal interference from any other components. The results showed an average of 14% attachment of Lactobionic acid to DSPE-PEG-NH_2 for the 3 batches tested.

- Sample calculations on % attachment for Batch 2:

  ⇒ From the calibration curve obtain LA concentration in sample=$\frac{7.N7Ä37.767Å}{N.Ç[N[} = 0.095\ mM.$

  ⇒ Mass of attached LA in sample=$0.095(mM) * 500(\mu L) *$ $3148.786\ O\frac{\geq}{2:5}P * 10^{3Ä} = 0.15\ mg$

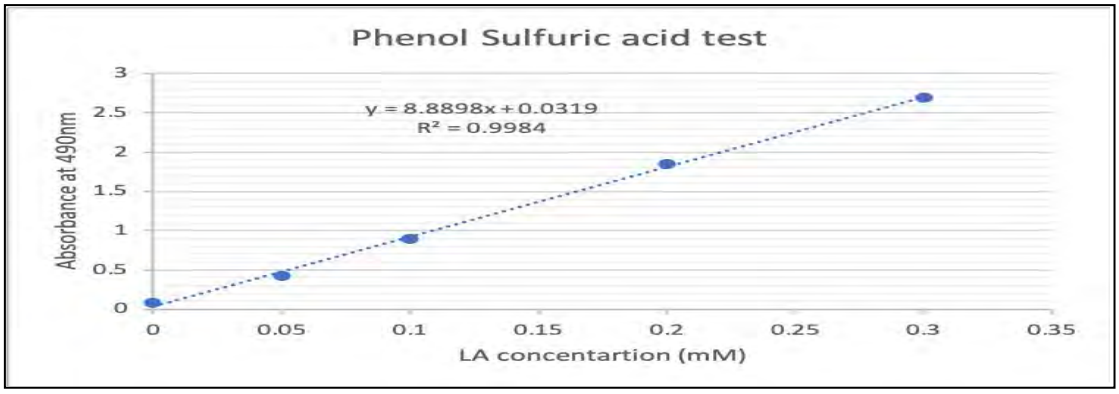

Figure 15: Lactobionic acid calibration curve (Batch 1)

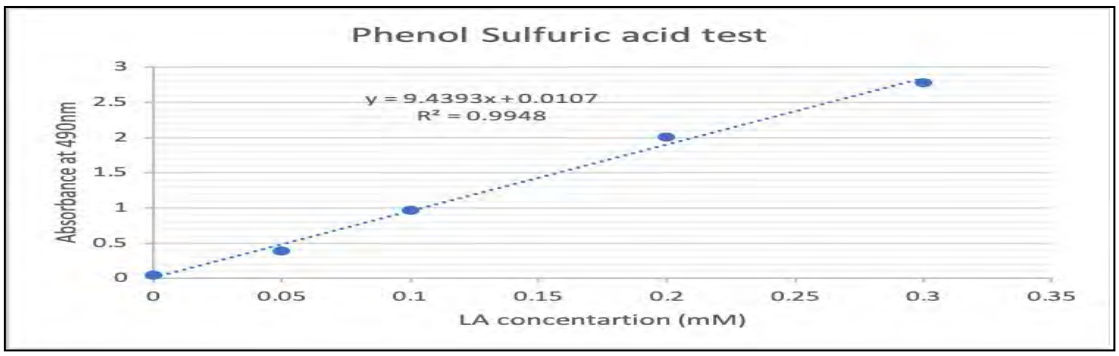

Figure 16: Lactobionic acid calibration curve (Batch 2)

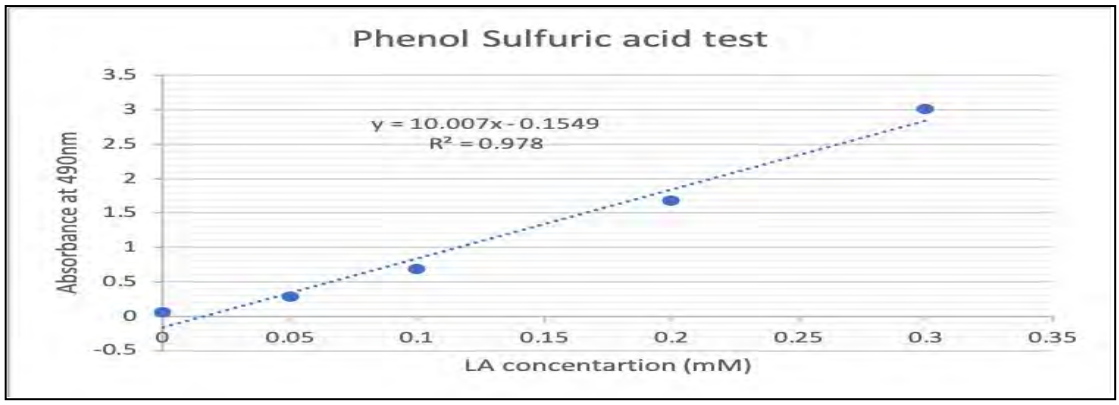

Figure 17: Lactobionic acid calibration curve (Batch 3)

Table 4: Results of phenol-sulfuric acid assay

	Batch 1	**Batch 2**	**Batch 3**
LA concentration (mM)	**Absorbance at 490 nm**	**Absorbance at 490 nm**	**Absorbance at 490 nm**
0	0.079	0.044	0.056
0.05	0.425	0.389	0.286
0.1	0.895	0.965	0.686
0.2	1.849	2.012	1.682
0.3	2.69	2.779	3.02
DSPE-PEG-NH_2 Absorbance at 490 nm	0.115	0.119	0.155
Sample Absorbance Absorbance at 490 nm	0.52	0.906	0.873
% Attachment	11	15	16
Average % attachment	14	**Std. deviation**	2.16

5.1.2. Infrared (IR) Spectroscopy. Infrared Spectroscopy was also used to confirm the attachment of Lactobionic acid molecule to DSPE-PEG-NH2 in order to

have a conjugated nanocarrier. The results shown in Figure 18 compares a sample of DSPE-PEG-NH2 (negative control) in orange and the conjugated sample of DSPE-PEG-LA in blue. The peak at 1661 cm^{-1} represents the C=O amide bond formed, and 800 cm^{-1} represents the galactose ring C-O-C bond, hence confirming the attachment. The results obtained are similar to the findings of Bansal et al. [64] and Wiercigroch et al [65].

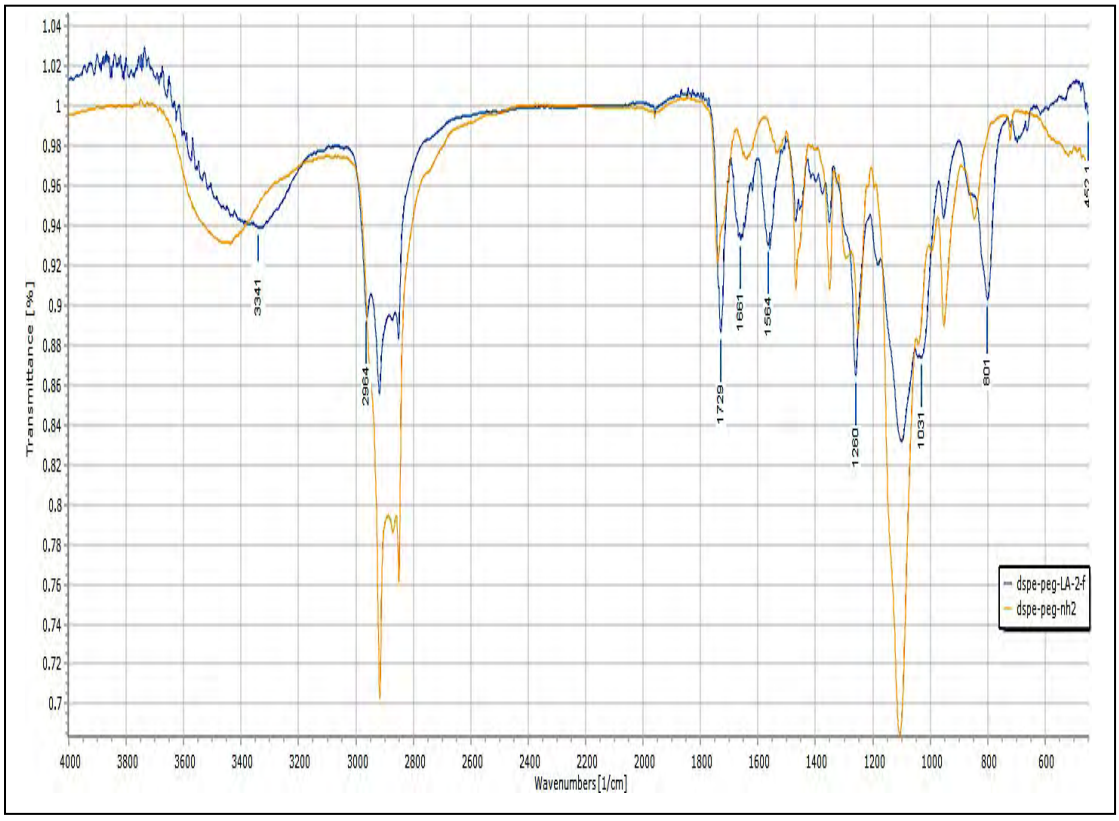

Figure 18: IR results

5.2. Dynamic Light Scattering (DLS)

Dynamic Light Scattering is used to obtain the size and size distribution of the liposomes. As shown in Tables 5 and 6, results indicated that the size of the liposomes has an average of 85.8±1.24 nm and 89.6±2.72 nm for control and LA liposomes respectively. A sample of the size distribution graph obtained from each form of liposomes is shown in both Figures 19 and 20. Having the size of LA liposomes larger than the control liposomes is consistent with other research papers found in literature,

such as the paper on oxaliplatin-loaded hepatoma- targeted liposome coupled with Lactobionic acid by Bansal et.al [64]. Furthermore, the increased size of LA liposomes is an indication and confirmation of the attachment of Lactobionic acid to the liposome.

Table 5: Control liposomes DLS results

Batch number	Radius(nm)	% PD
Batch 1	87.5	12.6
Batch 2	85.0	12.2
Batch 3	84.8	13.1
Average	**85.8**	**12.6**
Standard Deviation	**1.24**	**0.38**

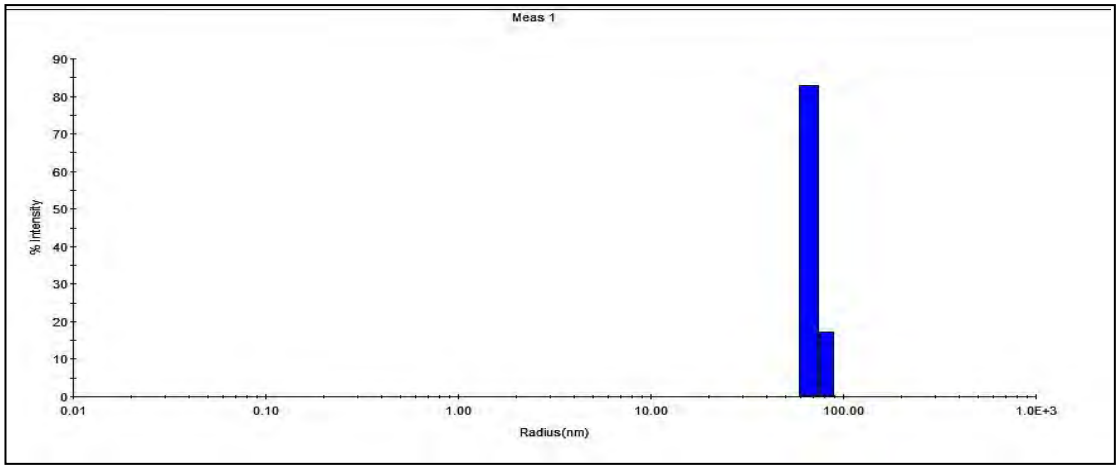

Figure 19: Size distribution for NH_2 liposomes

Table 6: LA liposomes DLS results

Batch number	Radius(nm)	% PD
Batch 1	91.3	11.2
Batch 2	91.8	11.6
Batch 3	85.8	12.1
Average	**89.6**	**11.7**
Standard Deviation	**2.72**	**0.37**

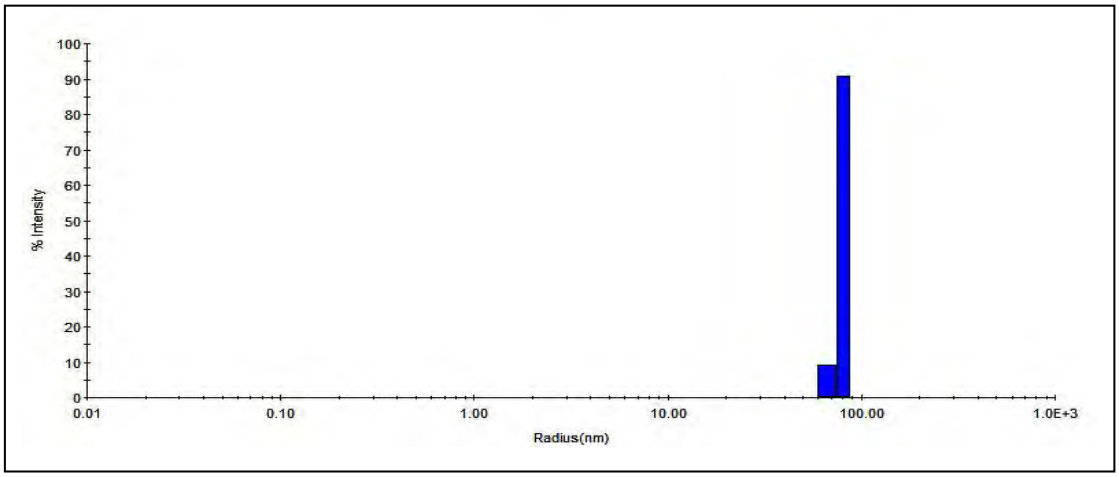

Figure 20: Size distribution for LA liposomes

Figure 21 shows a Transmission Electron Microscopy (TEM) image of a control liposome, confirming that the followed protocol results in a small Unilamellar vesicle with a size range of a 100 nm.

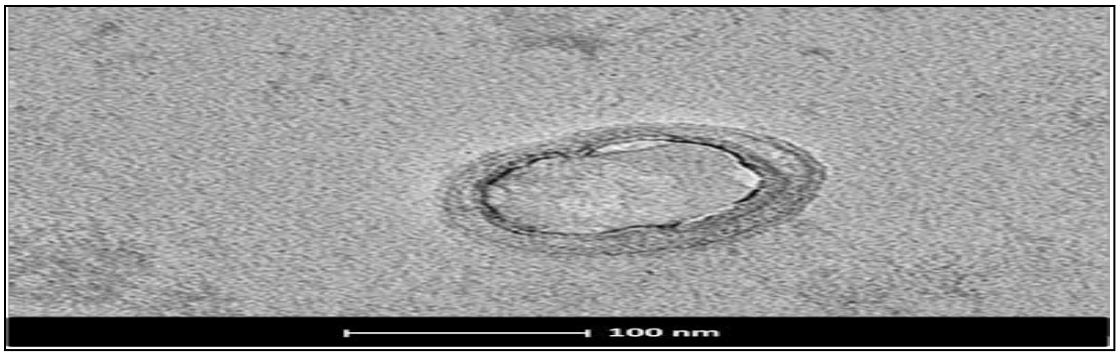

Figure 21: TEM image of prepared liposome

5.3. Stewart Assay

Stewart assay is a colorimetric quantitative assay test responsible for measuring the lipid content. The calibration curve shown in Figure 22 is used to determine the amount of lipid found in the prepared liposomes. NH_2 liposomes had an average DPPC content of 7.3 mg, while LA liposomes had 6.6 mg of DPPC on average which is the main lipid component of the formed liposomes, as shown in Tables 7 and 8. Figure 23 is a screenshot of the results obtained from the UV spectroscopy for batch 3, showing

a clear overlap between the control liposomes (1,2,3) and LA liposomes (4,5,6) at increasing concentrations.

Table 7: DPPC calibration test

DPPC (mg/ml)	DPPC (mg)	Absorbance at 485 nm
0.0025	0.01	0.04965
0.005	0.02	0.10255
0.01	0.04	0.2329
0.015	0.06	0.34435
0.02	0.08	0.4695
0.025	1	0.58995

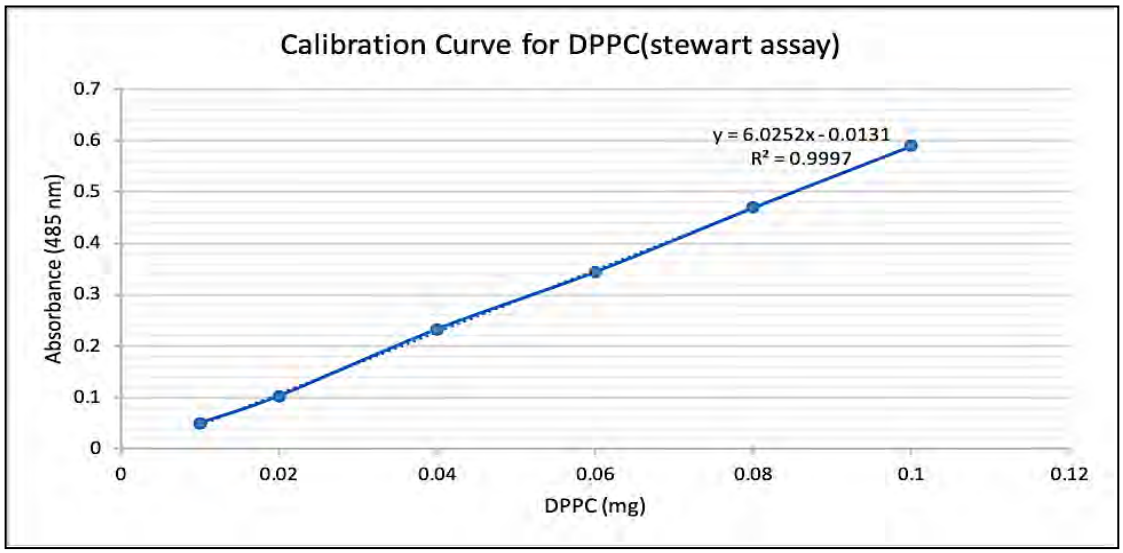

Figure 22: Calibration Curve for DPPC (Stewart assay)

Table 8: Stewart Assay results

Batch number	Control liposomes	LA Liposomes
	DPPC (mg)	
Batch 1	9.0	8.2
Batch 2	7.5	6.3
Batch 3	5.4	5.4
Average	7.3	6.6
Standard Deviation	1.5	1.2

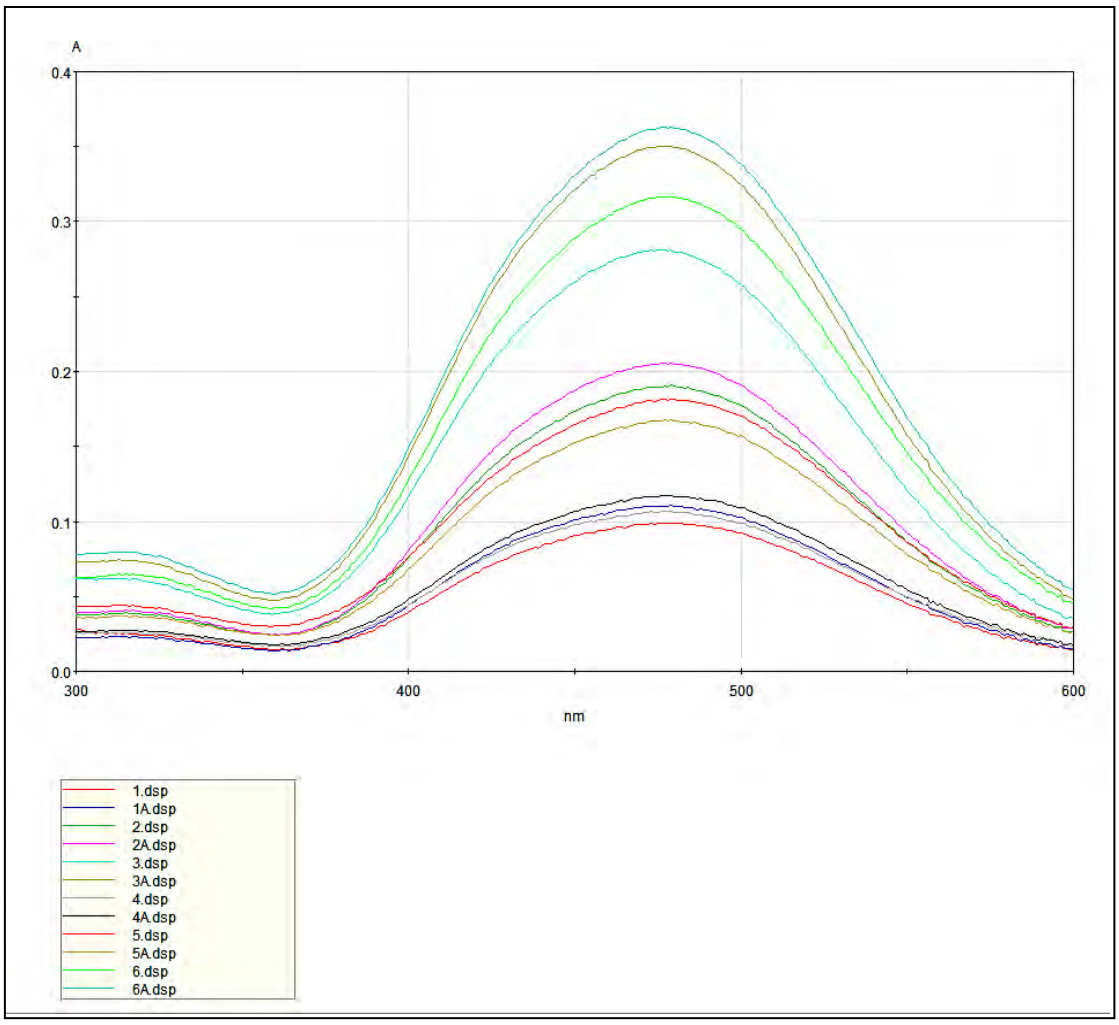

Figure 23: Screenshot from UV Spectrofluorometer done for Stewart assay test

5.4. Low Frequency Ultrasound Release

Figure 24, a screenshot of the online release data performed before normalization, shows the release of encapsulated calcein through the use of low-frequency US at three power intensities of 7.46, 9.85 and 17.31 mW/cm^2. The fluorescent of calcein is measured with time using the Spectrofluorometer. A baseline (of self-quenching) is established for the first 1.10 min, afterwards, the sonication begins. A pulsation mode is employed where the US is turned on for 20 s and off for 10 s for a total duration of 5 minutes. Finally, Triton-X is added for the final liposome lysis and the measurement continues for another 20 s corresponding to 100% release.

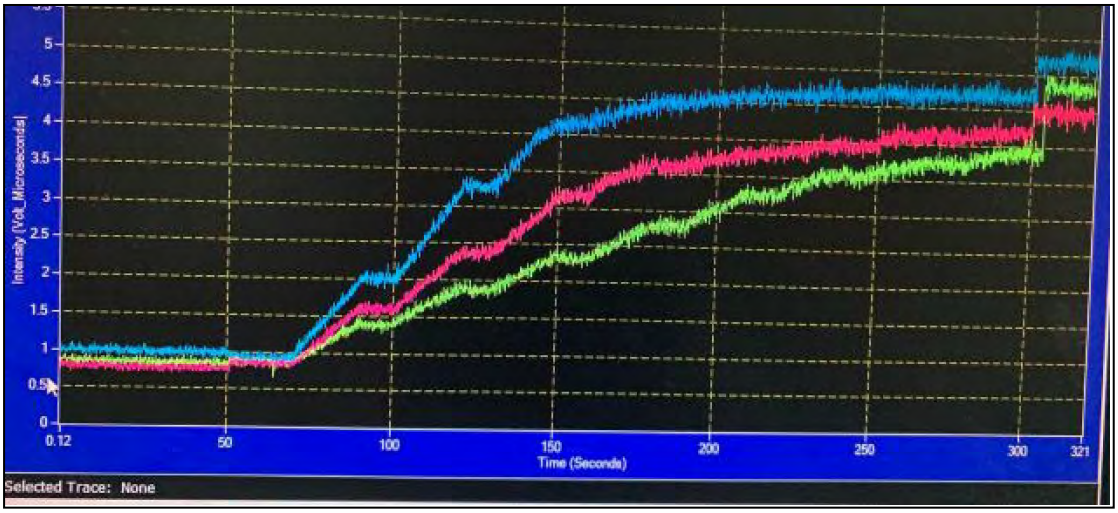

Figure 24: Screenshot of online release for control liposomes

Figures 25 and 26 represent the normalized and averaged release data of 3 batches with 3 repetitions at each power intensity for NH_2 and LA liposomes respectively, when plotted for Cumulative Fraction Release (CFR) versus time in seconds. As seen in the Figures, the baseline line region (first 1.10 min) show no change in release, however as soon as US is applied the CFR is increasing with time representing the increased release of calcein along with each pulse for the 20s on period, and then plateauing during the 10 s off period. Similar behavior is observed for both control and LA liposomes verifying that the mechanical effects of low frequency ultrasound are triggering drug release and proving their sensitivity to the ultrasound waves with increasing power intensity. Furthermore, the plateauing during the off periods indicates that the liposomes are encapsulating the remaining drug by self-assembly. The addition of the surfactant (Triton-X) will lower the surface tension between the fluids, leading to the total rupture of the liposome hence reaching a maximum release of a 100%.

It must be noted that the reason behind using low frequency ultrasound is to be able to observe the principle of cavitation without the interference of hyperthermia that is caused by high frequency ultrasound. Furthermore, the pulsation mode applied here is a precaution that must be taken since continuous exposure to ultrasound might be unsafe to patients in the long run.

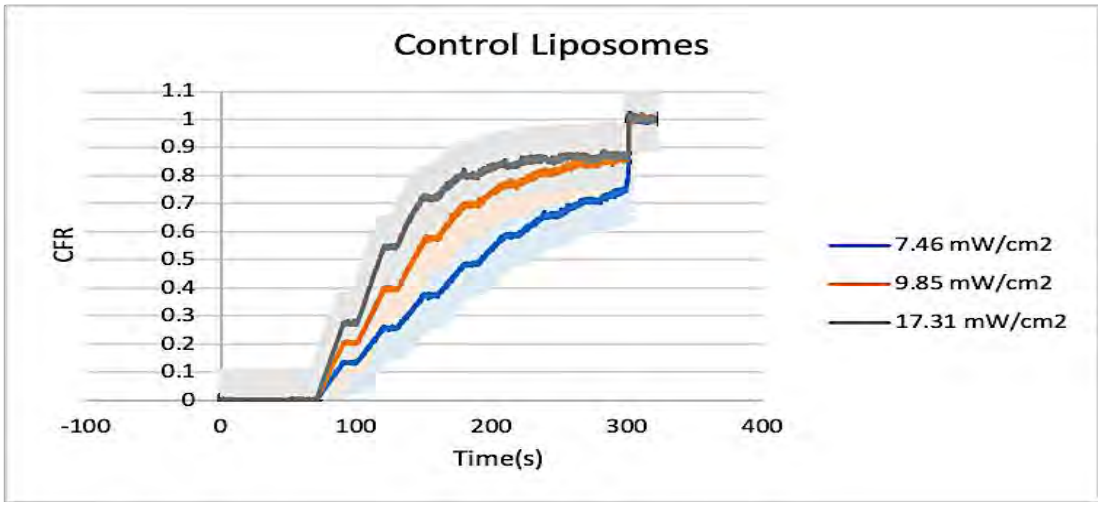

Figure 25: Low frequency US release for control liposomes

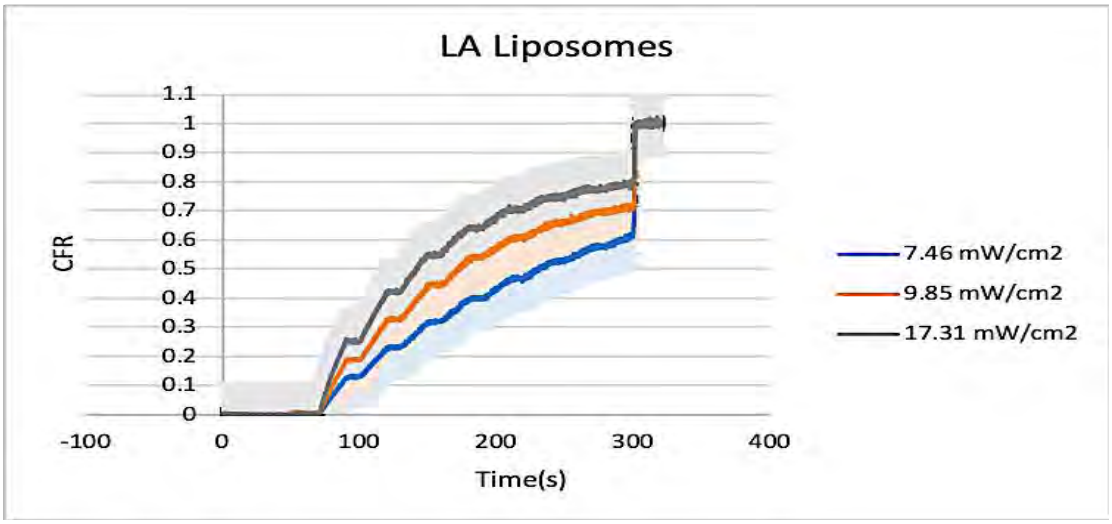

Figure 26: Low frequency US release for LA liposomes

In order to zoom in and have a clearer image of the effect of power intensity on drug release, Figures 27 and 28 represent the average CFR of each the 1st pulse, 2nd pulse and final release versus the three power intensities. An increasing trend is seen in the blue and orange lines representing the first and second pulses respectively, showing that a higher power intensity will in turn increase release, confirming the sensitivity of the liposomes to the power carried by ultrasound waves. On the other hand, through visual observation, the maximum release at 100% does not vary with power intensity, since total liposomal lysis occurred at that point of time.

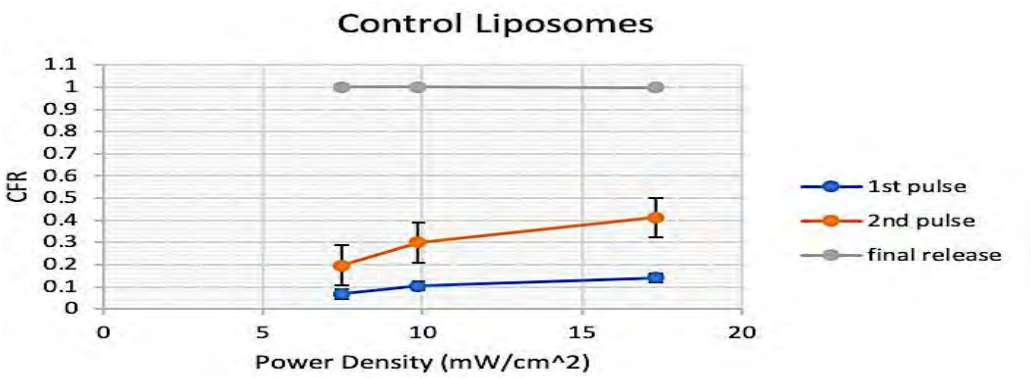

Figure 27: Comparison between first two pulses and final release with increasing power intensity for control liposomes

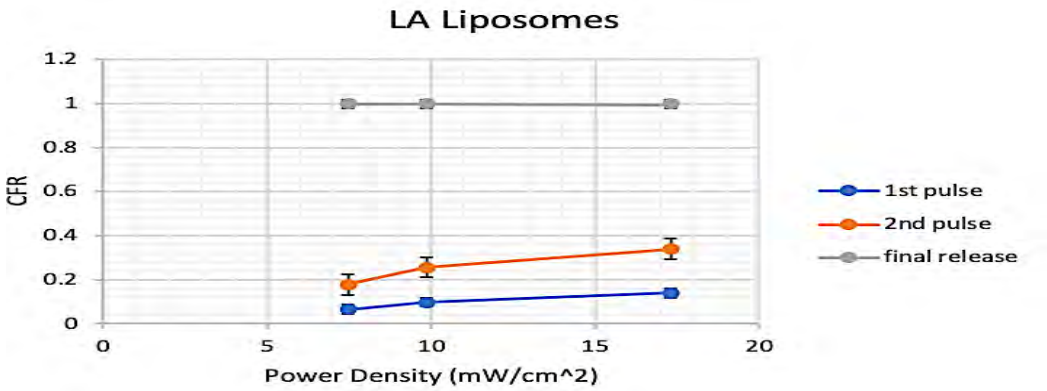

Figure 28: Comparison between first two pulses and final release with increasing power intensity for LA liposomes

It is clearly shown that the sequential pulsation has a direct effect on release for all the power intensities tested which confirms the occurrence of cavitation due to US exposure. Another comparison was performed by measuring the % of drug release with each of the first four pulses. In this study, control liposomes and LA liposomes had different behaviors. As seen in Figure 29, the first three pulses follow an increasing trend of release for all power intensities, but a slight drop in release at the 4th pulse for the last two power intensities. The variation might be due to the fact that the higher power intensities were able to release more of the drug with the first 3 pulses, hence lowering the amount of drug release by the 4th pulse in the case of control liposomes. On the other hand, when the same study was performed for LA liposomes (Figure 30), the pulses seem to release at similar %, while reserving the increasing effect of power

intensity. The difference in behavior between the two forms of liposomes indicates that the addition of the LA moiety did change the release mechanism by potentially stabilizing the liposomes and forming micelles that encapsulated any free drug.

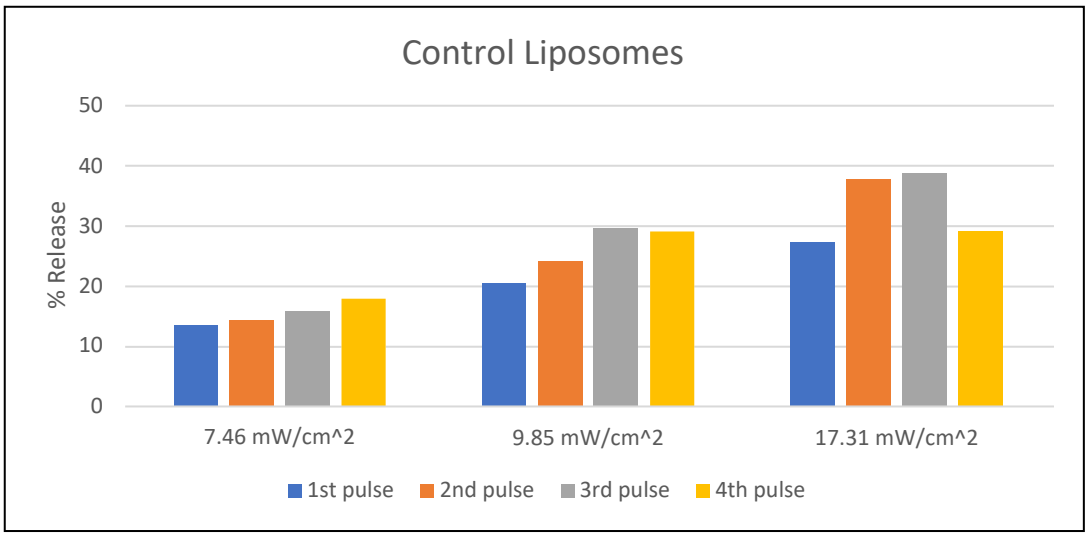

Figure 29 Percentage of drug release with each pulse at each power intensity for control liposomes

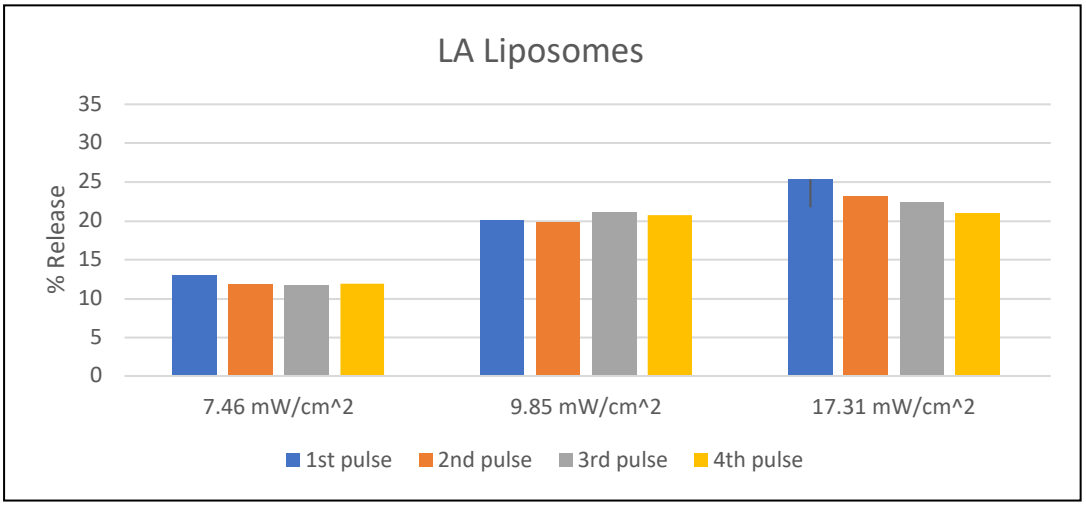

Figure 30: Percentage of drug release with each pulse at each power intensity for LA Liposomes

Comparing control liposomes and LA liposomes in terms of % release, as seen in Figure 31, the % release was compared for the two types of liposomes for the first four US pulses at each power intensity. It can be seen graphically that the amount of

drug released by control liposomes is always greater than that released by LA liposomes. the LA moiety is considered as a small molecule with a molecular weight of around 358 g/mol in comparison to other ligands such as transferrin or hyaluronic acid having a molecular weight in the thousands of Daltons range. However, the size of LA liposomes did have a statistically significant increase when compared to control liposomes with a p-value of 0.01, the slight size increase could have been the reason behind the hindered release amount, attributing it to the fact that the LA moiety added to the stability of the liposome and hence decreased its sonosensitivity, but was not significant enough to damage the integrity of the liposomal formation or bilayer which might result in increased release.

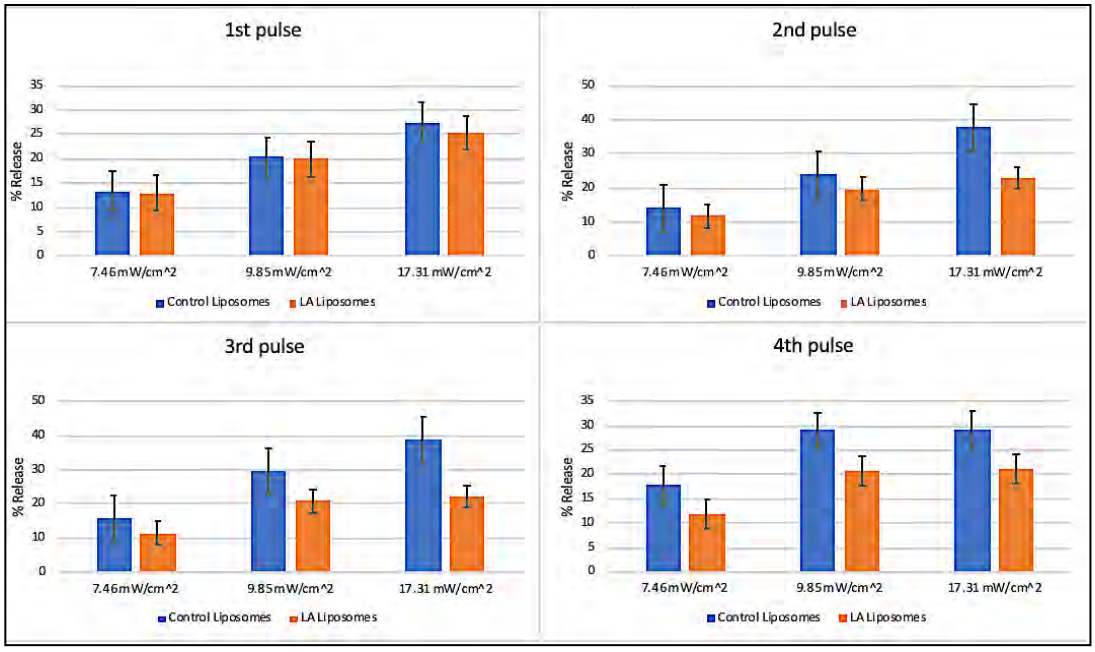

Figure 31: Comparision between the percentage of drug release for the first 4 pulses at each power intensity for control and LA liposomes

As discussed earlier on in this section, the addition of Triton-X is meant to cause the complete destruction of the liposomal integrity, the phenomenon of control liposomes releasing more drug than LA liposomes ended by the addition of the surfactant and this can be seen in Figure 32. The maximum release is graphically observed to be similar for both types of liposomes and at all power intensities.

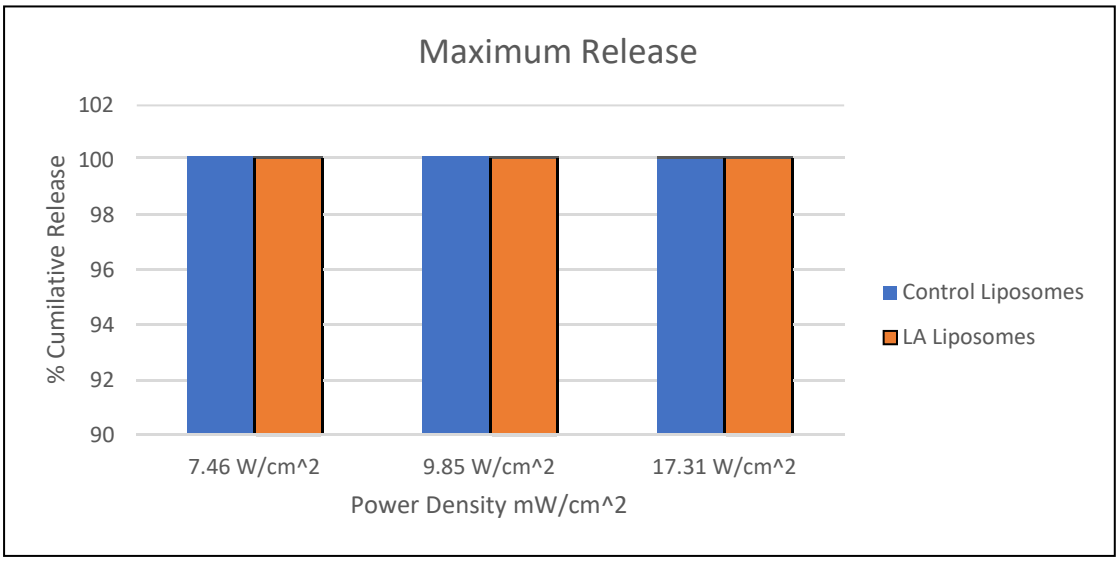

Figure 32: Comparision between the maximum release at each power intensity for control and LA liposomes

Further statistical analyses were performed to understand the difference or similarity between the diverse factors involved in the drug release study. Tables 9 to 11 are heat maps to presenting the extent of statistical difference by color variation, through cross-comparison between pulsation and power intensity for control liposomes and LA liposomes alone and combined. Using Tables 9 and 10, it can be concluded that is a significant difference (p-value < 0.05) between release at the two higher power intensities and that at the lowest regardless of the liposome type, which was previously observed graphically in Figures 24 and 25. However, comparison between 25% and 30% (equivalent to 9.85 and 17.31 mW/cm^2) showed no statistically significant differences (p-value > 0.05), indicating that liposomes will release approximately similar amounts at 9.85 and 17.31 mW/cm^2.

Table 11 shows that for the 1st pulse there was no significant difference between the LA liposomes and control liposomes regardless of the acoustic power density, which might be explained that the initial release response is common for both but with continued pulsation the physical and chemical changes discussed earlier will manifest more and start altering the subsequent release behavior, hence having a significant difference in the next 3 pulses. In term of maximum release, no statistically significant difference was observed between both types of liposomes and all power intensities which was previously graphically shown in Figure 31.

Table 9: Heat map of p-test on control liposomes for the first 4 pulses and maximum release at 3 power intensities

Control liposomes	1st pulse	2nd pulse	3rd pulse	4th pulse	Max. Release
% Intensity	p-value				
20% and 25%	1.7E-08	2.6E-11	1.39E-07	1.9E-07	0.9726
20% and 30%	9.6E-11	2.9E-11	5.3E-12	0.0019	0.1054
25% and 30%	2.3E-06	2.3E-07	0.006	0.7238	0.8543
p<0.01	0.01<p<0.05			p>0.05	

Table 10: Heat map of p-test on LA liposomes for the first 4 pulses and maximum release at 3 power intensities

LA Liposomes	1st pulse	2nd pulse	3rd pulse	4th pulse	Max. Release
% Intensity	p-value				
20% and 25%	1.4E-06	2.5E-05	6.8686E-05	0.00035854	0.8793
20% and 30%	1.96E-07	1.7E-07	1.3948E-07	6.3331E-07	0.9673
25% and 30%	0.0017	0.0820	0.52900805	0.90067669	0.5085
p<0.01	0.01<p<0.05			p>0.05	

Table 11: Heat map of p-test on the comparison between control and LA liposomes for the first 4 pulses and maximum release at 3 power intensities

Control and LA Liposomes	1st pulse	2nd pulse	3rd pulse	4th pulse	Max. Release
% intensity	p-value				
20%	0.6399	0.0003	7.95E-07	1.2E-06	0.6759
25%	0.6060	0.01452	0.0022	0.0015	0.4436
30%	0.2066	1.6E-06	5.05E-07	0.0068	0.8099
p<0.01	0.01<p<0.05			p>0.05	

5.5. Kinetic Modeling

Nine kinetic models were applied to the online release data, the plots were linearized, plotted versus a function of time in seconds, and the best fit models were chosen. Best fit models were selected according to the highest coefficient of determination (R^2) obtained after plotting the best fit line for each model. Weibull

model was found to give the highest R^2 in comparison to the other models for the control liposomes and LA liposomes and all power intensities. Hence it was determined that the release profiles follow the Weibull model. Figures 33-41 show the plots obtained for all 9 models for a batch of LA liposomes at a power intensity of 9.85 mW/cm^2. Remaining Figures can be found in Appendices A to F. Tables 12 and 13 contains the values of R^2 obtained from all models, showing Weibull having the highest correlation coefficient.

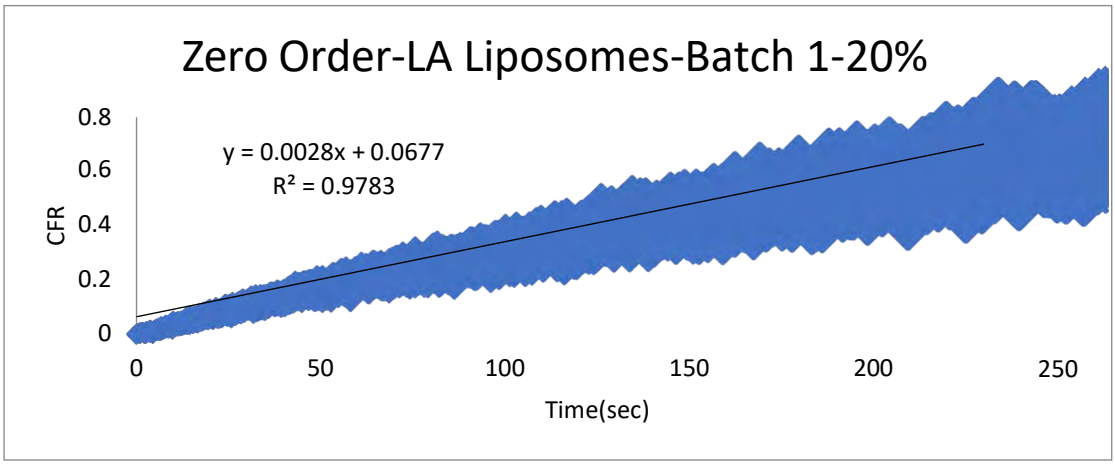

Figure 33: Zero-Order model applied on LA liposomes for a power intensity of 7.46 mW/cm^2

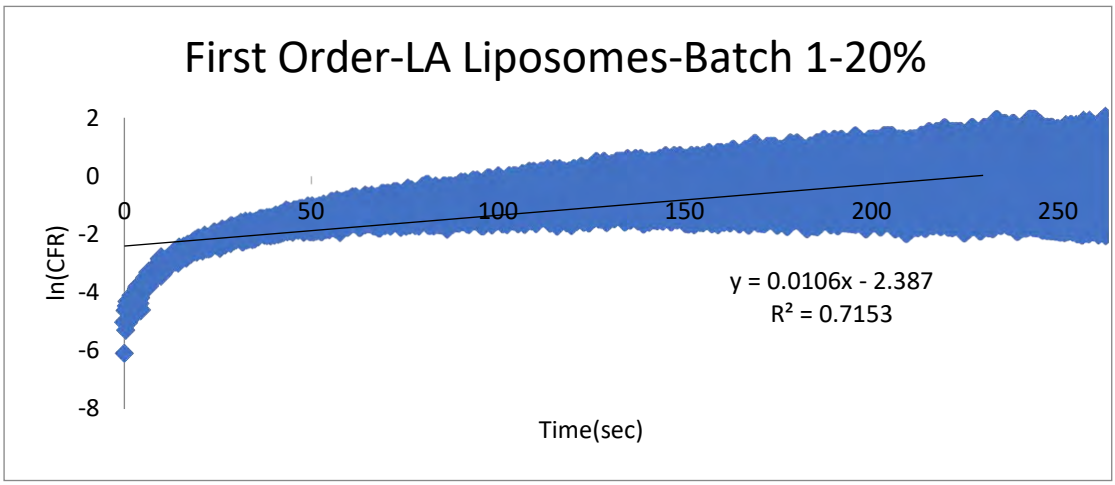

Figure 34 :First-Order model applied on LA liposomes for a power intensity of 7.46 mW/cm^2

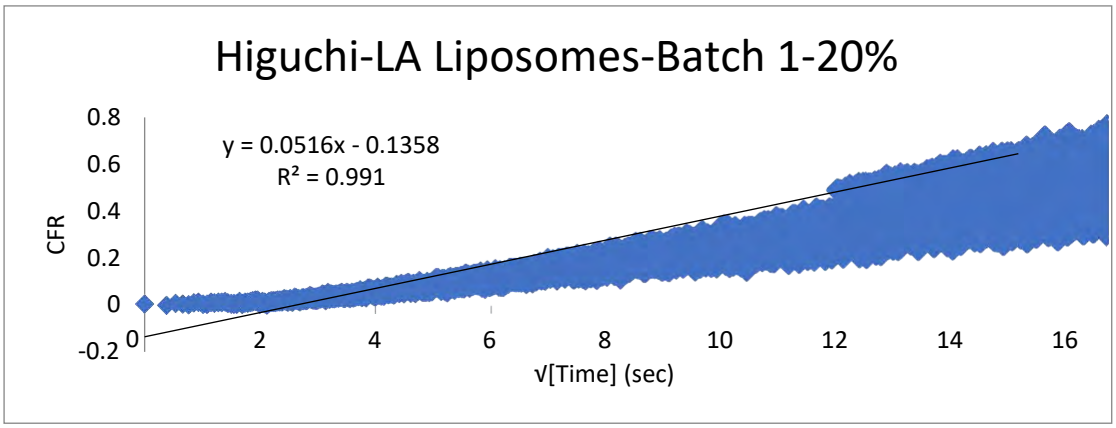

Figure 35:Higuchi model applied on LA liposomes for a power intensity of 7.46 mW/cm^2

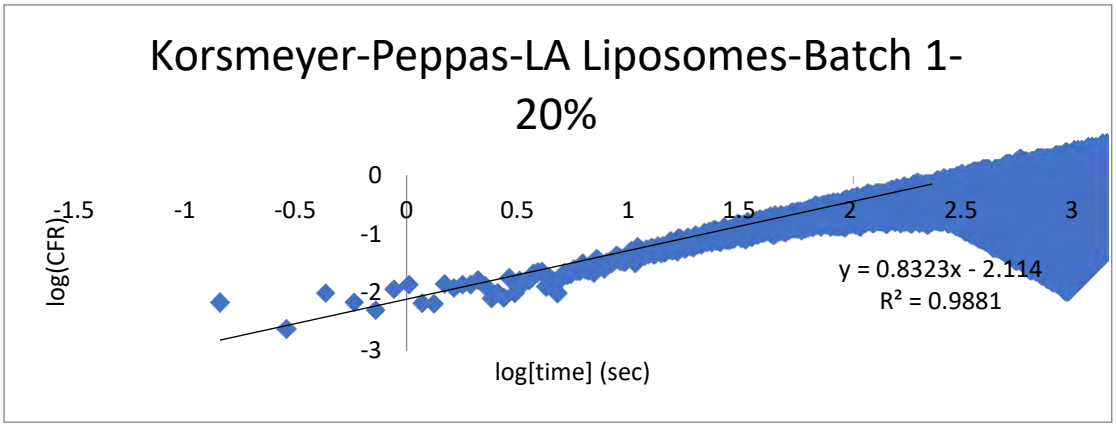

Figure 36:Korsmeyer-Peppas model applied on LA liposomes for a power intensity of 7.46 mW/cm^2

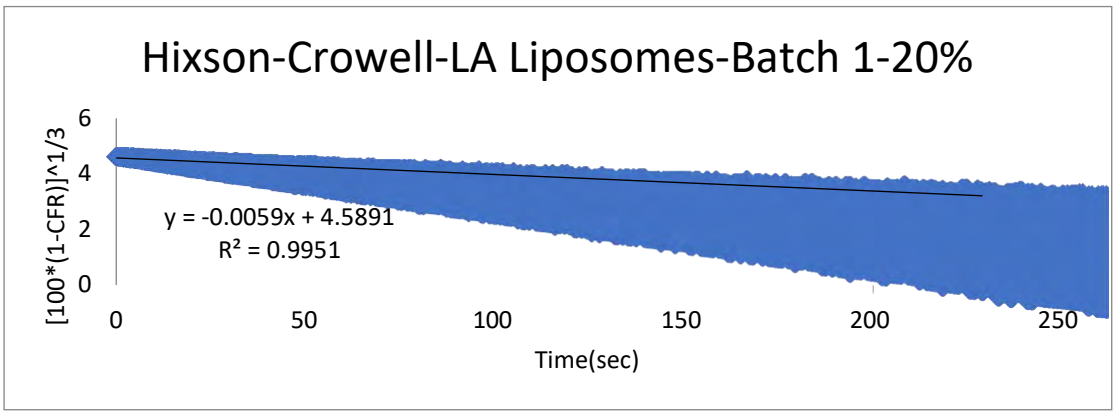

Figure 37:Hixon-Crowell model applied on LA liposomes for a power intensity of 7.46 mW/cm^2

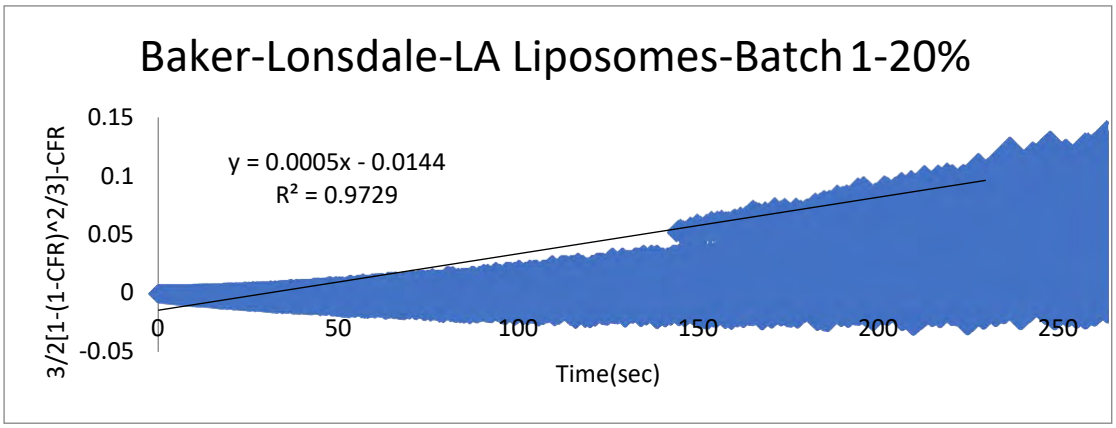

Figure 38:Baker-Lonsdale model applied on LA liposomes for a power intensity of 7.46 mW/cm^2

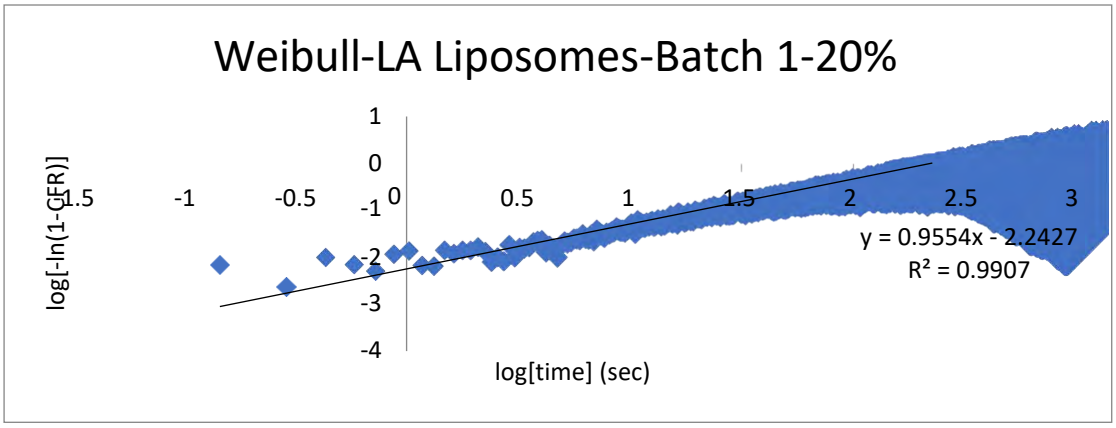

Figure 39: Weibull model applied on LA liposomes for a power intensity of 7.46 mW/cm^2

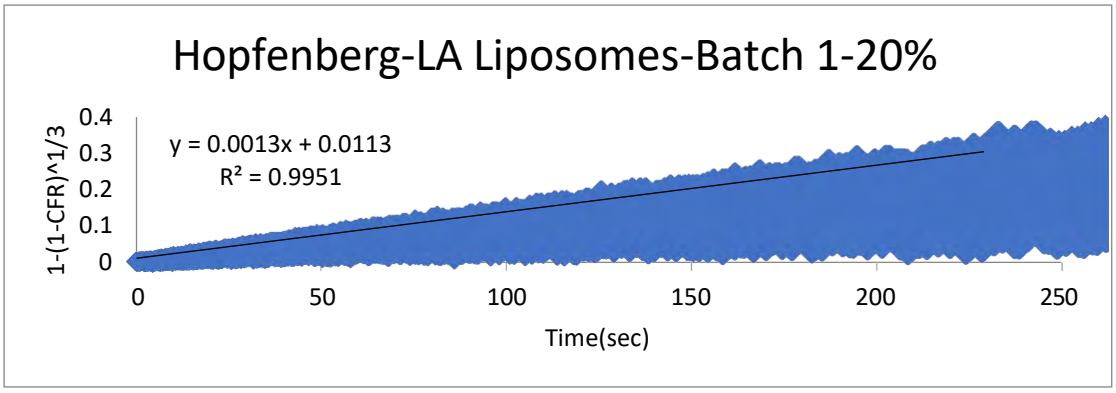

Figure 40: Hopfenberg model applied on LA liposomes for a power intensity of 7.46 mW/cm^2

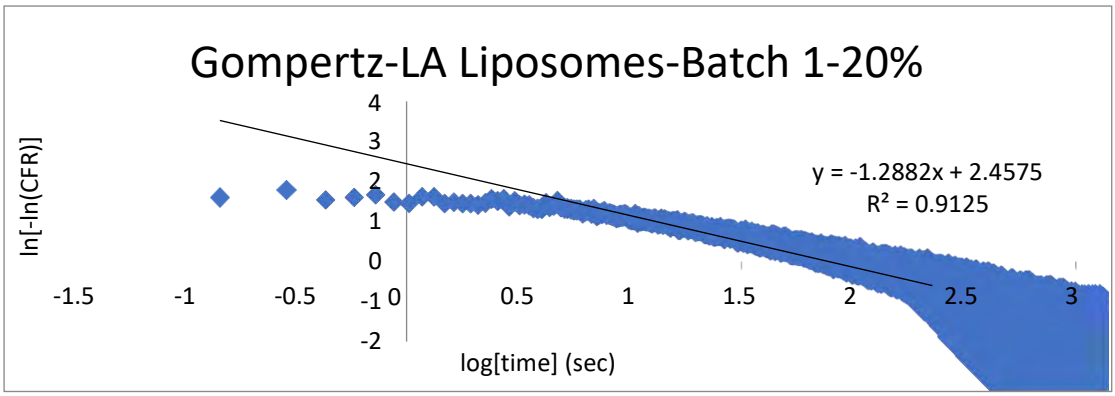

Figure 41: Gompertz model applied on LA liposomes for a power intensity of 7.46 mW/cm^2

Table 12: R^2 value of all kinetic models for control liposomes

Control Liposomes					
% Intensity	**Model**	**Batch 1**	**Batch 2**	**Batch 3**	**Average R^2**
20	Zero Order	0.9976	0.971	0.9758	0.98146667
	First Order	0.7051	0.6833	0.7372	0.70853333
	Higuchi	0.9878	0.9895	0.9782	0.98516667
	Korsmeyer-Peppas	0.9862	0.9899	0.9893	0.98846667
	Hixon-Crowell	0.9967	0.9948	0.9911	0.9942
	Baker-Lonsdale	0.9668	0.9751	0.9594	0.9671
	Weibull	0.9889	0.997	0.9848	0.99023333
	Hopfenberg	0.9967	0.9948	0.9911	0.9942
	Gompertz	0.8816	0.9011	0.8633	0.882
25	Zero Order	0.8956	0.908	0.8905	0.89803333
	First Order	0.6113	0.6287	0.6434	0.6278
	Higuchi	0.9707	0.9764	0.9629	0.97
	Korsmeyer-Peppas	0.9699	0.9766	0.9746	0.9737
	Hixon-Crowell	0.9627	0.9711	0.9567	0.9635
	Baker-Lonsdale	0.9775	0.9845	0.9724	0.97813333
	Weibull	0.9928	0.9948	0.9864	0.99133333
	Hopfenberg	0.9627	0.9711	0.9567	0.9635
	Gompertz	0.8961	0.8981	0.8837	0.89263333
30	Zero Order	0.7776	0.802	0.7251	0.76823333
	First Order	0.5435	0.525	0.4885	0.519
	Higuchi	0.9065	0.924	0.867	0.89916667
	Korsmeyer-Peppas	0.9408	0.9349	0.912	0.92923333
	Hixon-Crowell	0.867	0.8994	0.8139	0.8601
	Baker-Lonsdale	0.8993	0.9401	0.8603	0.8999
	Weibull	0.9752	0.9803	0.956	0.9705
	Hopfenberg	0.867	0.8994	0.8139	0.8601
	Gompertz	0.9083	0.9268	0.9199	0.91833333

Table 13: R^2 value of all kinetic models for LA liposomes

LA Liposomes					
% Intensity	**Model**	**Batch 1**	**Batch 2**	**Batch 3**	**Average R^2**
20	Zero Order	0.9783	0.9832	0.9696	0.97703333
	First Order	0.7155	0.673	0.694	0.69416667
	Higuchi	0.9906	0.9888	0.9947	0.99136667
	Korsmeyer-Peppas	0.9881	0.9821	0.9894	0.98653333
	Hixon-Crowell	0.9951	0.9961	0.99	0.99373333
	Baker-Lonsdale	0.9729	0.9695	0.987	0.97646667
	Weibull	0.9907	0.9893	0.995	0.99166667
	Hopfenberg	0.9951	0.9961	0.99	0.99373333
	Gompertz	0.9125	0.9256	0.9311	0.92306667
25	Zero Order	0.916	0.9437	0.9424	0.93403333
	First Order	0.632	0.6752	0.6432	0.65013333
	Higuchi	0.9806	0.9891	0.9934	0.9877
	Korsmeyer-Peppas	0.9741	0.9843	0.9799	0.97943333
	Hixon-Crowell	0.9555	0.9786	0.9819	0.972
	Baker-Lonsdale	0.9851	0.9843	0.9911	0.98683333
	Weibull	0.9897	0.9926	0.9958	0.9927
	Hopfenberg	0.9545	0.9786	0.9819	0.97166667
	Gompertz	0.9407	0.9163	0.9265	0.92783333
30	Zero Order	0.8737	0.8849	0.9084	0.889
	First Order	0.4806	0.6126	0.5941	0.56243333
	Higuchi	0.9677	0.9718	0.9844	0.97463333
	Korsmeyer-Peppas	0.8563	0.9698	0.9629	0.92966667
	Hixon-Crowell	0.9378	0.9491	0.9692	0.95203333
	Baker-Lonsdale	0.9755	0.9803	0.992	0.9826
	Weibull	0.9927	0.9917	0.9928	0.9924
	Hopfenberg	0.9378	0.9491	0.9692	0.95203333
	Gompertz	0.9449	0.9279	0.9286	0.9338

The Weibull distribution, named after the Swedish mathematician Waloddi Weibull, is widely used in many applications such as engineering, weather forecasting, economics and many forms of analysis. Focusing on drug diffusion and the study of drug release, as Explained in section 4.7.7, the linearized form of Weibull model is log[-ln(1-CFR)] =b log t-log a, hence a plot of log[-ln(1-CFR)] versus log time will have a slope of b. Mathematical models do not precisely provide the drug kinetic properties but they do give an insight into the mechanism(s) involved in drug release.

From the value of b, the shape parameter, the curve is categorized as exponential for b=1 or parabolic for b < 1 or sigmoid when b > 1 [66].

In term of the release mechanism studies have related the Weibull model to Fickian diffusion through the value of the shape parameter b. A value of b less than 0.75 indicates a Fickian diffusion, whereas a value between 0.75 and 1 indicates a combination of Fickian diffusion and case II transport, b=1 follows a first order release and b>1 shows a complex release that initially increases with time but eventually curves downwards [67], [68].

Fickian diffusion refers to the form of transport following the first and second Fick's laws. Fick's first law states that the flow of particles in a unit area is dependent on the concentration gradient of the particles as seen in Equation 23; Fick's second law deals with the change of concentration with time, shown in Equation 24, where *J* is the particle flux, *D* is diffusion coefficient, *A* is area and *C* is concentration. Another derivative of diffusion is known as non-Fickian diffusion, which refers to the form of diffusion that does not obey Fick's laws and deals with mass change along with diffusion, specifically the swelling and shrinking of a particle when placed in a fluid. Several forms of non-Fickian diffusion are found such as case II diffusion, sigmoidal or anomalous diffusion and two-step or super case II diffusion. Case II diffusion is a focus in the study of drug delivery, since the structure of the drug carrier when inside the body can change according to the chemistry of the environment it is in such as pH or the hydrophobic/hydrophilic component of the polymer [69].

$$J = -DA\frac{=@}{=\{} \tag{23}$$

$$\frac{é@(\{,,)}{é,} = D^{e}\frac{é^{g}@(\{,,)}{é\{^{g}} \tag{24}$$

By analyzing the information found in Table 14, in the case of control liposomes, the average b value was found to be 1.0 and 0.91 for LA liposomes. From the mentioned b-values it can be inferred that controlled liposomes follow a 1st order rate of release which follows Fick's first law of diffusion, whereas LA liposomes have a combined release mechanism of Fickian diffusion and case II transport. The first order release is sustained release that depends on the concentration of the drug, which explains the behavior of control liposomes release profile discussed in section 5.4, where the % release seemed to increase with the first 3 pulses and was significantly greater when compared to LA liposomes. On the other hand, the combined release

mechanism in LA liposomes have case II transport which is more of that of a controlled release that depends on the surrounding environment the liposome is in. Therefore, LA liposomes were shown to have less % release which may be due to swelling or shrinking of the liposomes.

Table 14: Value of b (Weibull shape parameter) at different power intensities

Liposome type	**Batch #**	**Power Intensity(mW/cm^2)**		
		7.46	**9.85**	**17.31**
Control	1	1.0428	1.0512	0.9645
	2	1.0507	1.0487	1.0141
	3	1.0738	1.0671	1.0115
Average ± STD		1.05±0.01	1.06±0.01	1.00±0.02
LA	1	0.9554	0.9002	0.8239
	2	1.0135	0.9511	0.8913
	3	0.8837	0.8977	0.8948
Average ± STD		0.95±0.05	0.92±0.02	0.87±0.03

A Two-Factor ANOVA test with replication was performed and results are presented in Table 15, it was found that the value of b is significantly different between control and LA liposomes (p-value=1.03E-05 and $F>F_{critical}$), and between each power intensity (p-value=0.015064 and $F>F_{critical}$) showing that the type of drug diffusion out of liposomes is dependent on both the liposomes type and the intensity of US it is subjected to. On the other hand, there was found to be no interaction between power intensity and type of liposome (p-value=0.713709 and $F<F_{critical}$). Inferring that the presence of the moiety retards the release of the calcein from the nanopores in the liposomes.

Table 15: Two Factor ANOVA test on b value

ANOVA						
Source of Variation	***SS***	***df***	***MS***	***F***	***P-value***	***F crit***
Sample	0.068796	1	0.068796	52.44297	1.03E-05	4.747225
Columns	0.015934	2	0.007967	6.07341	0.015064	3.885294
Interaction	0.00091	2	0.000455	0.346941	0.713709	3.885294
Within	0.015742	12	0.001312			
Total	0.101382	17				

Chapter 6. Conclusion and Future Work

With focused and dedicated research, humanity is getting one step closer to winning the fight against cancer. An efficient, harmless and innovative Drug Delivery System (DDS) is the key player in this fight. Liposomes, a form of nanocarriers that can encapsulate chemotherapeutics in their core and be decorated with a targeting moiety was used in this research. Receptor-mediated endocytosis will guide the modified liposomes towards the tumor site, and upon accumulation, US will trigger drug release at the tumor site. This research focuses on Human Hepatocellular Carcinoma (HCC), specifically the overexpressed ASGPR found in its cell line, making it the first study to combine liposomes, disaccharides, and US.

In this research, the process of preparing final liposomes and studying release mechanisms is precisely structured in order for each test to accurately represent and complement the following test. At first, the attachment between DSPE-PEG-NH_2 and Lactobionic acid is confirmed for accuracy using the phenol-sulfuric acid test and IR spectroscopy and performed on three different batches. Next, both control and targeted liposomes are prepared using the thin lipid hydration method where their final size is measured for three batches of each as well through DLS. Stewart assay follows in order to measure the amount of lipid found in both liposomes, also while ensuring reproducibility of results. Finally, low-frequency ultrasound is used in conjugation with calcein intensity in order to study the release mechanisms at different power intensities which were further studied using kinetic release modeling to obtain the best-fit release data.

As with all research projects, there is no end to product development and process optimization. The future work entails studying the effect of high-frequency US on the release of this drug delivery system. Furthermore, in order to bring the research one step closer to reality *in vitro* and *in vivo* tests must be conducted to study the behavior of LA liposomes in cells and animals.

This research has a much higher purpose than just scientific breakthroughs, cancer has in one way or another left its harmful print on every person. Having lost a loved one to cancer and seen her undergo the process of chemotherapy which in some instances has side effects as devastating side as cancer itself; I believe cancer patients suffer enough from the disease without adding the worry of hair loss, nausea, and

weakness. Therefore, through this research, the hope is to improve the quality of life for cancer patients in the UAE and worldwide.

References

[1] R. Siegel. "Cancer treatment and survivorship statistics, 2012" (in eng). *CA: A Cancer Journal for Clinicians,* vol. 62, no. 4, p. 41-220, 2012.

[2] G. H. Lyman. "Economics of cancer care". *Journal of Oncology Practice,* vol. 3, no. 3, pp. 113-114, 2007.

[3] R. H. Bradbury and P. Angibaud. *Cancer Topics in Medicinal Chemistry*. Berlin: Springer (in English), v.1, 2007, pp. 1862-2461.

[4] J. Panno. *Cancer: The Role of Genes, Lifestyle, and Environment*.New York: Facts on File, 2005, pp. 62-65.

[5] C. M. Haskell and J. S. Berek. *Cancer treatment*. Philadelphia : Saunders, 1980.

[6] H. Attarwala. "Role of antibodies in cancer targeting". *Journal of Natural Science, Biology, and Medicine,* vol. 1, no. 1, pp. 53-56, Jul-Dec 2010.

[7] C. Buzea, I. I. Pacheco, and K. Robbie. "Nanomaterials and nanoparticles: Sources and toxicity". *Biointerphases*, vol. 2, no. 4, pp. MR17-MR71, December 01 2007.

[8] D. R. Boverhof *et al.*. "Comparative assessment of nanomaterial definitions and safety evaluation considerations". *Regulatory Toxicology and Pharmacology,* vol. 73, no. 1, pp. 137-150, 2015.

[9] W.-Y. Qian, D.-M. Sun, R.-R. Zhu, X.-L. Du, H. Liu, and S.-L. Wang. "pH-sensitive strontium carbonate nanoparticles as new anticancer vehicles for controlled etoposide release". *International Journal of Nanomedicine,* vol. 7, pp. 5781-5792, 2012.

[10] B. J. Valverde. *Liver Cancer : Causes, Diagnosis, and Treatment (Cancer Etiology, Diagnosis, and Treatments).* Hauppauge, N.Y. : Nova Science Publishers (in English), 2011, pp. 1-3.

[11] A. A. D'Souza and P. V. Devarajan. "Asialoglycoprotein receptor mediated hepatocyte targeting - strategies and applications". *Journal of Controlled Release : Official Journal of the Controlled Release Society,* vol. 203, pp. 39-126, 2015.

[12] G. T. Noble, J. F. Stefanick, J. D. Ashley, T. Kiziltepe, and B. Bilgicer. "Ligand-targeted liposome design: challenges and fundamental considerations," *Trends in Biotechnology,* vol. 32, no. 1, pp. 32-45, 2014.

[13] K. Jain, U. Kesharwani, K. Gupta and N. K. Jain. "Dendrimer toxicity: Let's meet the challenge". *International Journal of Phramceuticals,* vol. 394, pp. 42-122, 2010.

[14] L. P. Mendes, P. Jiayi, and V. P. Torchilin. "Dendrimers as Nanocarriers for Nucleic Acid and Drug Delivery in Cancer Therapy". *Molecules,* vol. 22, no. 9, pp. 1401, 2017.

[15] G. Guney and H. Kutlu. "Importance of Solid Lipid Nanoparticles in Cancer Therapy". *NSTI-Nanotech,* vol. 3, pp. 400-403, 2011.

[16] H. Khodabandehloo, H. Zahednasab, and A. Ashrafi Hafez. "Nanocarriers Usage for Drug Delivery in Cancer Therapy". *Iranian Journal of Cancer Prevention,* vol. 9, no. 2, p. e3966, 2016.

[17] M. A. Elkhodiry *et al.*. "Synergistic Nanomedicine: Passive, Active, and Ultrasound-Triggered Drug Delivery in Cancer Treatment". *Journal of Nanoscience and Nanotechnology,* vol. 16, no. 1, pp. 1-18, 2016.

[18] G. A. Husseini and W. G. Pitt. "Micelles and nanoparticles for ultrasonic drug and gene delivery". *Advanced Drug Delivery Review,* vol. 60, no. 10, p. 1137, 2008.

[19] A. Akbarzadeh *et al.*. "Liposome: classification, preparation, and applications". *Nanoscale Research Letters,* vol. 8, no. 1, pp. 102-102, 2013.

[20] S. E. Ahmed, A. M. Martins, and G. A. Husseini. "The use of ultrasound to release chemotherapeutic drugs from micelles and liposomes". *Journal of Drug Targeting,* vol. 23, no. 1, pp. 16-42, 2015.

[21] W. G. Pitt, G. A. Husseini, and B. J. Staples. "Ultrasonic drug delivery - a general review". *Expert Opinion on Drug Delivery*, vol. 1, pp. 37-56, 2004.

[22] S. Abbina and A. Parambath. "PEGylation and its alternatives: A summary" in *Engineering of Biomaterials for Drug Delivery Systems* ,1st ed, vol. 1. A. Parambath ,Ed. Amsterdam: Elsevier Scince, 2018, pp. 363-376.

[23] M. L. Immordino, F. Dosio, and L. Cattel. "Stealth liposomes: review of the basic science, rationale, and clinical applications, existing and potential". *International Journal of Nanomedicine,* vol. 1, no. 3, pp. 297-315, 2006.

[24] M. Salim, H. Minamikawa, A. Sugimura, and R. Hashim."Amphiphilic designer nano-carriers for controlled release". *MedChemComms,* vol. 5, pp. 1602-1618, 2014.

[25] A. K. Iyer, G. Khaled, J. Fang, and H. Maeda. "Exploiting the enhanced permeability and retention effect for tumor targeting". *Drug Discovery Today,* vol. 11, no. 17, pp. 812-818, 2006.

[26] H. Zhong *et al.*. "Overexpression of hypoxia-inducible factor 1α in common human cancers and their metastases" .*Cancer Research*, vol. 59, no. 22, pp. 5830-5835, 1999.

[27] D. Katayoun and A. Abbas Hemmati. "Active-targeted Nanotherapy as Smart Cancer Treatment" in *Smart Drug Delivery System,*1st ed., vol. 3.A. Sezer, Ed. London : Intech Open, 2016, pp.91-116.

[28] J. Sudimack and R. J. Lee. "Targeted drug delivery via the folate receptor". *Advanced Drug Delivery Reviews,* vol. 41, no. 2, pp. 62-147, 2000.

[29] P. Kumar and R. Srivastava. *Nanomedicine for cancer therapy : from chemotherapeutic to hyperthermia-based therapy*. Switzerland: Springer International Publishing, 2016, pp.19-20.

[30] D. A. Richards, A. Maruani, and V. Chudasama. "Antibody fragments as nanoparticle targeting ligands: a step in the right direction." *Chemical Science,* vol. 8, no. 1, pp. 63-77, 2017.

[31] Y. H. Bae, R. J. Mrsny, and K. Park. *Cancer Targeted Drug Delivery : An Elusive Dream*. New York: Springer International Publishing, 2013, pp.461-507.

[32] G. Yosi, F. Michael, and G. Gary. "Recent Innovations in Peptide Based Targeted Drug Delivery to Cancer Cells." *Biomedicines,* vol. 4, p. 11, 2016.

[33] R. Javad, M. Ahad, A. Abbas, T. Maryam, H. Maryam, and R. Mohammad. "Anti-Cancer Drug Delivery Using Carbohydrate-Based Polymers." *Current Pharmaceutical Design: CPD,* vol. 23, pp. 6019-6032, 2017.

[34] X. Zhou *et al.*. "Lactosylated liposomes for targeted delivery of doxorubicin to hepatocellular carcinoma." *International Journal of Nanomedicine,* vol. 7, pp. 5465-5474, 2012.

[35] L. M. Bareford and P. W. Swaan. "Endocytic Mechanisms for Targeted Drug Delivery." *Advanced Drug Delivery Reviews,* vol. 59, no. 8, pp. 748-758, 2007.

[36] M. Huo, Y. Chen, and J. Shi. "Triggered-release drug delivery nanosystems for cancer therapy by intravenous injection: where are we now?" *Expert Opinion on Drug Delivery,* vol. 13, no. 9, pp. 1195-1198, 2016.
[37] R. A. Gatenby and R. J. Gillies. "Why do cancers have high aerobic glycolysis?" *Nature Reviews Cancer,* vol. 4, p. 891, 2004.
[38] H. G. Moussa, A. M. Martins, and G. A. Husseini. "Review on triggered liposomal drug delivery with a focus on ultrasound." *Current Cancer Drug Targets,* vol. 15, no. 4, pp. 282-313, 2015.
[39] T. L. Andresen, D. H. Thompson, and T. Kaasgaard. "Enzyme-triggered nanomedicine: Drug release strategies in cancer therapy (Invited Review)." *Molecular Membrane Biology,* vol. 27, pp. 353-363, 2010.
[40] S. Kaur, C. Prasad, B. Balakrishnan, and R. Banerjee. "Trigger responsive polymeric nanocarriers for cancer therapy." *Biomaterials Science,* vol. 3, no. 7, pp. 87-955, 2015.
[41] M. Karimi *et al.*. "Temperature-Responsive Smart Nanocarriers for Delivery Of Therapeutic Agents: Applications and Recent Advances." *ACS Applied Materials & Interfaces,* vol. 8, no. 33, pp. 21107-21133, 2016.
[42] K. Hayashi *et al.*. "Magnetically responsive smart nanoparticles for cancer treatment with a combination of magnetic hyperthermia and remote-control drug release." *Theranostics,* vol. 4, no. 8, pp. 44-834, 2014.
[43] F. M. Abu-Zidan, A. F. Hefny, and P. Corr. "Clinical ultrasound physics." *Journal of Emergencies, Trauma and Shock,* vol. 4, no. 4, p. 501, 2011.
[44] T. G. Leighton. "What is ultrasound?" *Progress in Biophysics and Molecular Biology,* vol. 93, no. 1, pp. 3-83, 2007.
[45] S. Mullick Chowdhury, T. Lee, and J. K. Willmann. "Ultrasound-guided drug delivery in cancer." *Ultrasonography,* vol. 36, no. 3, pp. 171-184, 2017.
[46] C. E. Brennen. "Cavitation in medicine." *Interface Focus,* vol. 5, no. 5, pp. 20150022, 2015.
[47] A. M. Martins, S. A. Elgaili, R. F. Vitor, and G. A. Husseini. "Ultrasonic Drug Delivery Using Micelles and Liposomes." in *Handbook of Ultrasonics and Sonochemistry*,1st ed. , vol. 1. M.Ashokkumar,Ed. Singapore: Springer Science, 2015, pp. 1-35.
[48] A. Schroeder *et al.*. "Controlling liposomal drug release with low frequency ultrasound: mechanism and feasibility." *Langmuir : the ACS Journal of Surfaces and Colloids,* vol. 23, no. 7, pp. 25-4019, 2007.
[49] M. Afadzi *et al.*. "Mechanisms of the ultrasound-mediated intracellular delivery of liposomes and dextrans." *IEEE Transactions on Ultrasonics, Ferroelectrics and Frequency Control,* vol. 60, no. 1, pp. 21-33, 2013.
[50] G. Myhr and J. Moan. "Synergistic and tumour selective effects of chemotherapy and ultrasound treatment." *Cancer Letters,* vol. 232, no. 2, pp. 206-213, 2006.
[51] W. G. Pitt *et al.*. "Preliminary results of combining low frequency low intensity ultrasound and liposomal drug delivery to treat tumors in rats." *Journal of Nanoscience and Nanotechnology,* vol. 11, no. 3, pp. 1866-1870, 2011.
[52] H. Patel, C. Tscheka, and H. Heerklotz. "Characterizing Vesicle Leakage By Fluorescence Lifetime Measurements." *Biophysical Journal,* vol. 98, no. 3, pp. 80a, 2010.

[53] L.-F. Gutiérrez, S. Hamoudi, and K. Belkacemi. "Lactobionic acid: A high value-added lactose derivative for food and pharmaceutical applications." *International Dairy Journal,* vol. 26, no. 2, pp. 103-111, 2012.

[54] S. K. Vashist. "Comparison of 1-Ethyl-3-(3-Dimethylaminopropyl) Carbodiimide Based Strategies to Crosslink Antibodies on Amine-Functionalized Platforms for Immunodiagnostic Applications." *Diagnostics,* vol. 2, no. 3, pp. 2075-4418, 2012.

[55] M. Viel, F. Collet, and C. Lanos. "Chemical and multi-physical characterization of agro-resources' by-product as a possible raw building material." *Industrial Crops & Products,* vol. 120, pp. 214-237, 2018.

[56] S. S. Nielsen. "Food Analysis Laboratory Manual" in *Food science text series,* 5th ed.. S. Nielsen, Ed. Switzerland: Springer (in English), 2017, pp. 47-53.

[57] B. Stuart. *Infrared Spectroscopy : Fundamentals and Application*s *(Analytical Techniques in the Sciences).* Chichester: Eng. J. Wiley (in English), 2004, pp.1-14.

[58] M. Manzoli. "Boosting the Characterization of Heterogeneous Catalysts for H2O2 Direct Synthesis by Infrared Spectroscopy." *Catalysts,* vol. 9, no. 1, pp. 2073- 4344, 2019.

[59] S. Bhattacharjee. "DLS and zeta potential – What they are and what they are not?" *Journal of Controlled Release,* vol. 235, pp. 337-351, 2016.

[60] J. C. M. Stewart. "Colorimetric determination of phospholipids with ammonium ferrothiocyanate." *Analytical Biochemistry,* vol. 104, no. 1, pp. 10-14, 1980.

[61] Z. Ya, H. Zhimin, E. Omari-Siaw, L. Shuang, and Z. Yuan. "Preparation and In Vitro-In Vivo Evaluation of Sustained-Release Matrix Pellets of Capsaicin to Enhance the Oral Bioavailability." *AAPS PharmSciTech,* vol. 17, pp. 339-349, 2016.

[62] S. Dash, P. N. Murthy, P. Chowdhury, and L. Nath. "Kinetic modeling on drug release from controlled drug delivery systems." *Acta Poloniae Pharmaceutica - Drug Research,* vol. 67, no. 3, pp. 217-223, 2010.

[63] Y. Zeng *et al.*. "Lipid-AuNPs@PDA nanohybrid for MRI/CT imaging and photothermal therapy of hepatocellular carcinoma." *ACS Applied Materials & Interfaces,* vol. 6, no. 16, pp. 77-14266, 2014.

[64] D. Bansal, K. Yadav, V. Pandey, A. Ganeshpurkar, A. Agnihotri, and N. Dubey. "Lactobionic acid coupled liposomes: an innovative strategy for targeting hepatocellular carcinoma." *Drug Delivery,* vol. 23, no. 1, pp. 6-140, 2016.

[65] E. Wiercigroch *et al.*. "Raman and infrared spectroscopy of carbohydrates: A review." *Spectrochimica Acta Part A: Molecular and Biomolecular Spectroscopy,* vol. 185, pp. 317-335, 2017.

[66] N. Patel, N. Chotai, J. Patel, T. Soni, J. Desai, and R. Patel. "Comparison of In Vitro Dissolution Profiles of Oxcarbazepine-HP b-CD Tablet Formulations with Marketed Oxcarbazepine Tablets." *Dissolution Technologies,* vol. 15, no. 4, pp. 28-34, 2008.

[67] V. Papadopoulou, K. Kosmidis, M. Vlachou, and P. Macheras. "On the use of the Weibull function for the discernment of drug release mechanisms." *International Journal of Pharmaceutics,* vol. 309, no. 1, pp. 44-50, 2006.

[68] S. Kaddah, N. Khreich, F. Kaddah, C. Charcosset, and H. Greige-Gerges. "Cholesterol modulates the liposome membrane fluidity and permeability for a hydrophilic molecule." *Food and Chemical Toxicology,* vol. 113, pp. 40-48, 2018.

[69] K. W. Kolasinski, *Physical Chemistry : How Chemistry Works*. Newark: Wiley (in English), 2017, pp. 55-56.

Appendix A: Plots of kinetic modeling for Control Liposomes Batch 1

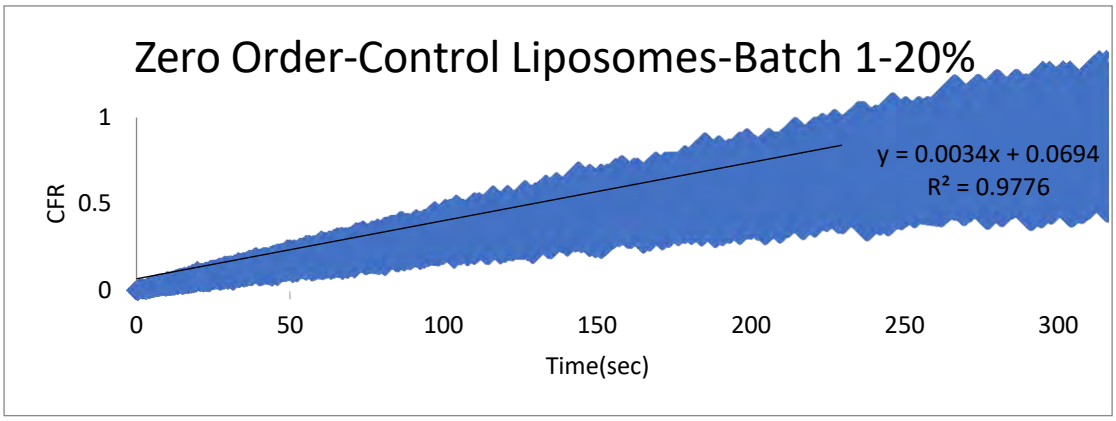

Figure 42: Zero Order model applied on Control liposomes for a power intensity of 7.46 mW/cm^2

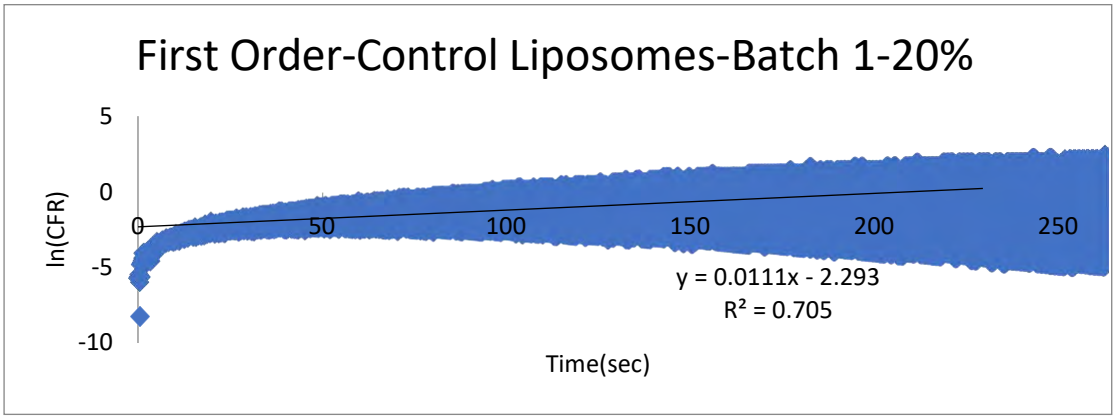

Figure 43:First Order model applied on Control liposomes for a power intensity of 7.46 mW/cm^2

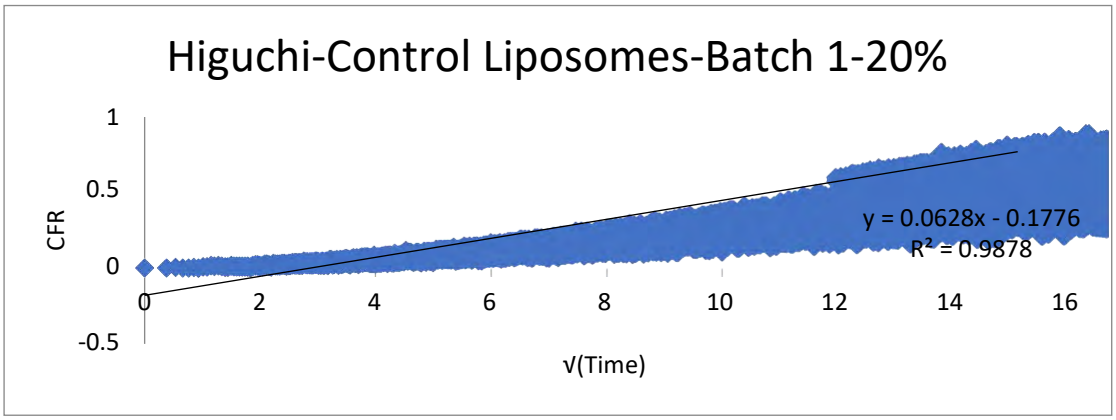

Figure 44:Higuchi model applied on Control liposomes for a power intensity of 7.46 mW/cm^2

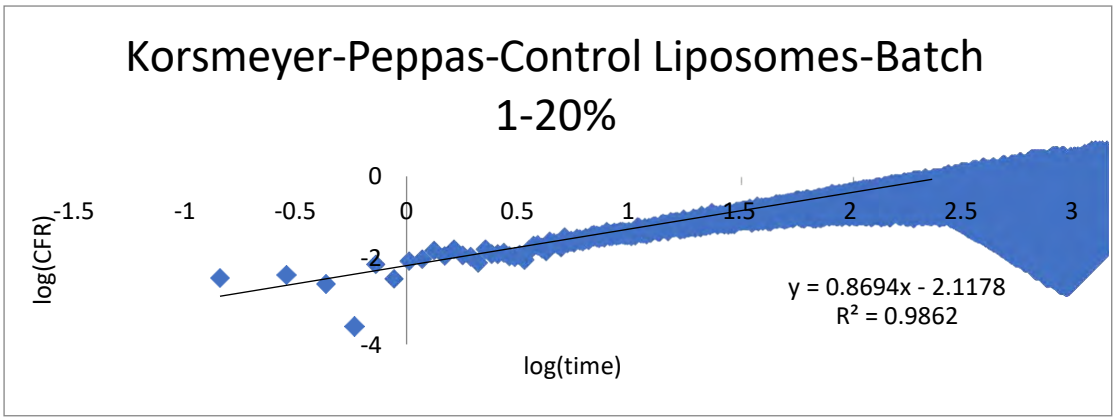

Figure 45:Korsmeyer-Peppas model applied on Control liposomes for a power intensity of 7.46 mW/cm^2

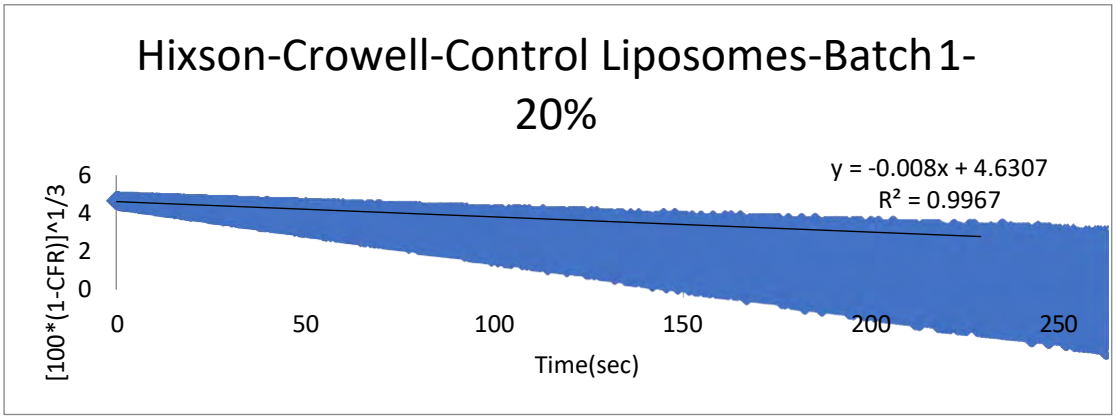

Figure 46:Hixson-Crowell model applied on Control liposomes for a power intensity of 7.46 mW/cm^2

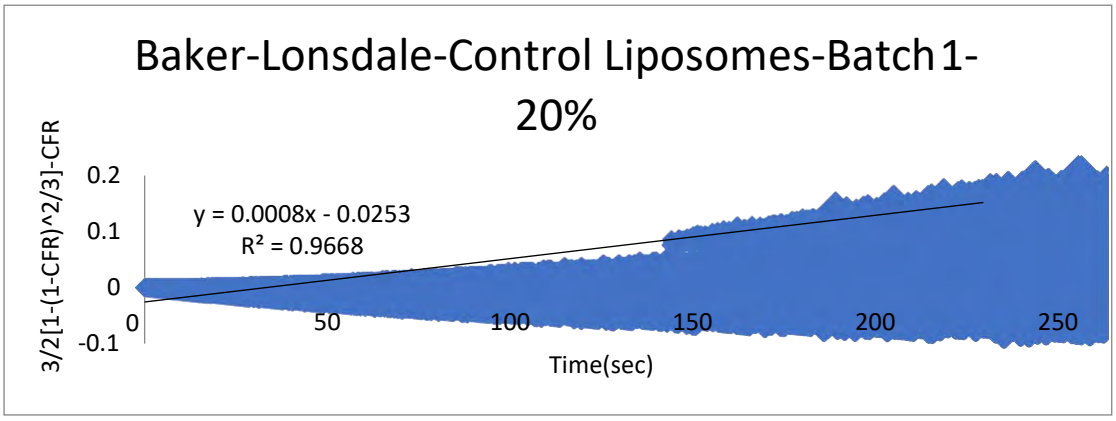

Figure 47:Baker-Lonsdale model applied on Control liposomes for a power intensity of 7.46 mW/cm^2

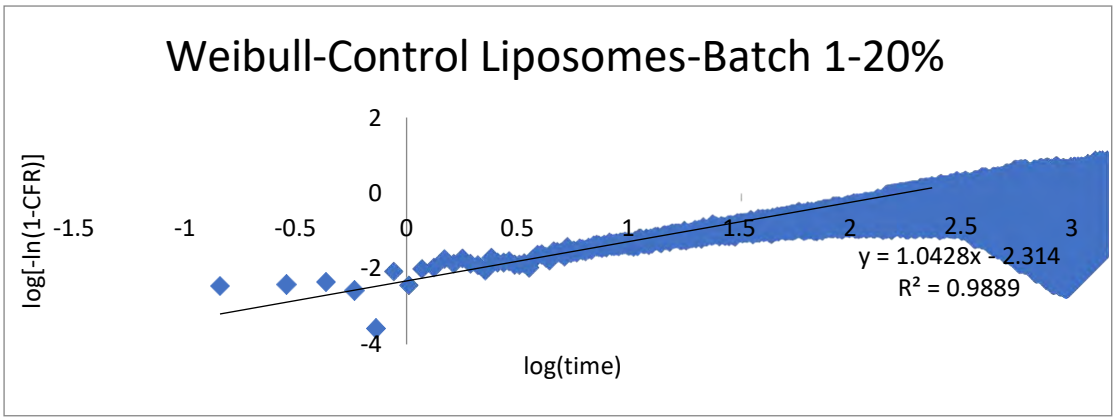

Figure 48:Weibull model applied on Control liposomes for a power intensity of 7.46 mW/cm^2

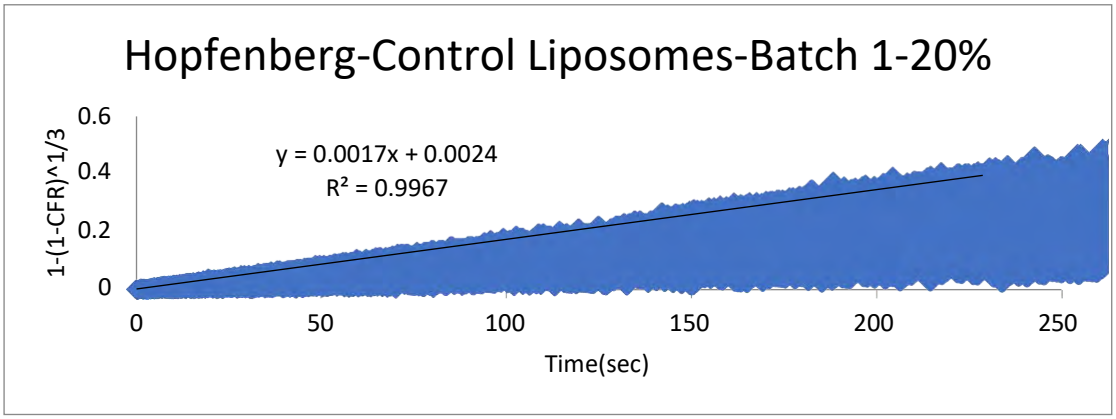

Figure 49:Hopfenberg model applied on Control liposomes for a power intensity of 7.46 mW/cm^2

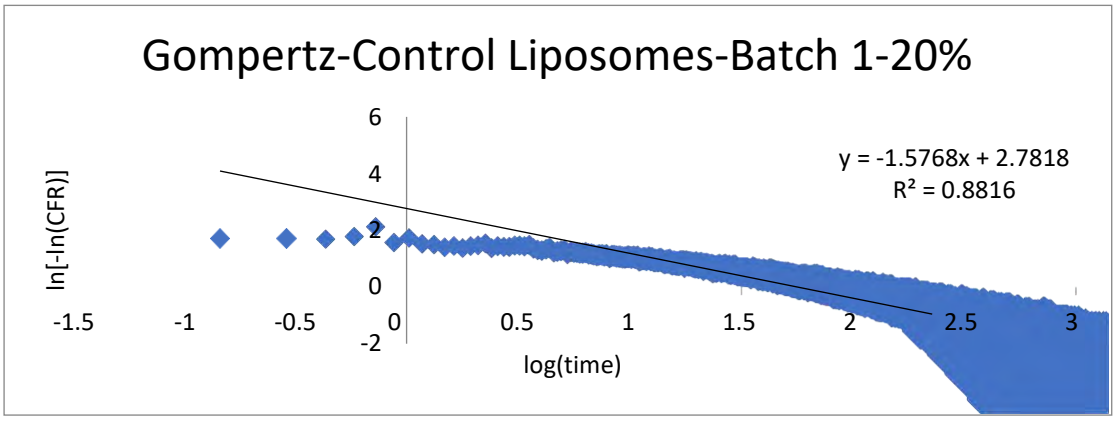

Figure 50:Gompertz model applied on Control liposomes for a power intensity of 7.46 mW/cm^2

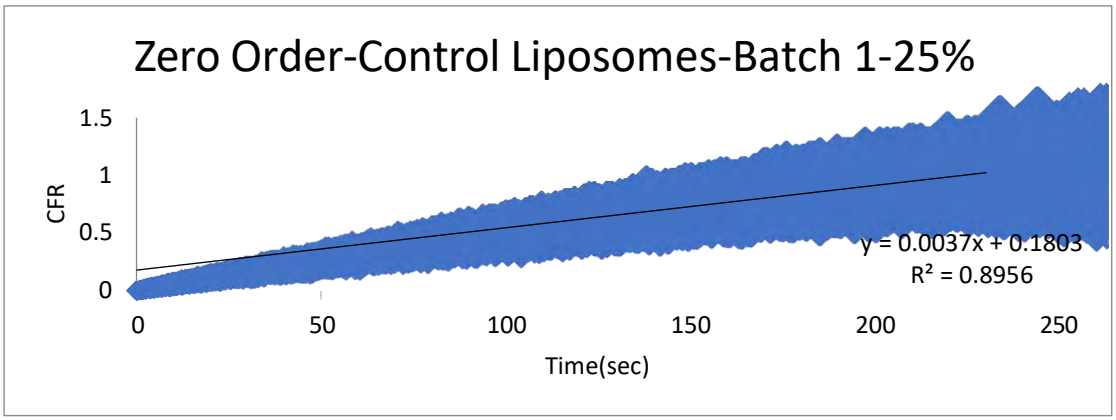

Figure 51:Zero Order model applied on Control liposomes for a power intensity of 9.85 mW/cm^2

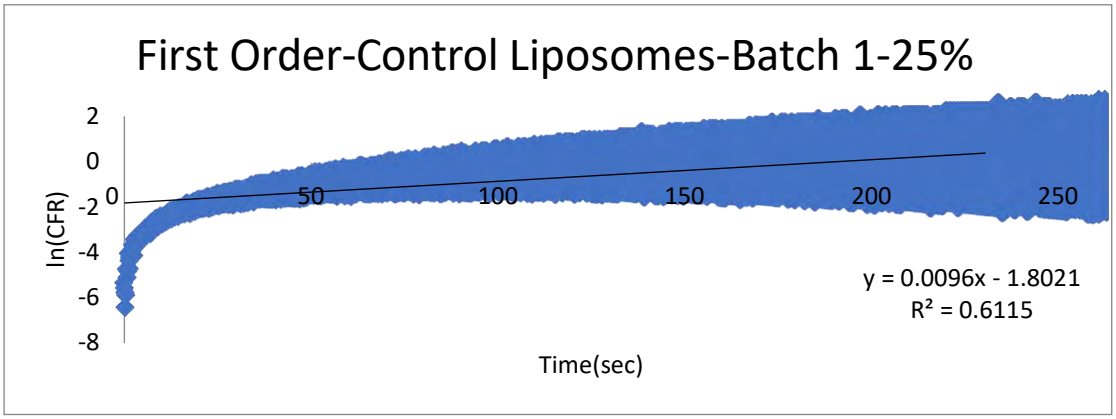

Figure 52: First Order model applied on Control liposomes for a power intensity of 9.85 mW/cm^2

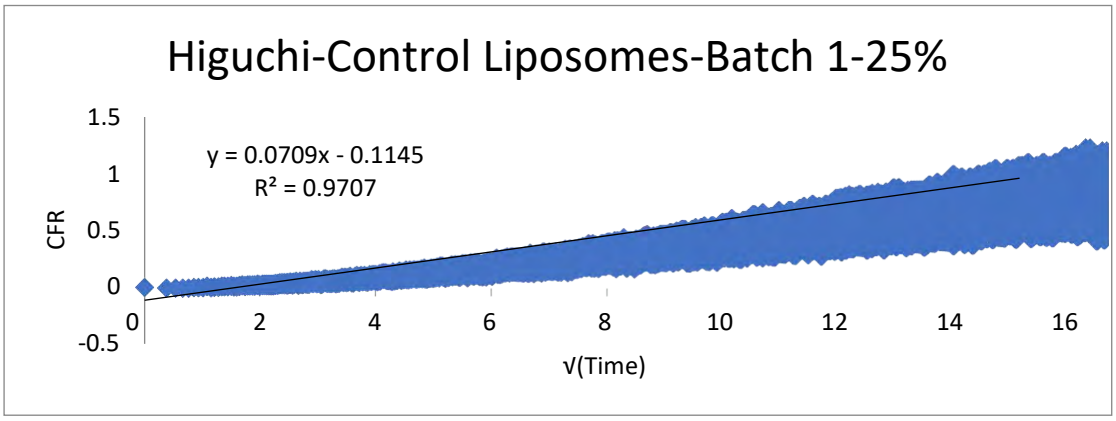

Figure 53:Higuchi model applied on Control liposomes for a power intensity of 9.85 mW/cm^2

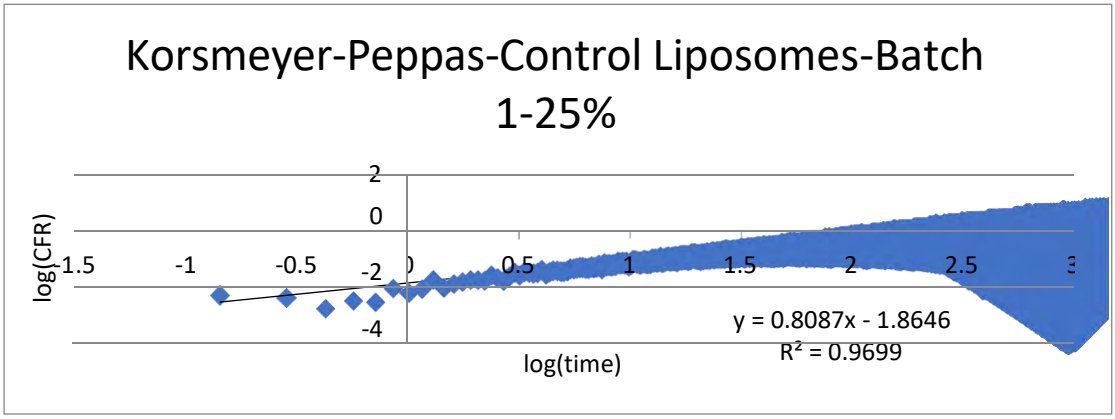

Figure 54: Korsmeyer-Peppas model applied on Control liposomes for a power intensity of 9.85 mW/cm^2

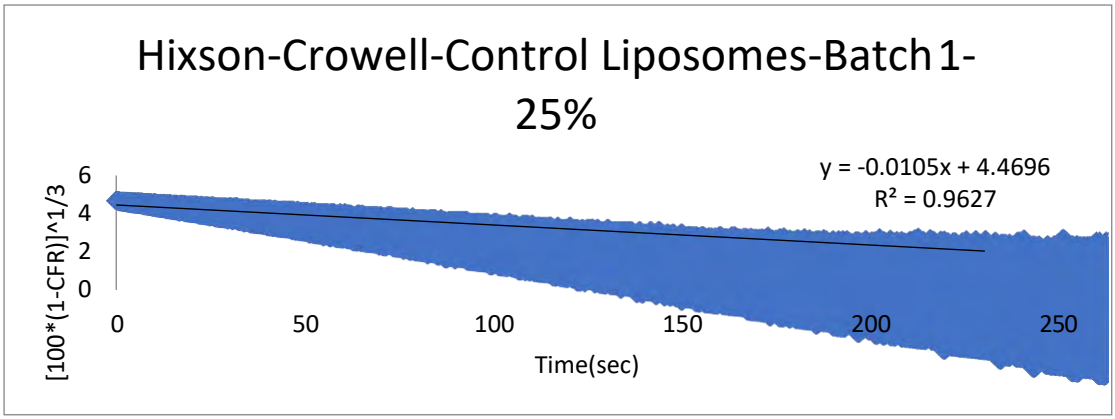

Figure 55: Hixson-Crowell model applied on Control liposomes for a power intensity of 9.85 mW/cm^2

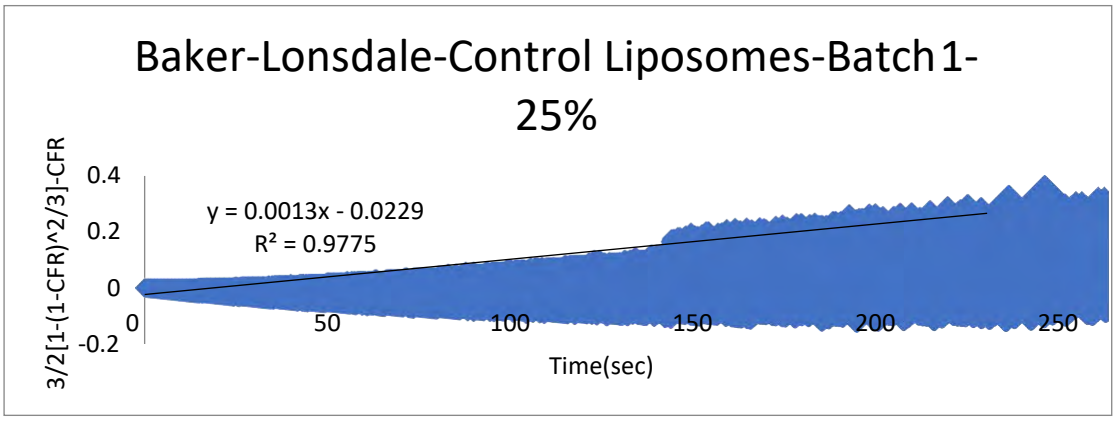

Figure 56:Baker-Lonsdale model applied on Control liposomes for a power intensity of 9.85 mW/cm^2

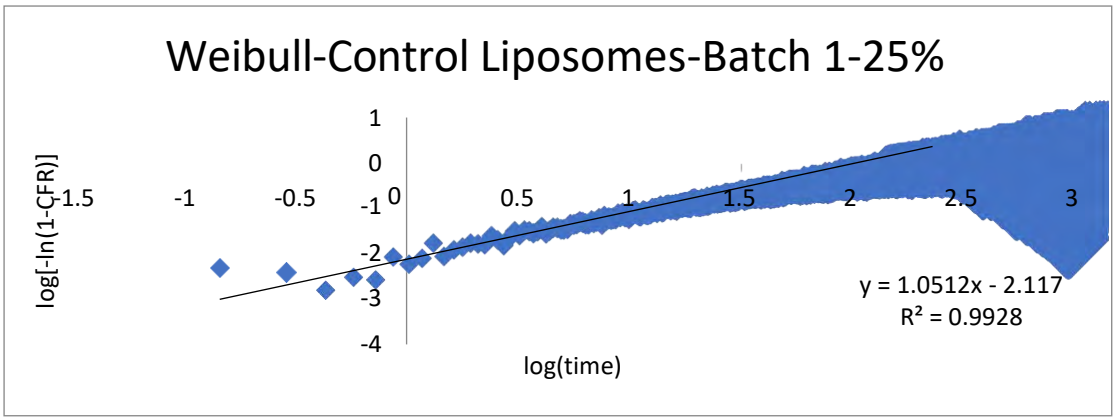

Figure 57: Weibull model applied on Control liposomes for a power intensity of 9.85 mW/cm^2

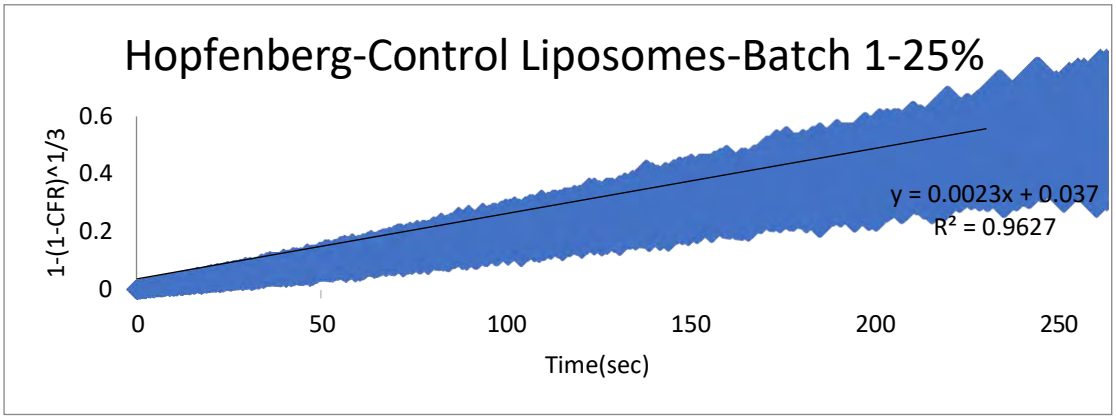

Figure 58: Hopfenberg model applied on Control liposomes for a power intensity of 9.85 mW/cm^2

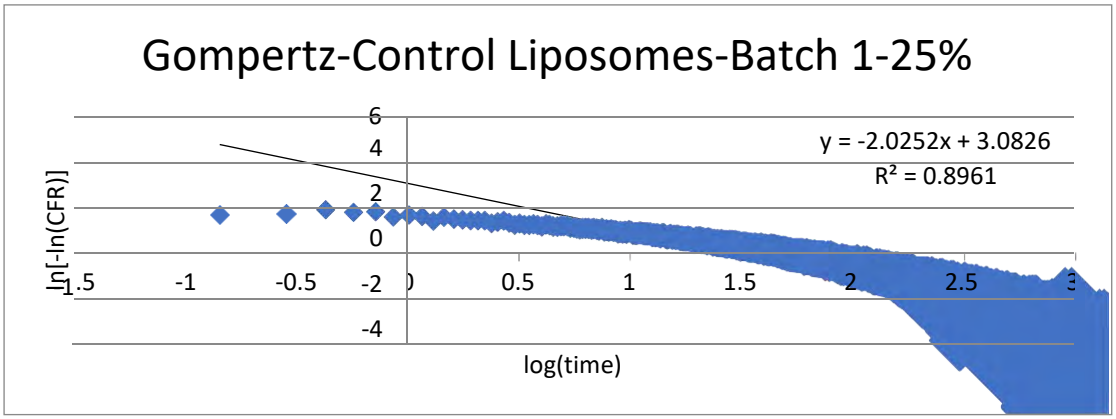

Figure 59: Gompertz model applied on Control liposomes for a power intensity of 9.85 mW/cm^2

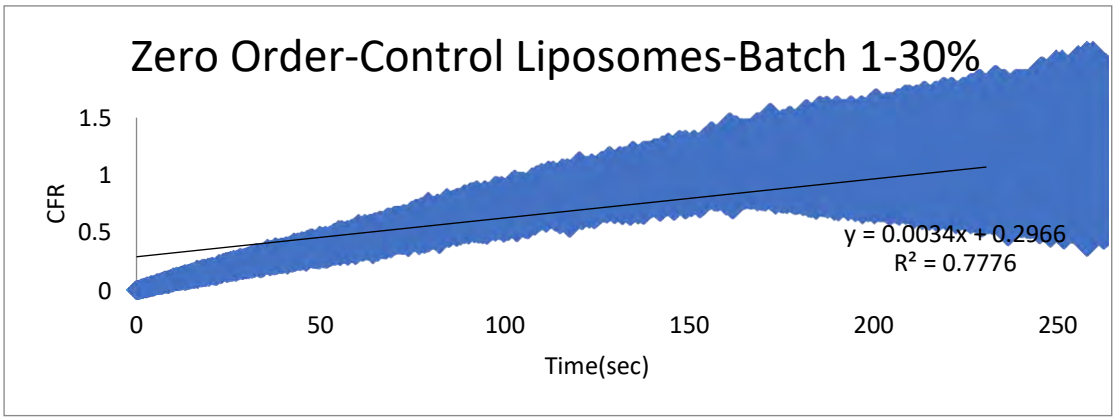

Figure 60: Zero Order model applied on Control liposomes for a power intensity of 17.31 mW/cm^2

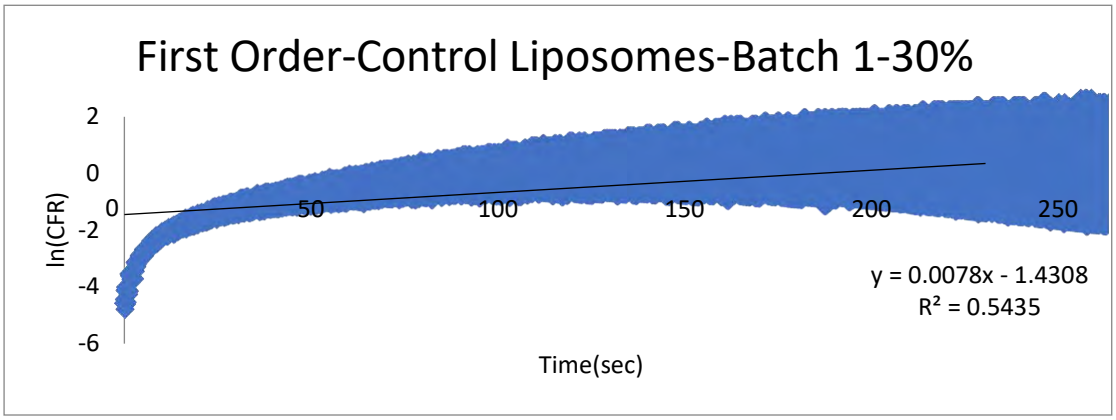

Figure 61: First Order model applied on Control liposomes for a power intensity of 17.31 mW/cm^2

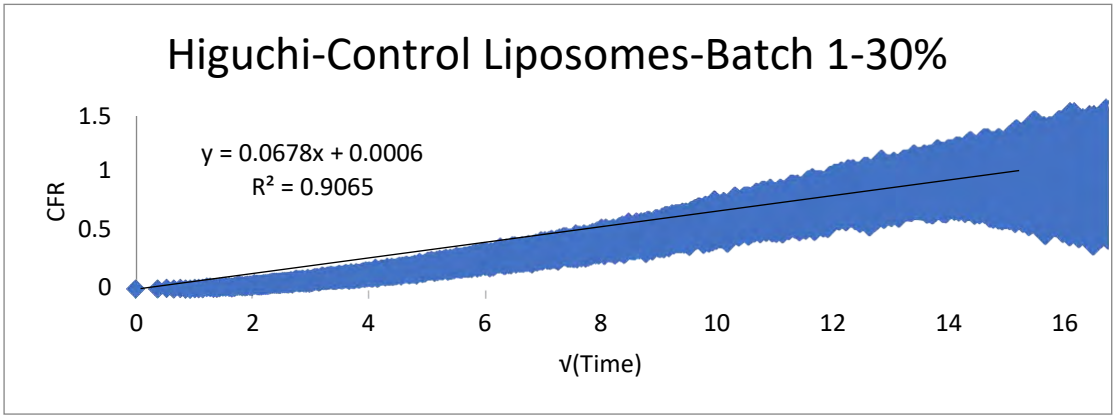

Figure 62:Higuchi model applied on Control liposomes for a power intensity of 17.31 mW/cm^2

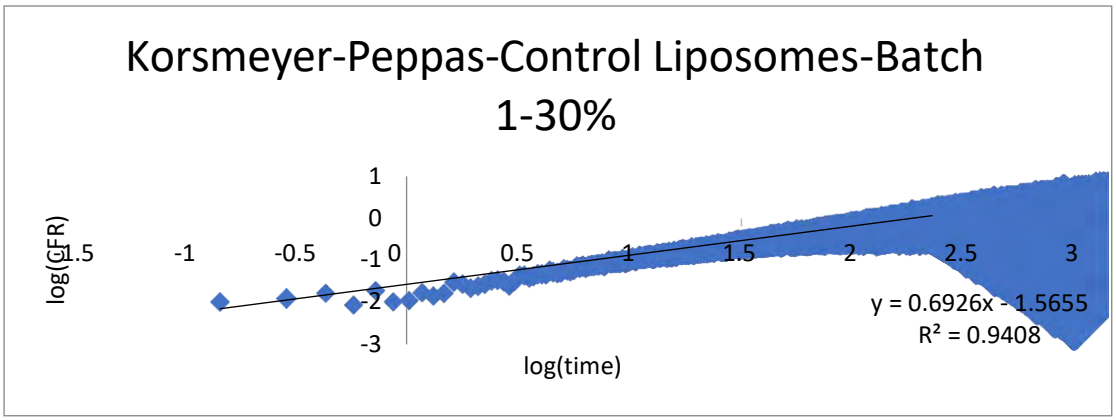

Figure 63: Korsmeyer-Peppas model applied on Control liposomes for a power intensity of 17.31 mW/cm^2

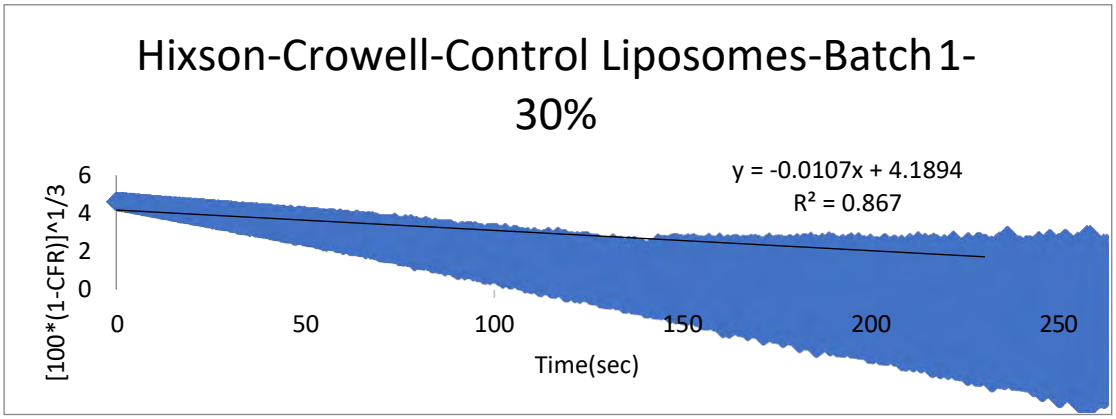

Figure 64: Higuchi model applied on Control liposomes for a power intensity of 17.31 mW/cm^2

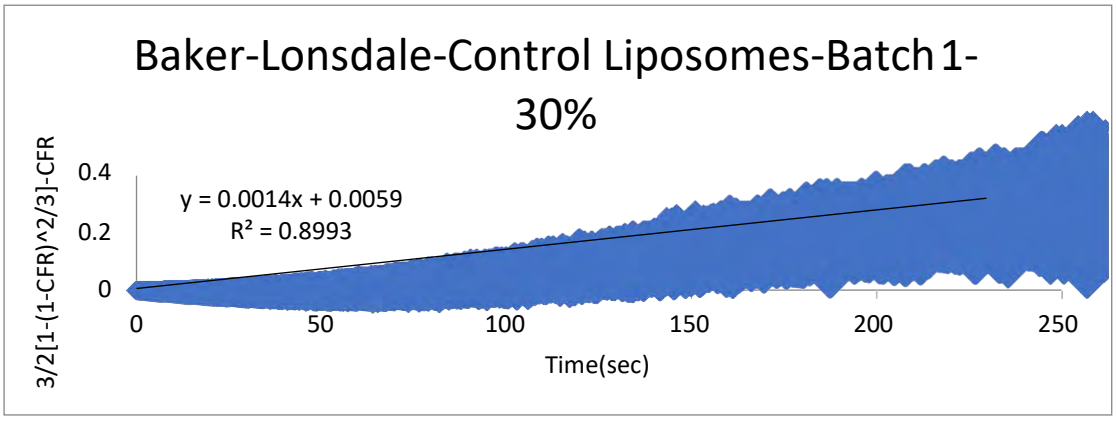

Figure 65:Baker-Lonsdale model applied on Control liposomes for a power intensity of 17.31 mW/cm^2

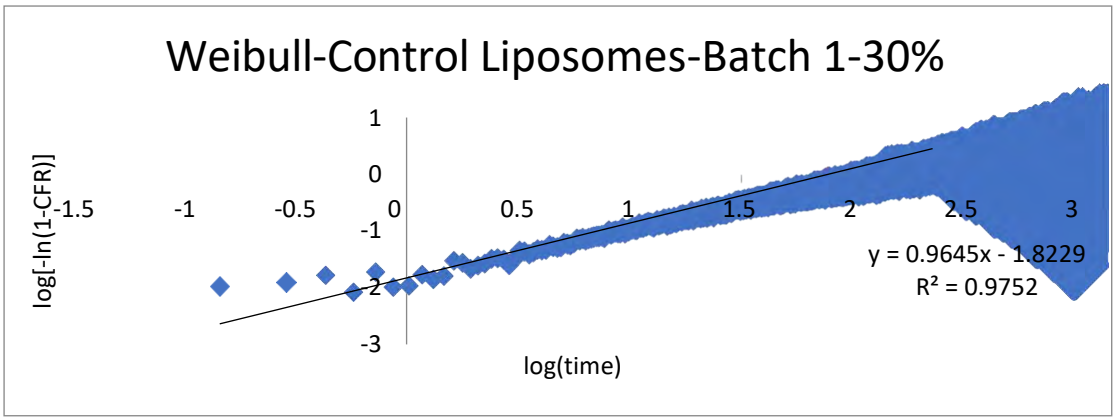

Figure 66:Weibull model applied on Control liposomes for a power intensity of 17.31 mW/cm^2

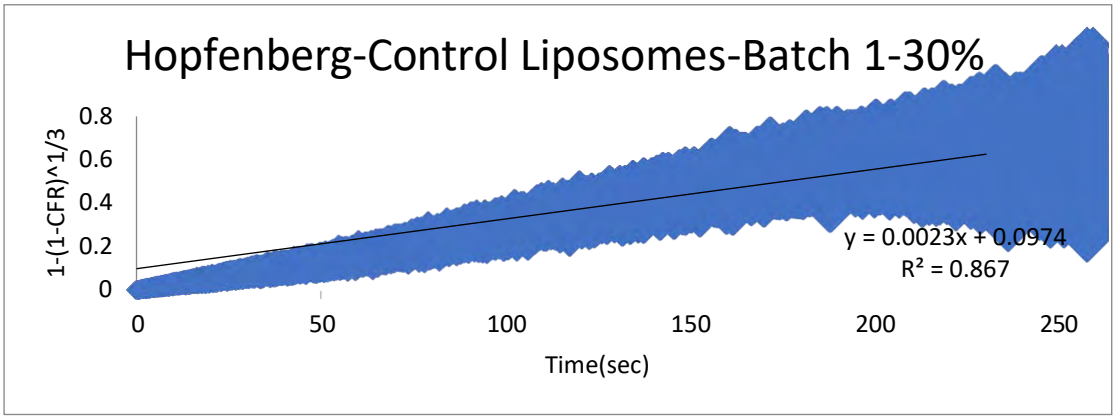

Figure 67: Hopfenberg model applied on Control liposomes for a power intensity of 17.31 mW/cm^2

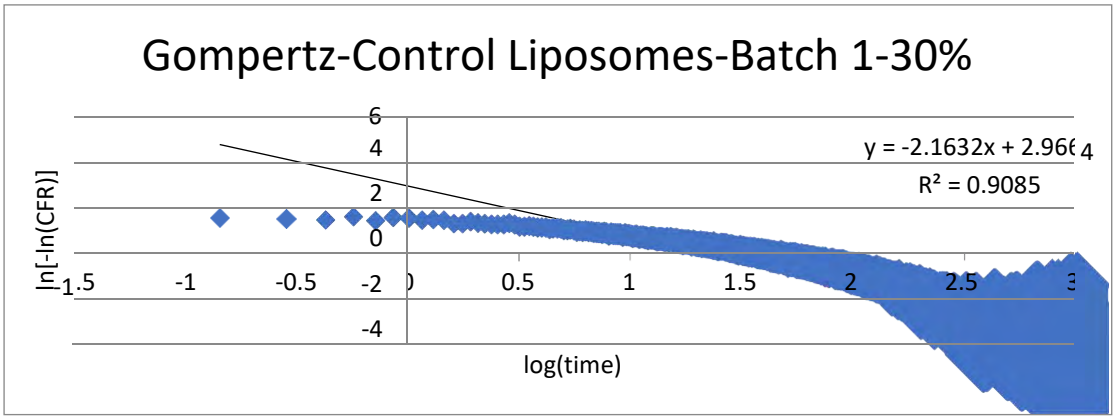

Figure 68: Gompertz model applied on Control liposomes for a power intensity of 17.31 mW/cm^2

Appendix B: Plots of kinetic modeling for Control Liposomes Batch 2

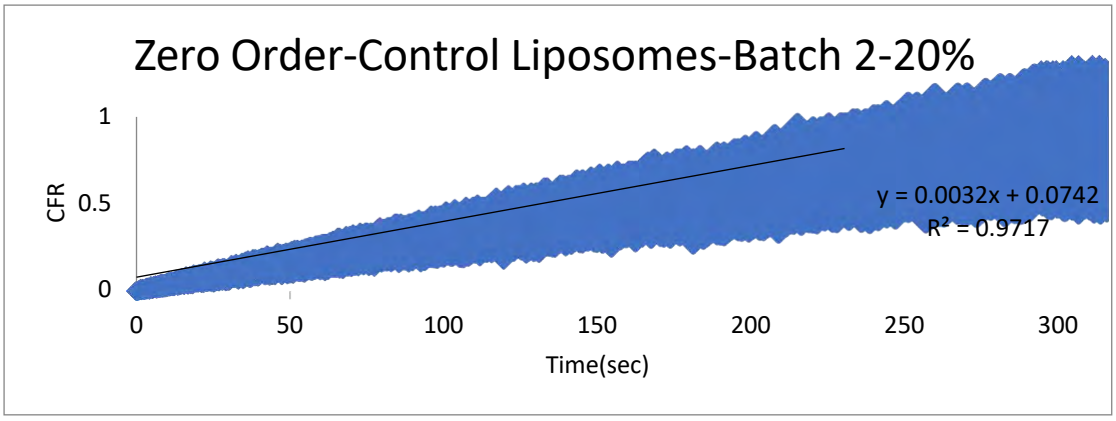

Figure 69: Zero Order model applied on Control liposomes for a power intensity of 7.46 mW/cm^2

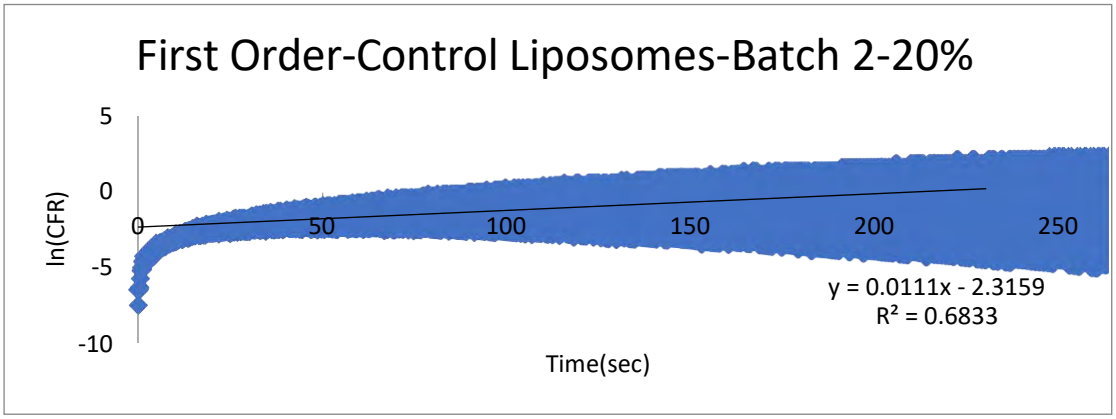

Figure 70:First Order model applied on Control liposomes for a power intensity of 7.46 mW/cm^2

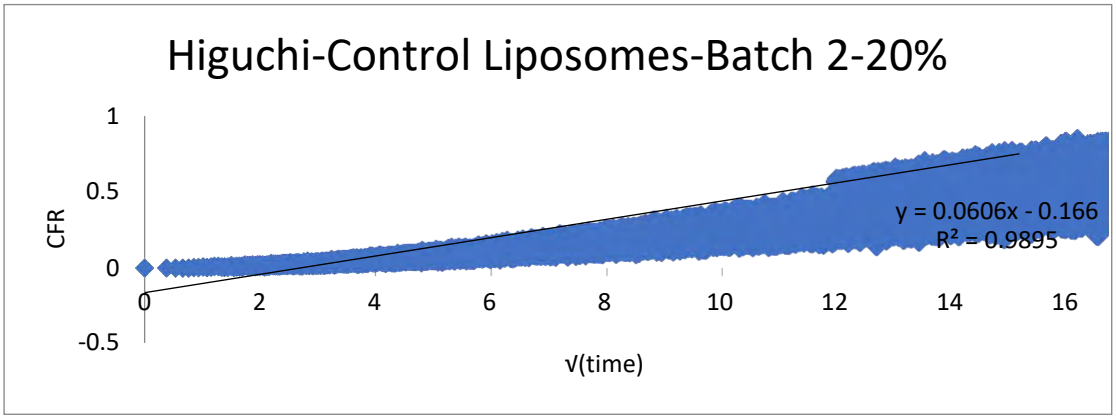

Figure 71:Higuchi model applied on Control liposomes for a power intensity of 7.46 mW/cm^2

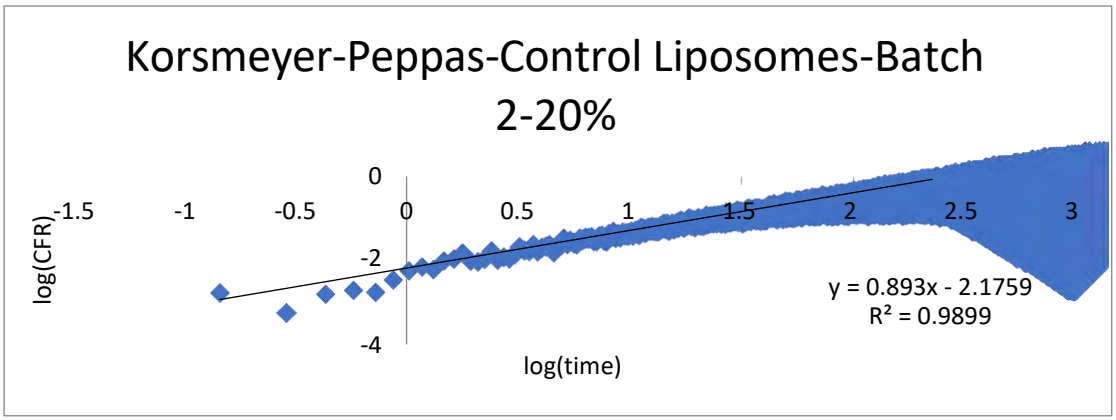

Figure 72:Korsmeyer-Peppas model applied on Control liposomes for a power intensity of 7.46 mW/cm^2

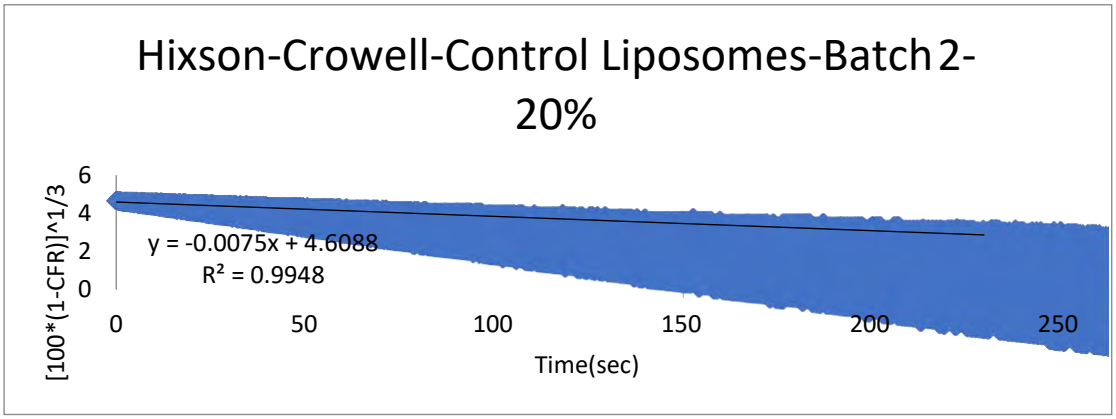

Figure 73:Hixson-Crowell model applied on Control liposomes for a power intensity of 7.46 mW/cm^2

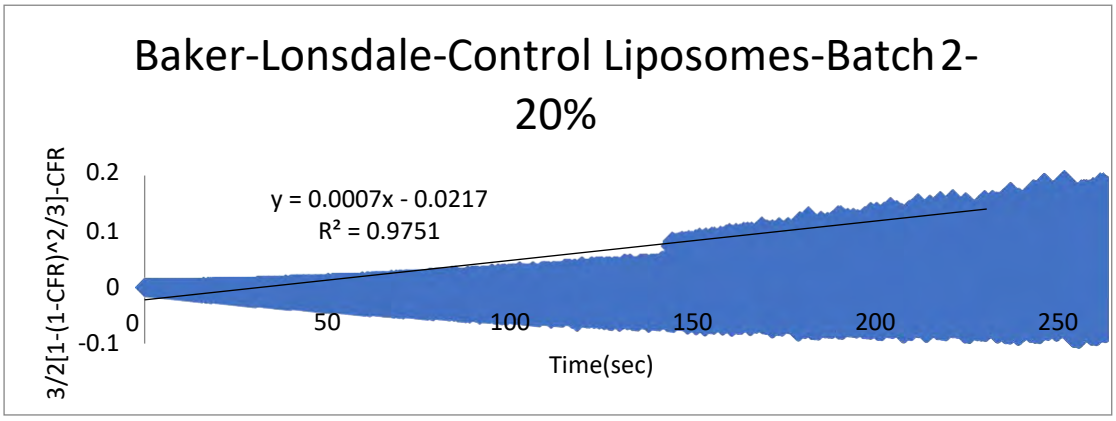

Figure 74:Baker-Lonsdale model applied on Control liposomes for a power intensity of 7.46 mW/cm^2

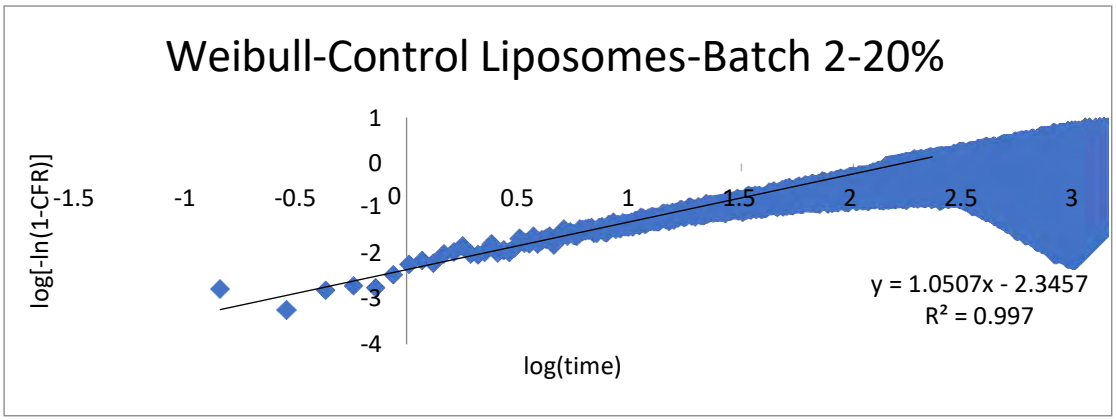

Figure 75:Weibulli model applied on Control liposomes for a power intensity of 7.46 mW/cm^2

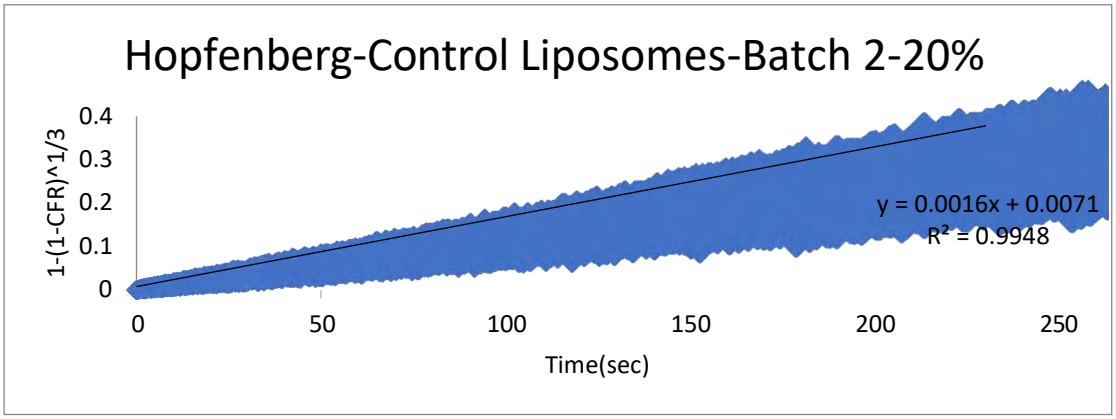

Figure 76:Hopfenberg model applied on Control liposomes for a power intensity of 7.46 mW/cm^2

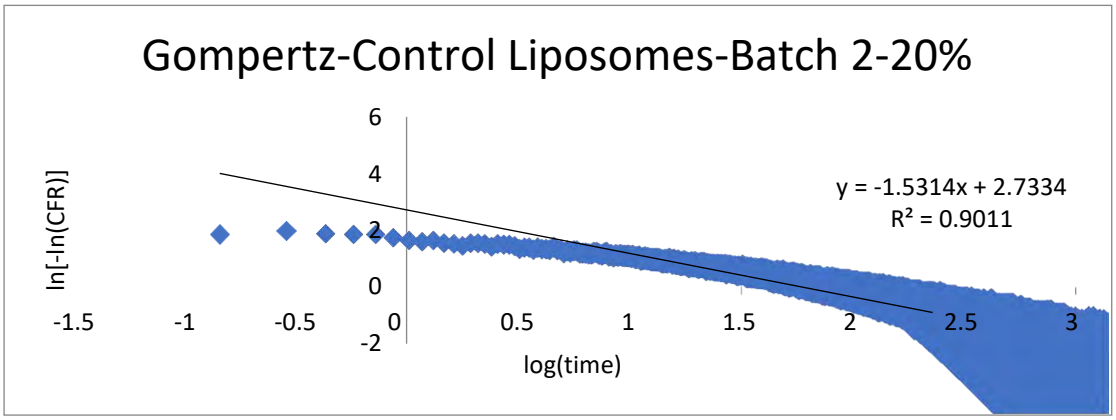

Figure 77:Gompertz model applied on Control liposomes for a power intensity of 7.46 mW/cm^2

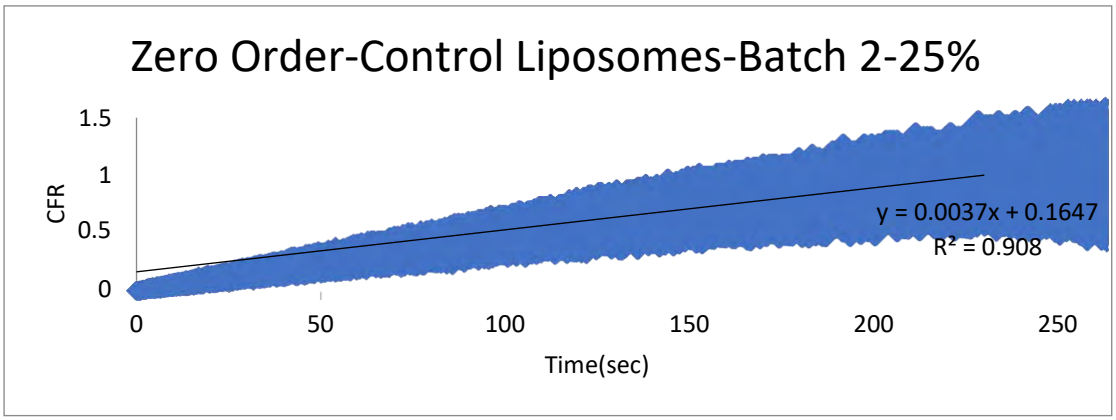

Figure 78: Zero Order model applied on Control liposomes for a power intensity of 9.85 mW/cm^2

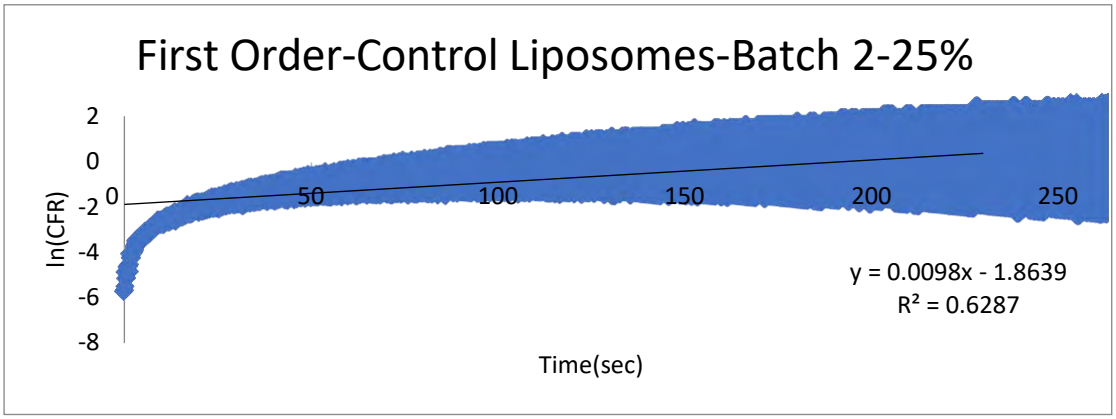

Figure 79: First order model applied on Control liposomes for a power intensity of 9.85 mW/cm^2

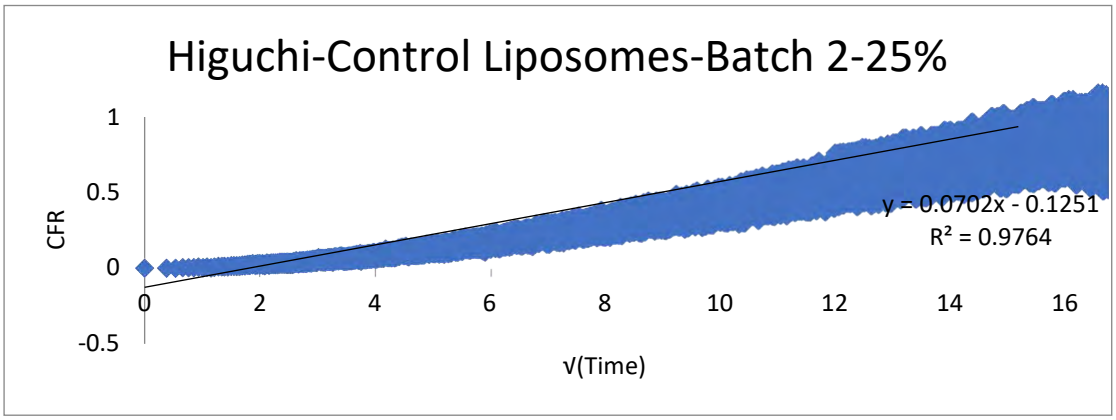

Figure 80: Higuchi model applied on Control liposomes for a power intensity of 9.85 mW/cm^2

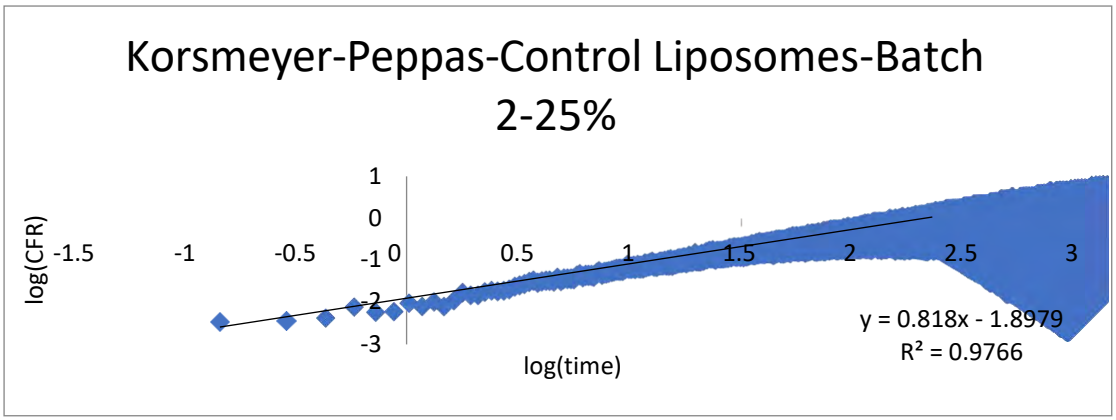

Figure 81 : Korsmeyer-Peppas model applied on Control liposomes for a power intensity of 9.85 mW/cm^2

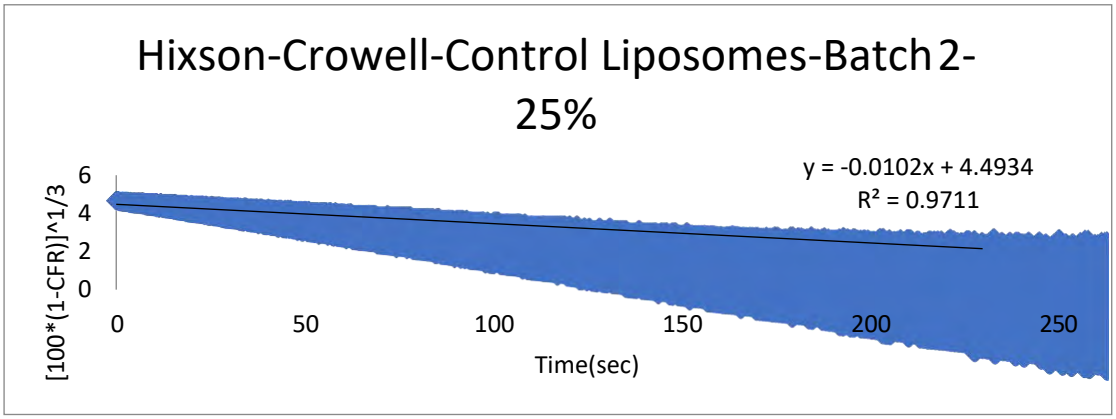

Figure 82: Hixson-Crowell model applied on Control liposomes for a power intensity of 9.85 mW/cm^2

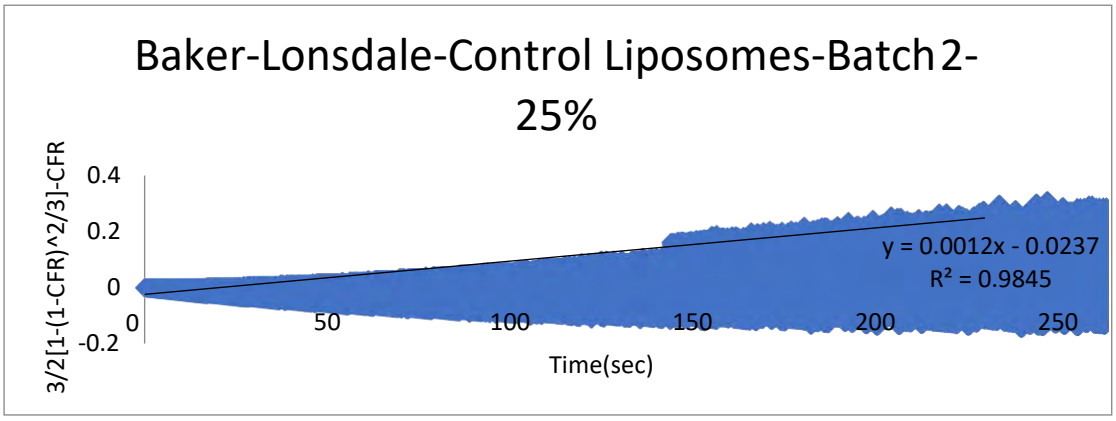

Figure 83: Baker-Lonsdale model applied on Control liposomes for a power intensity of 9.85 mW/cm^2

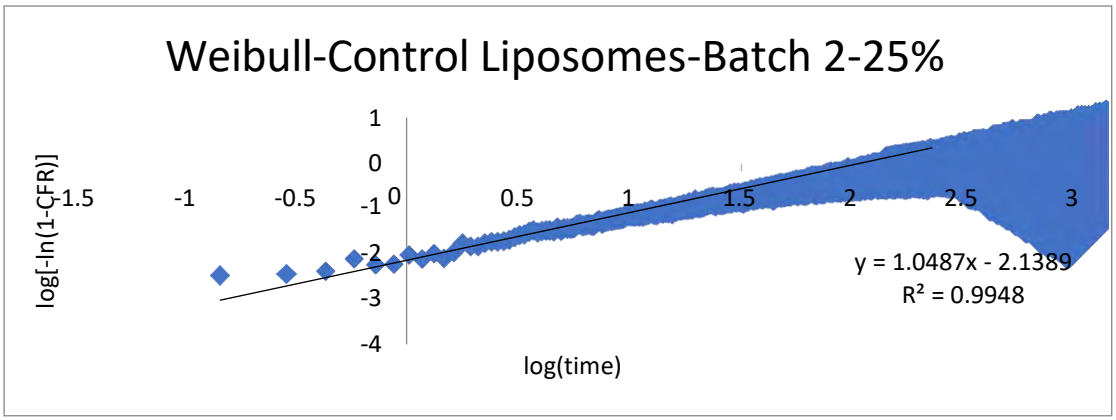

Figure 84: Weibull model applied on Control liposomes for a power intensity of 9.85 mW/cm^2

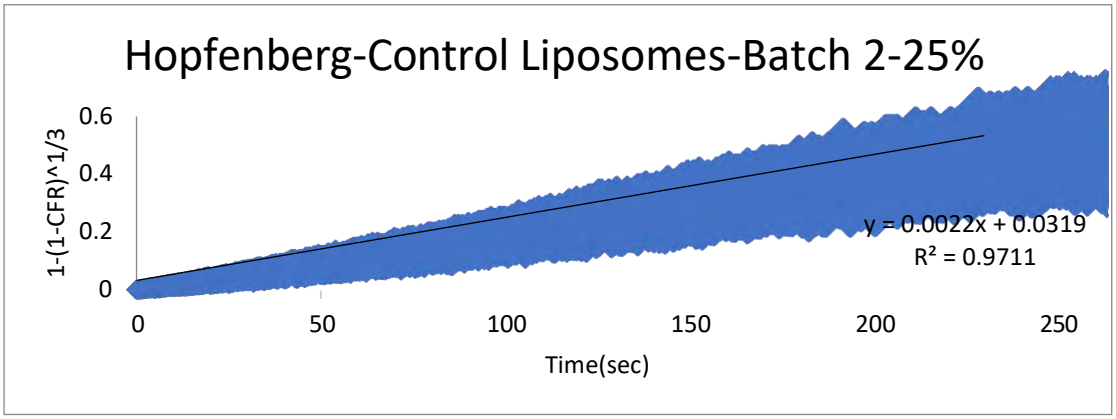

Figure 85: Hopfenberg model applied on Control liposomes for a power intensity of 9.85 mW/cm^2

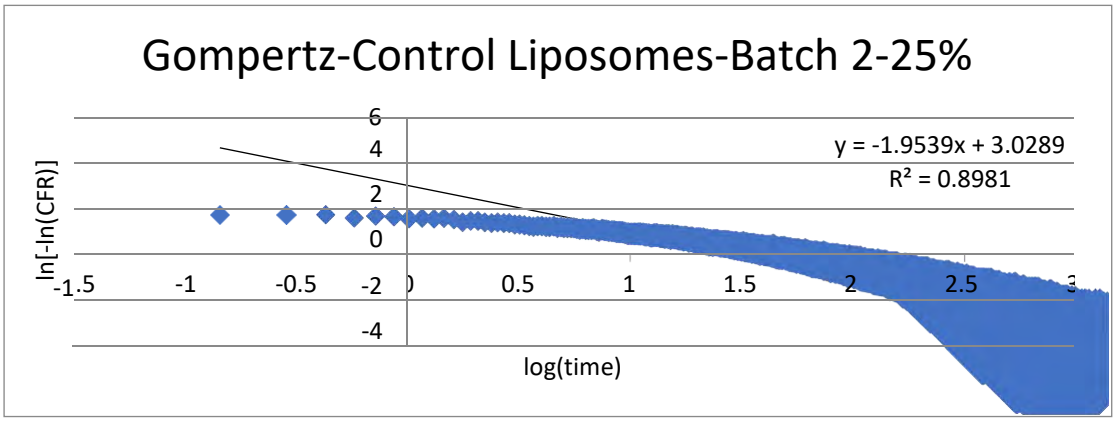

Figure 86: Gompertz model applied on Control liposomes for a power intensity of 9.85 mW/cm^2

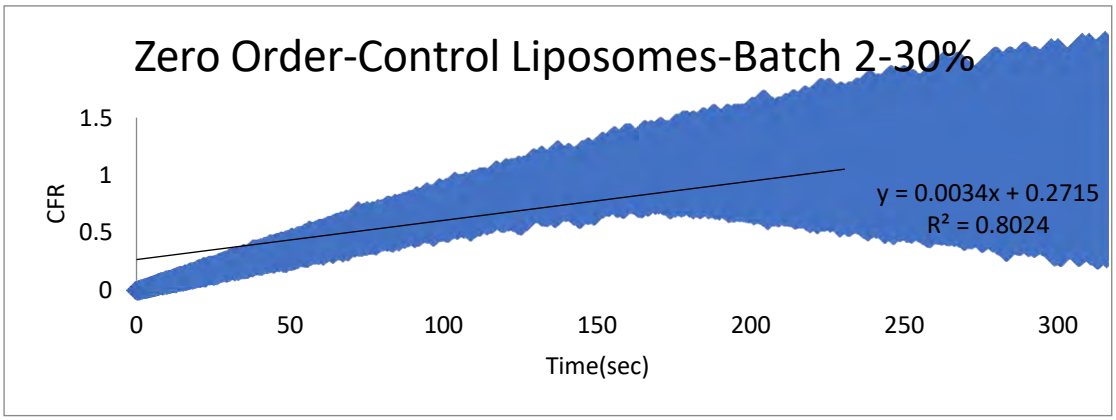

Figure 87: Zero Order model applied on Control liposomes for a power intensity of 17.31 mW/cm^2

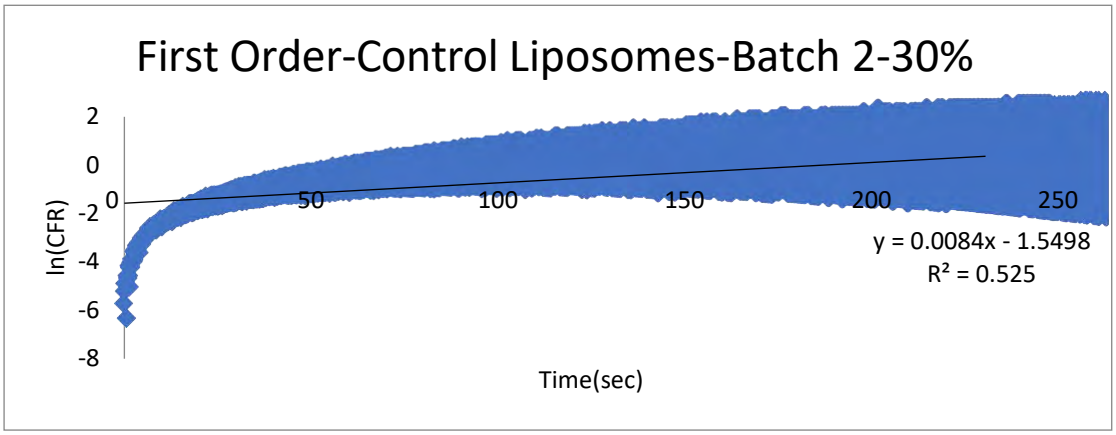

Figure 88: First Order model applied on Control liposomes for a power intensity of 17.31 mW/cm^2

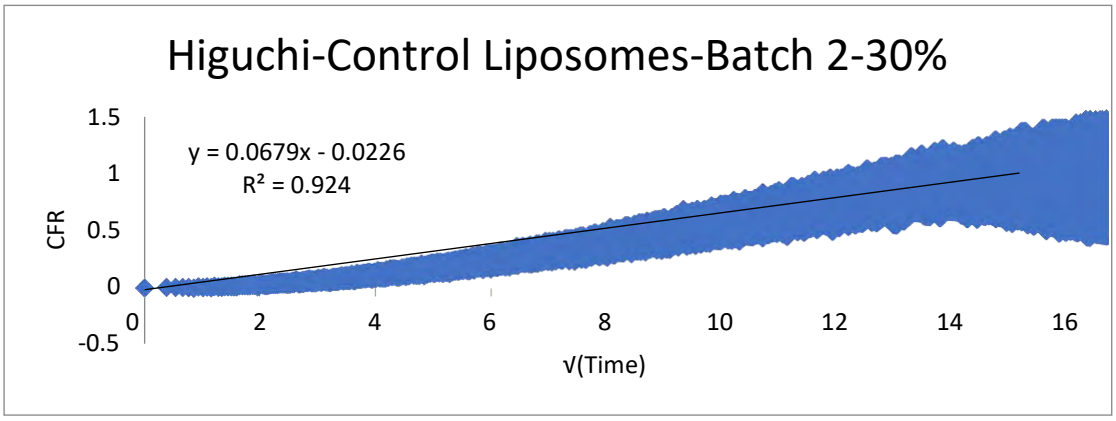

Figure 89:Higuchi model applied on Control liposomes for a power intensity of 17.31 mW/cm^2

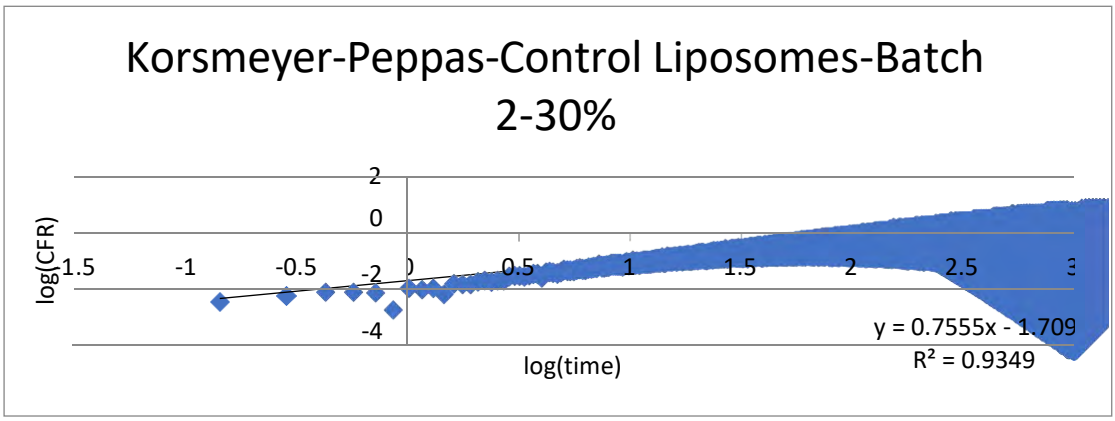

Figure 90:Korsmeyer-Peppas model applied on Control liposomes for a power intensity of 17.31 mW/cm^2

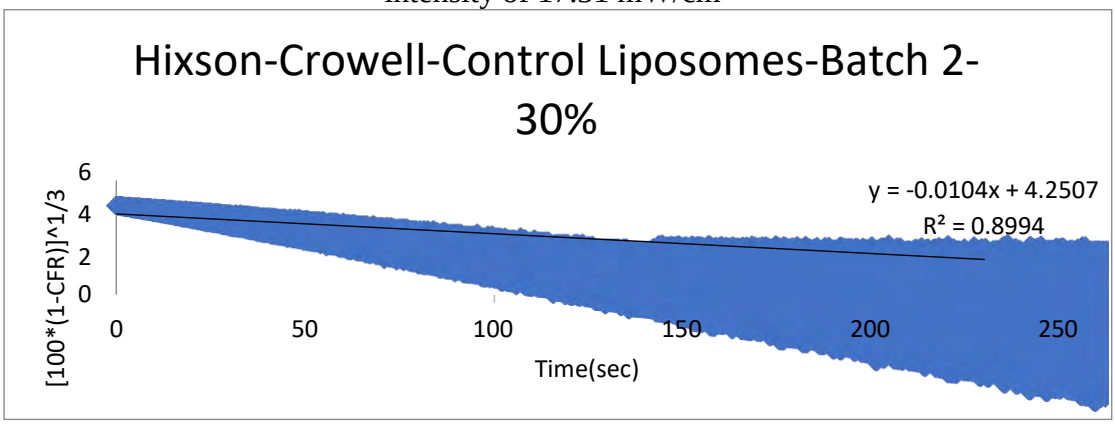

Figure 91:Hixson-Crowell: model applied on Control liposomes for a power intensity of 17.31 mW/cm^2

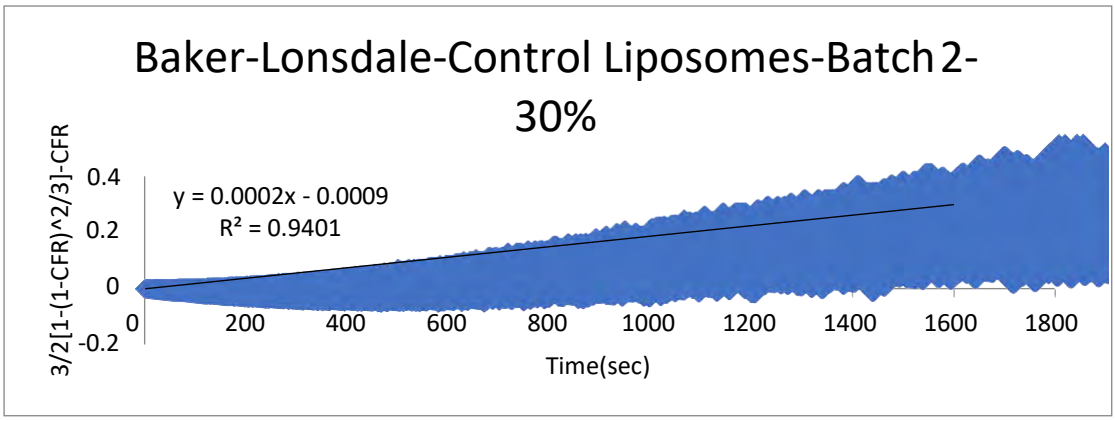

Figure 92: Baker-Lonsdale model applied on Control liposomes for a power intensity of 17.31 mW/cm^2

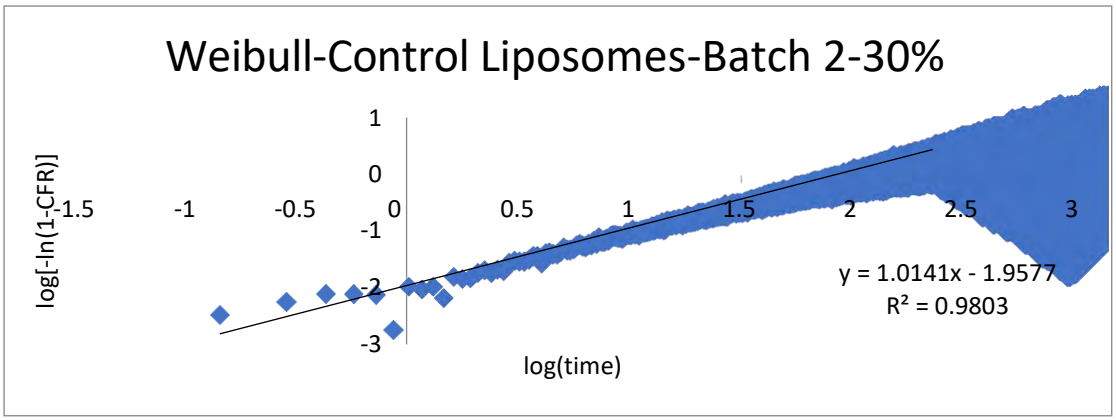

Figure 93: Weibull model applied on Control liposomes for a power intensity of 17.31 mW/cm^2

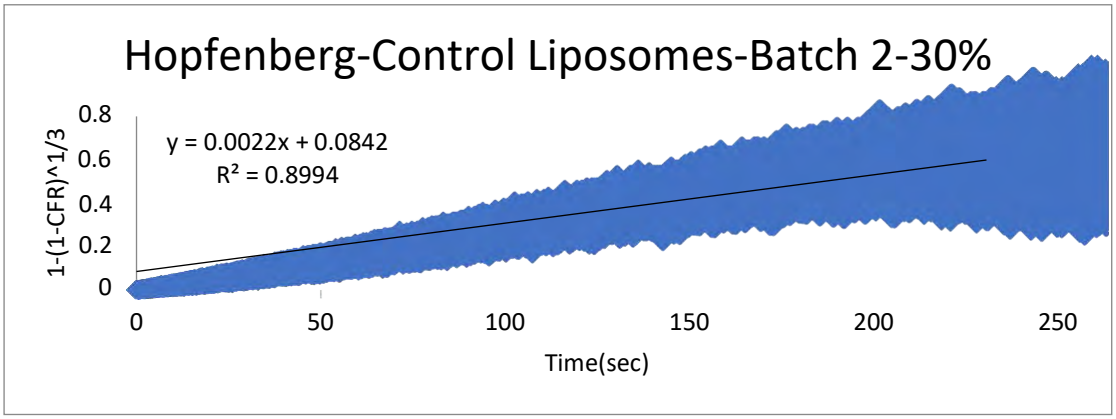

Figure 94: Hopfenberg model applied on Control liposomes for a power intensity of 17.31 mW/cm^2

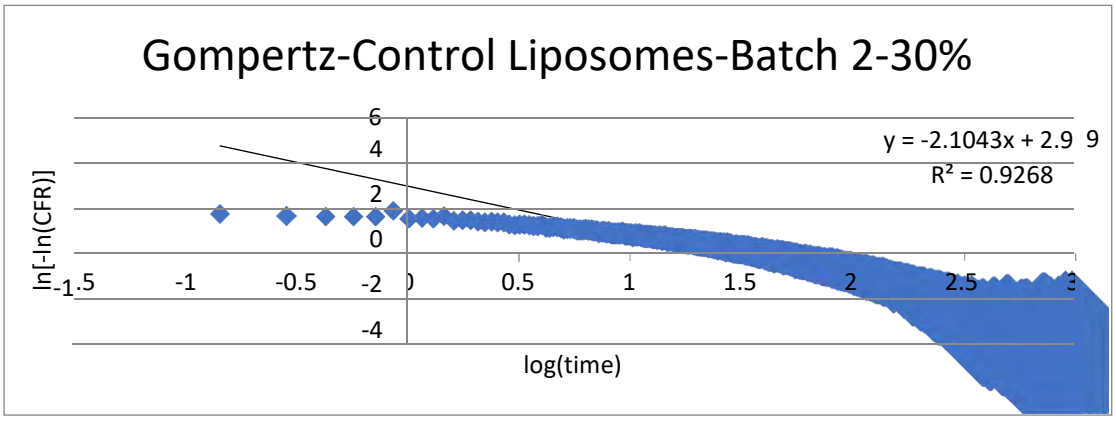

Figure 95: Gompertz model applied on Control liposomes for a power intensity of 17.31 mW/cm^2

Appendix C: Plots of kinetic modeling for Control Liposomes Batch 3

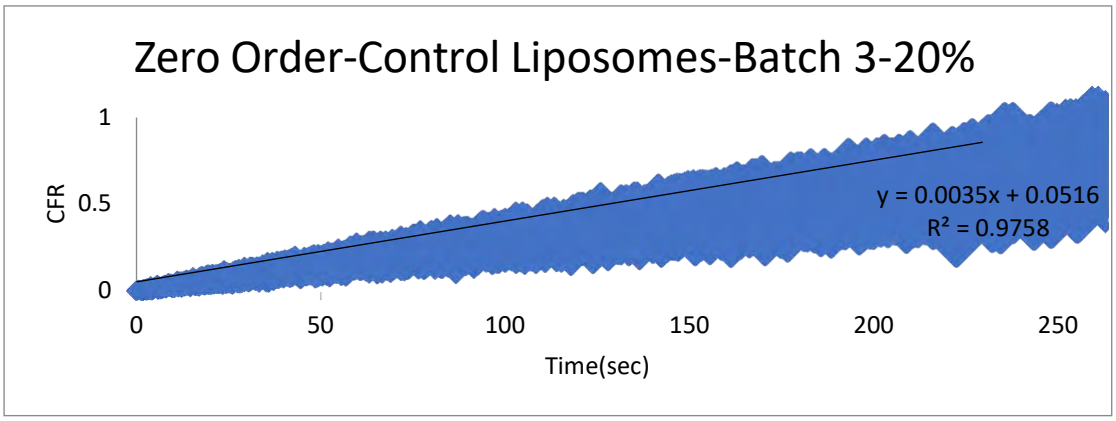

Figure 96: Zero order model applied on Control liposomes for a power intensity of 7.46 mW/cm^2

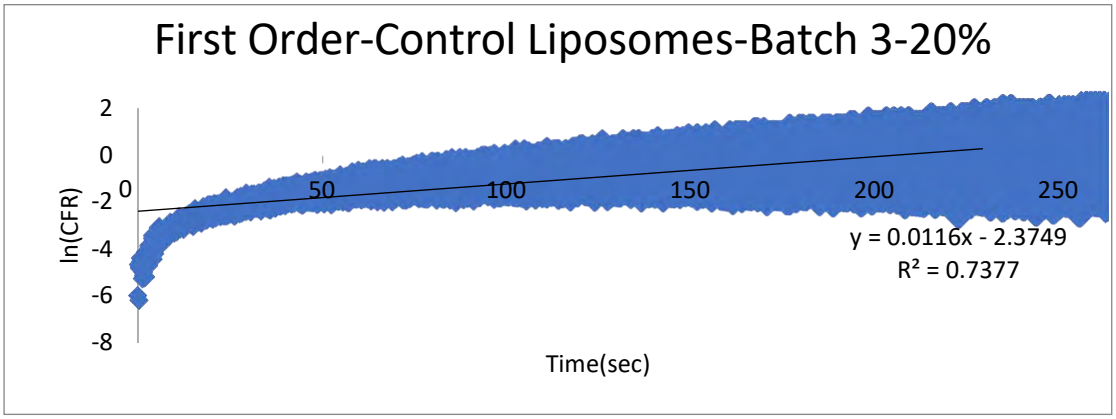

Figure 97:First Order model applied on Control liposomes for a power intensity of 7.46 mW/cm^2

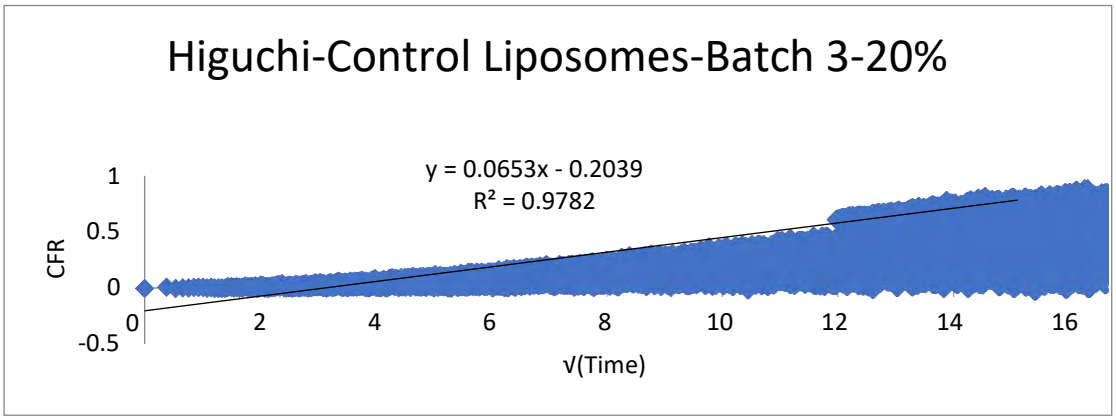

Figure 98: Higuchi model applied on Control liposomes for a power intensity of 7.46 mW/cm^2

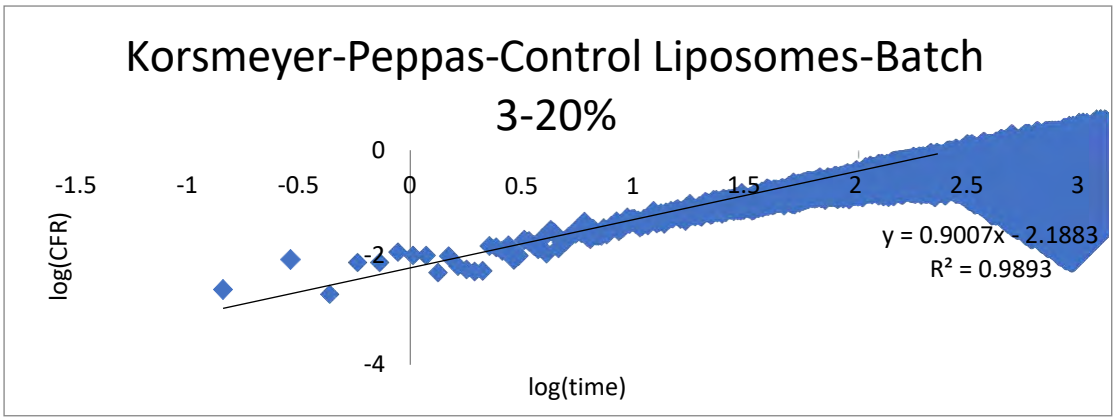

Figure 99: Korsmeyer-Peppas model applied on Control liposomes for a power intensity of 7.46 mW/cm^2

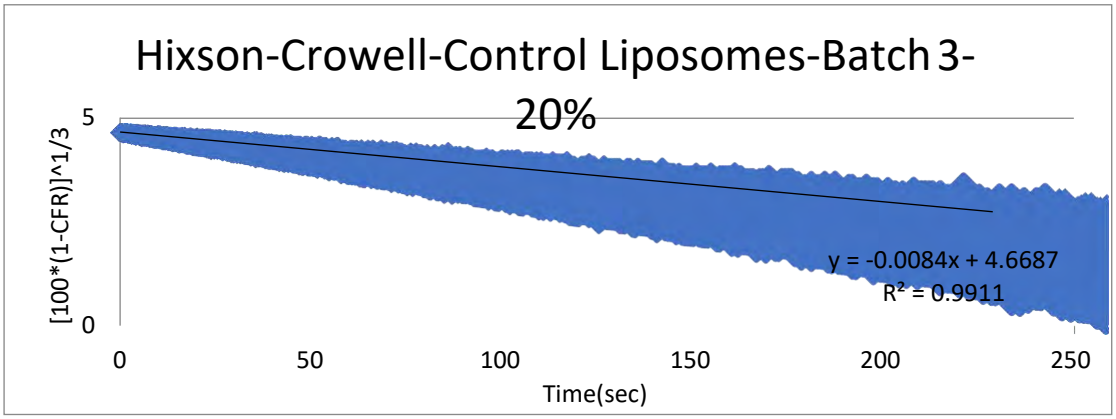

Figure 100:Hixson-Crowell model applied on Control liposomes for a power intensity of 7.46 mW/cm^2

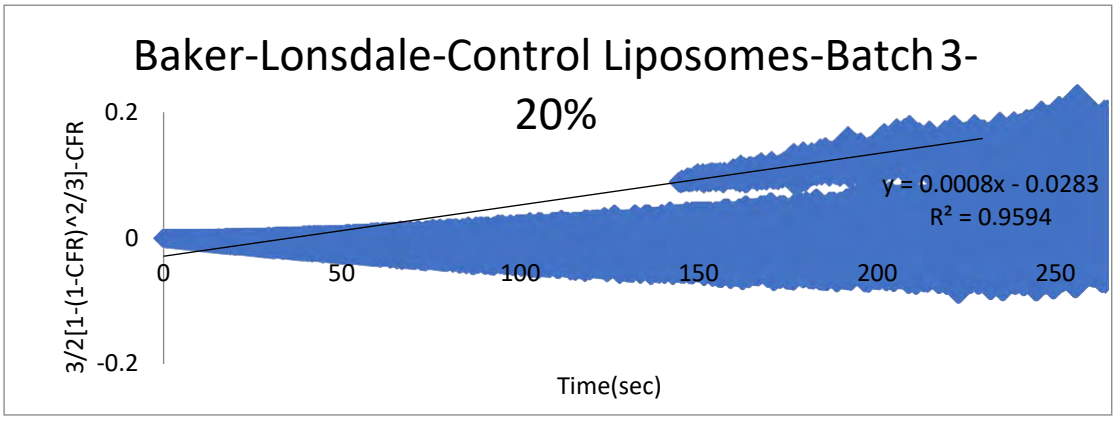

Figure 101: Baker-Lonsdale model applied on Control liposomes for a power intensity of 7.46 mW/cm^2

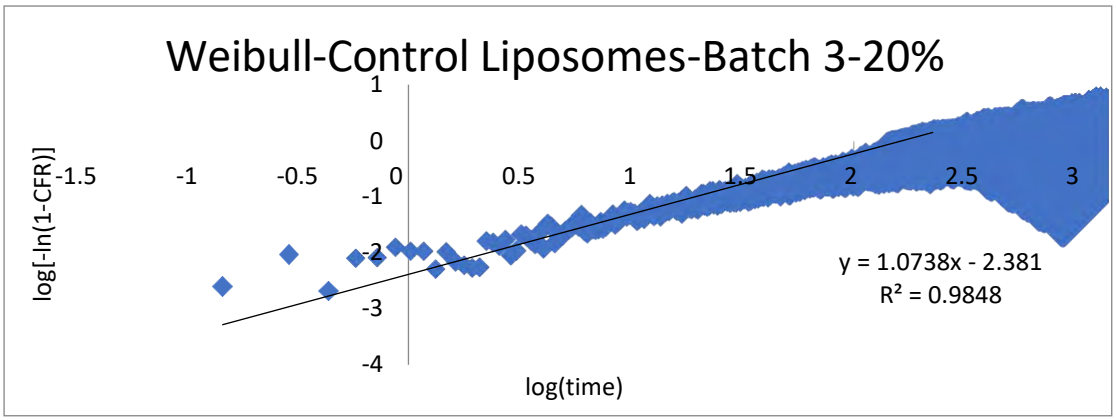

Figure 102: Weibull model applied on Control liposomes for a power intensity of 7.46 mW/cm^2

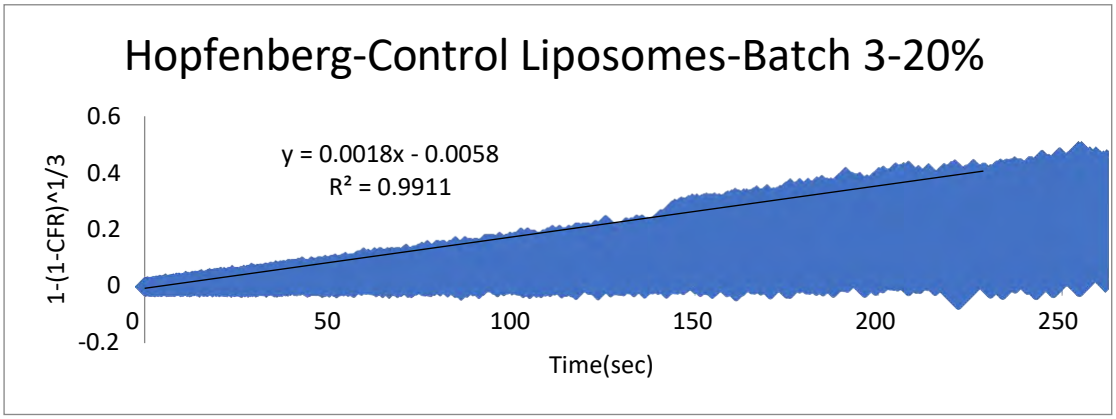

Figure 103: Hopfenberg model applied on Control liposomes for a power intensity of 7.46 mW/cm^2

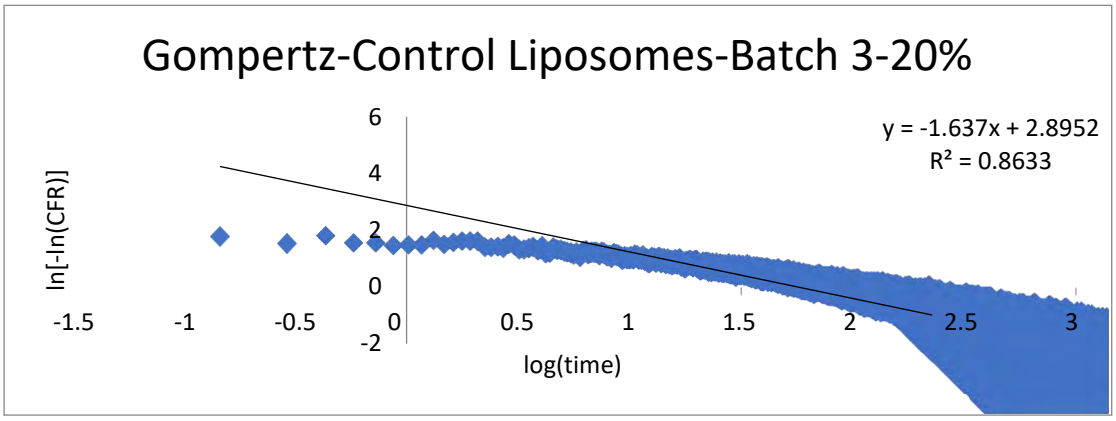

Figure 104: Gompertz model applied on Control liposomes for a power intensity of 7.46 mW/cm^2

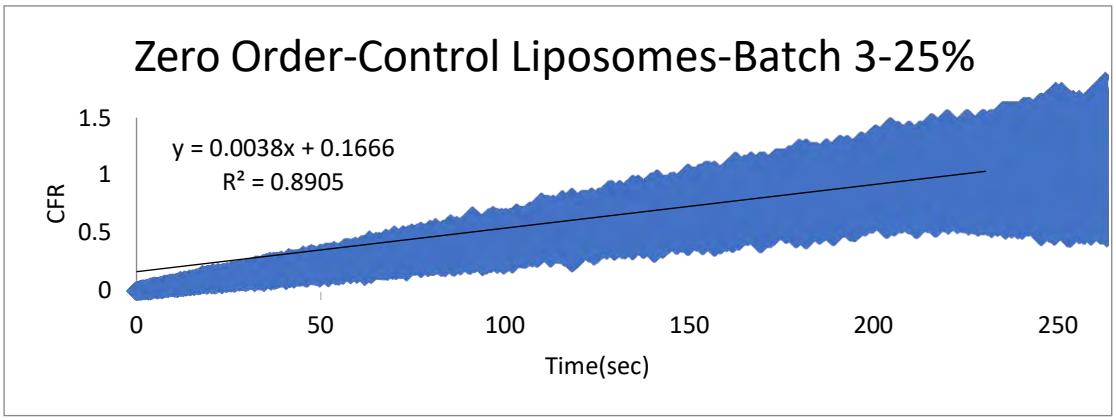

Figure 105: Zero order model applied on Control liposomes for a power intensity of 9.85 mW/cm^2

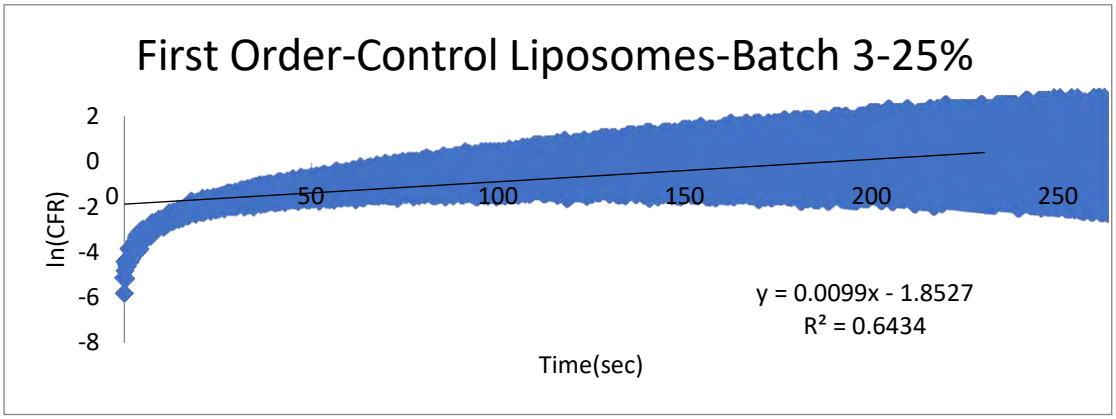

Figure 106:First order model applied on Control liposomes for a power intensity of 9.85 mW/cm^2

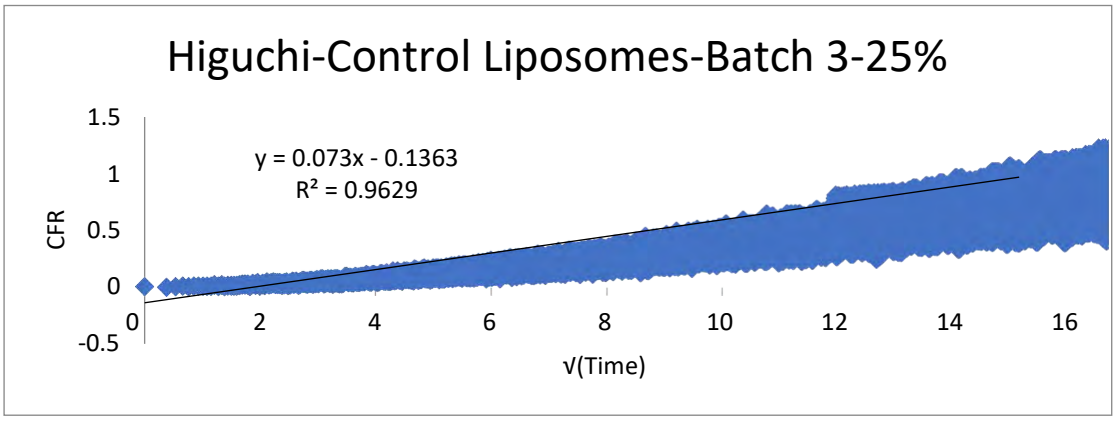

Figure 107: Higuchi model applied on Control liposomes for a power intensity of 9.85 mW/cm^2

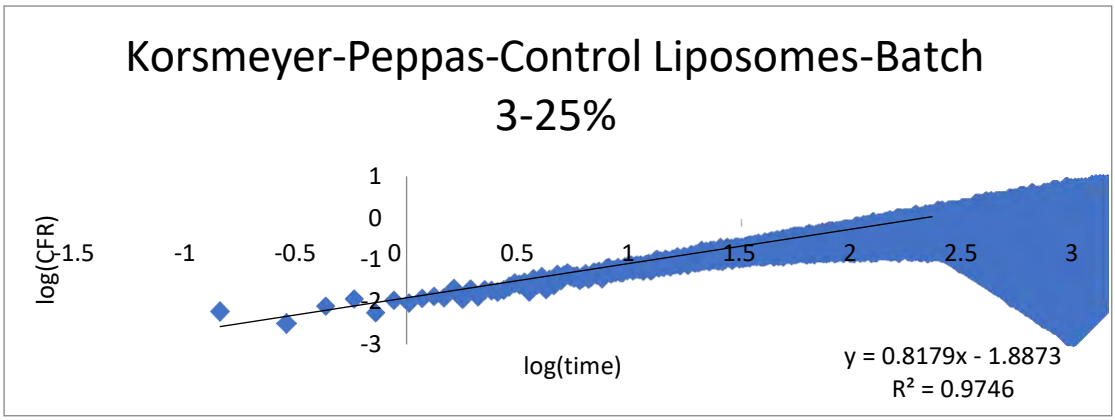

Figure 108: Korsmeyer-Peppas model applied on Control liposomes for a power intensity of 9.85 mW/cm^2

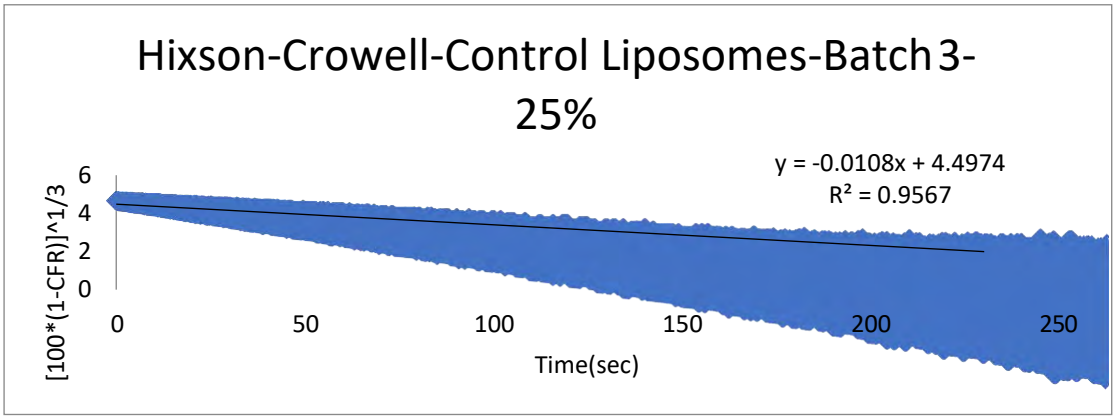

Figure 109: Hixson-Crowell model applied on Control liposomes for a power intensity of 9.85 mW/cm^2

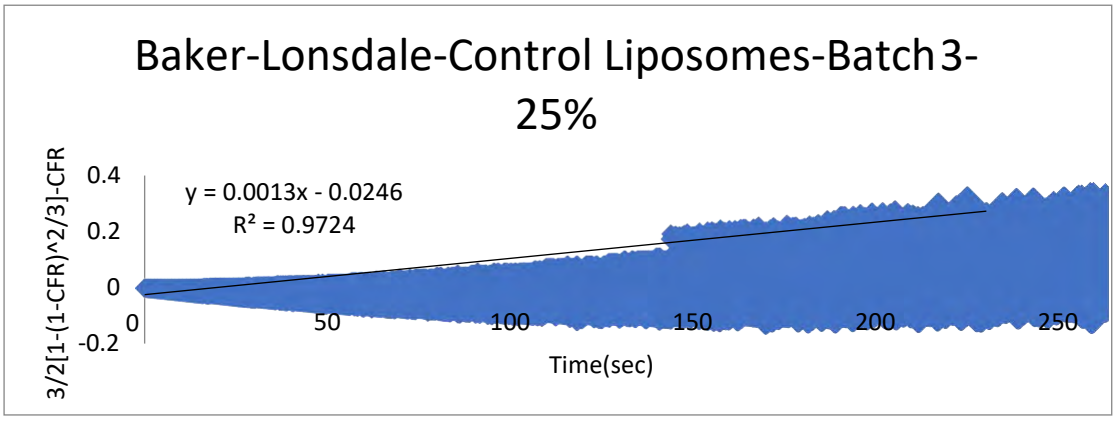

Figure 110: Baker-Lonsdale model applied on Control liposomes for a power intensity of 9.85 mW/cm^2

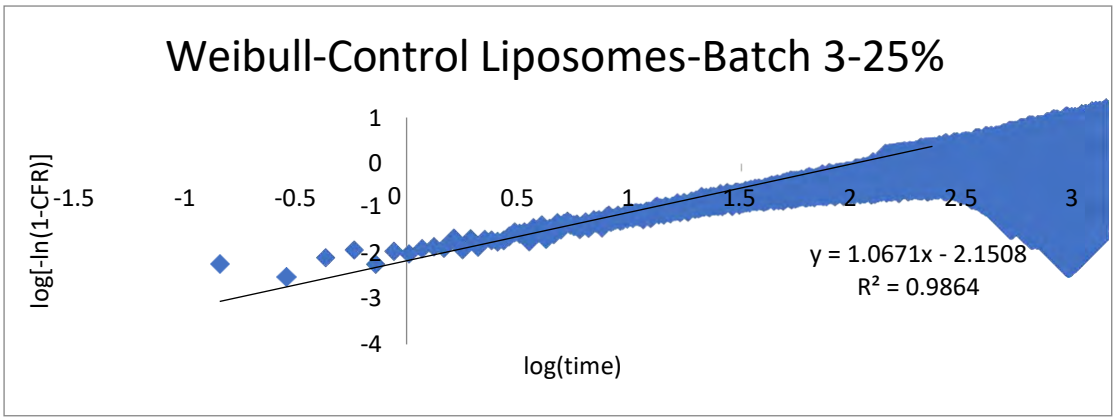

Figure 111: Weibull model applied on Control liposomes for a power intensity of 9.85 mW/cm^2

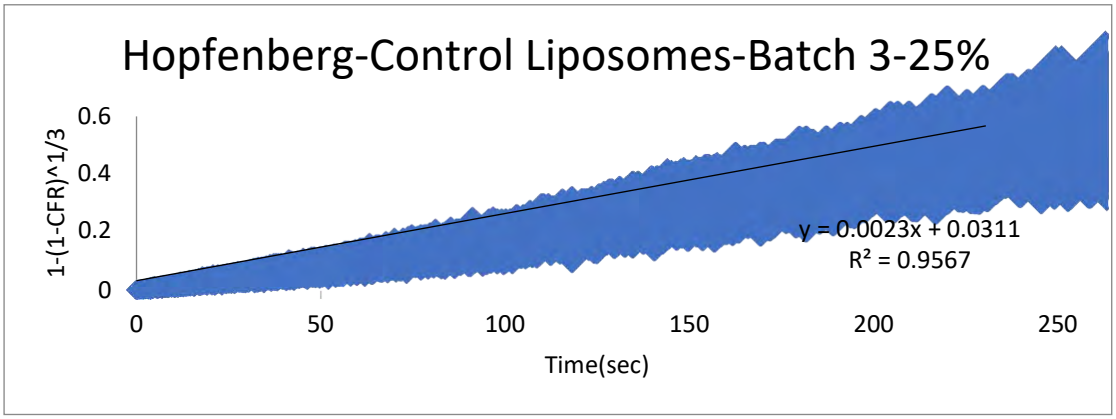

Figure 112: Hopfenberg model applied on Control liposomes for a power intensity of 9.85 mW/cm^2

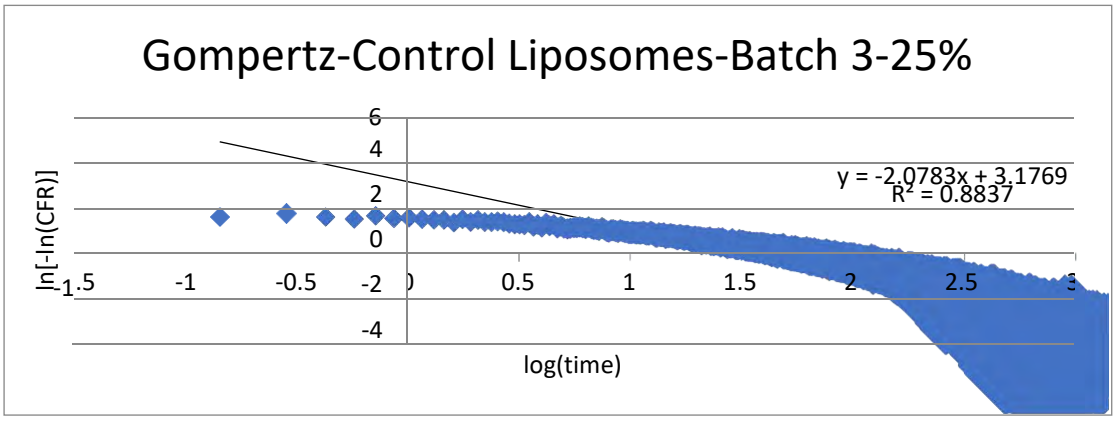

Figure 113: Gompertz model applied on Control liposomes for a power intensity of 9.85 mW/cm^2

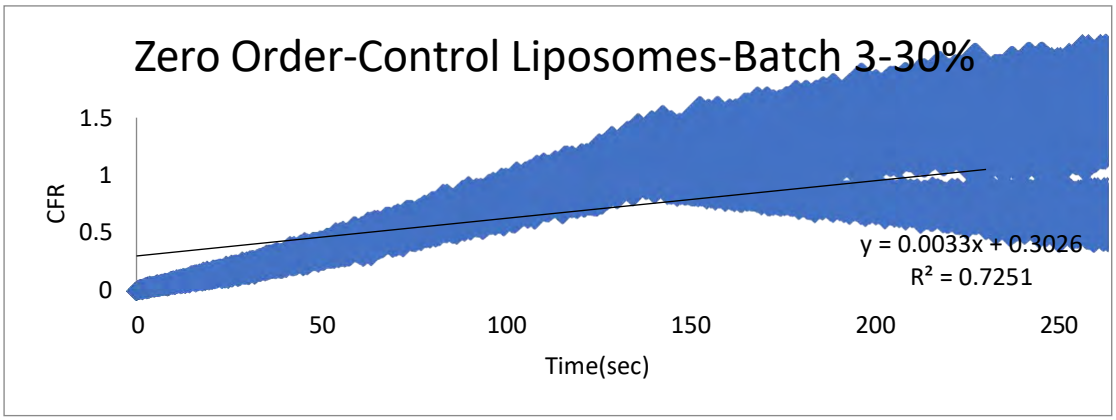

Figure 114: Zero order model applied on Control liposomes for a power intensity of 17.31 mW/cm^2

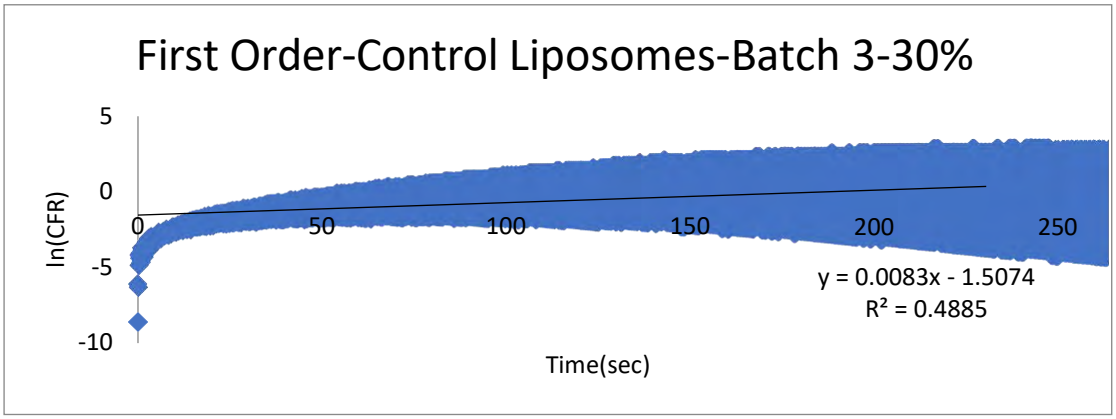

Figure 115: First order model applied on Control liposomes for a power intensity of 17.31 mW/cm^2

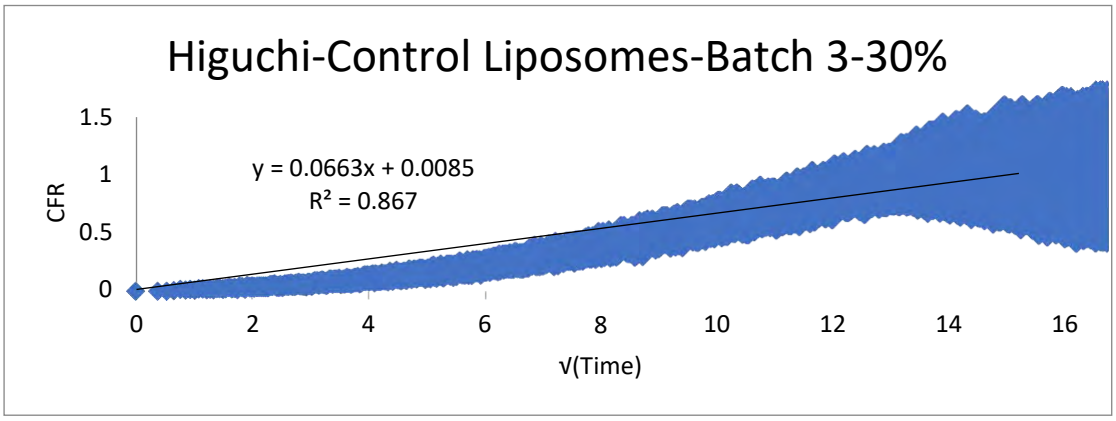

Figure 116:Higuchi model applied on Control liposomes for a power intensity of 17.31 mW/cm2

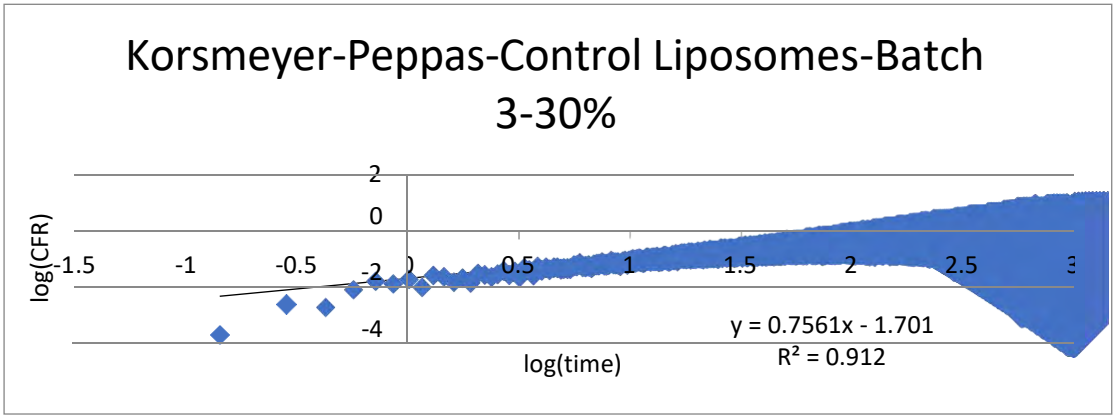

Figure 117: Korsmeyer-Peppas model applied on Control liposomes for a power intensity of 17.31 mW/cm^2

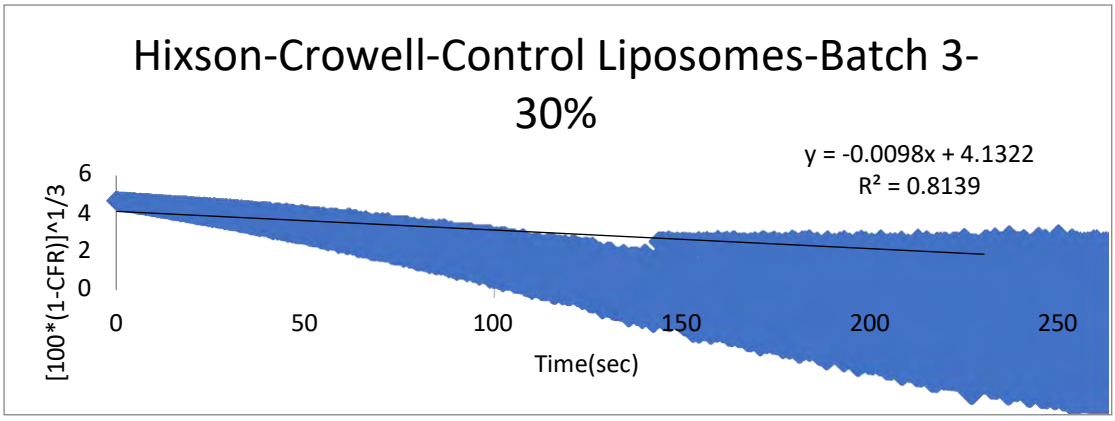

Figure 118: Hixson-Crowell model applied on Control liposomes for a power intensity of 17.31 mW/cm^2

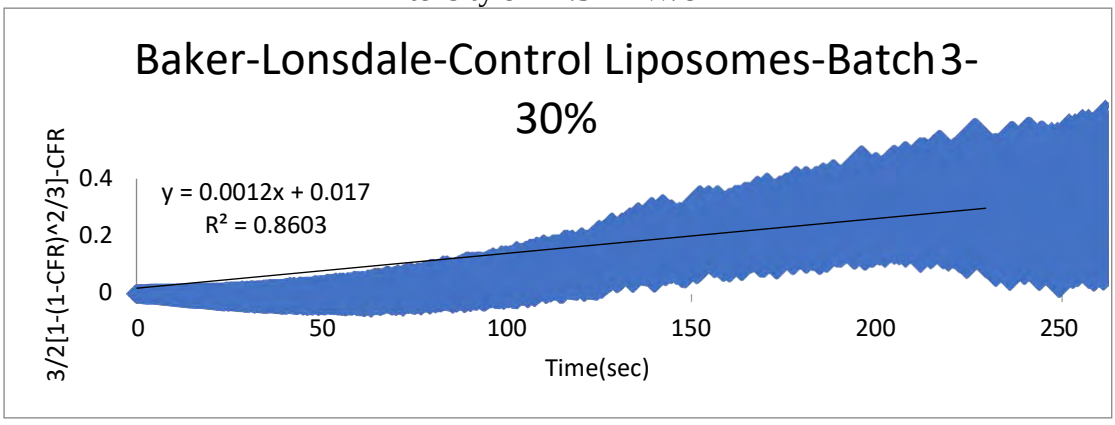

Figure 119: Baker-Lonsdale model applied on Control liposomes for a power intensity of 17.31 mW/cm^2

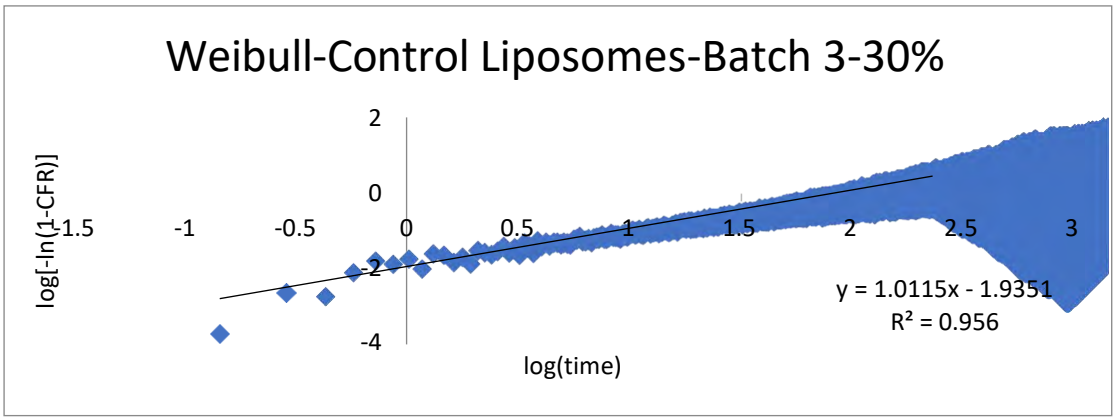

Figure 120: Weibull model applied on Control liposomes for a power intensity of 17.31 mW/cm^2

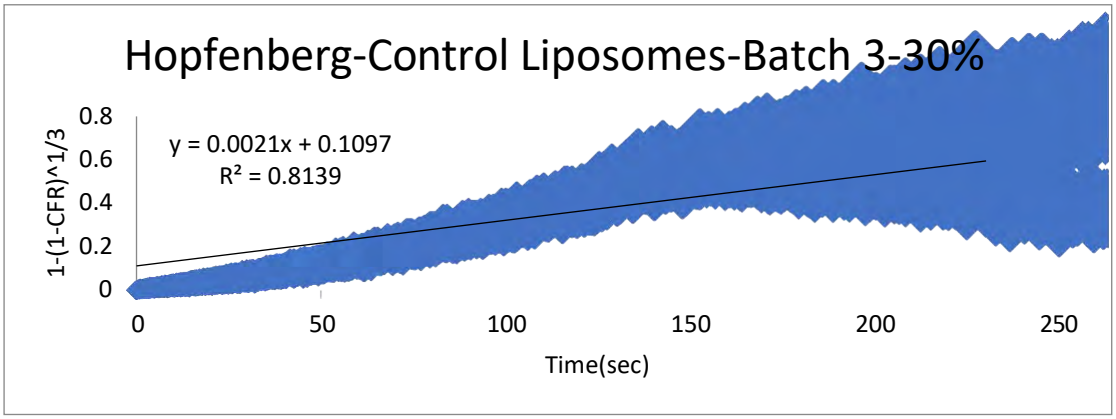

Figure 121: Hopfenberg model applied on Control liposomes for a power intensity of 17.31 mW/cm^2

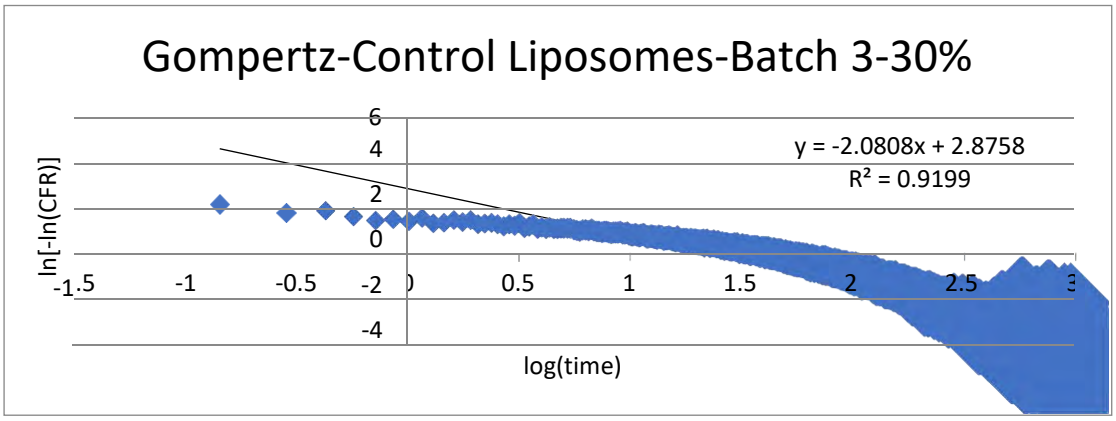

Figure 122: Gompertz model applied on Control liposomes for a power intensity of 17.31 mW/cm^2

Appendix D: Plots of kinetic modeling for LA Liposomes Batch 1

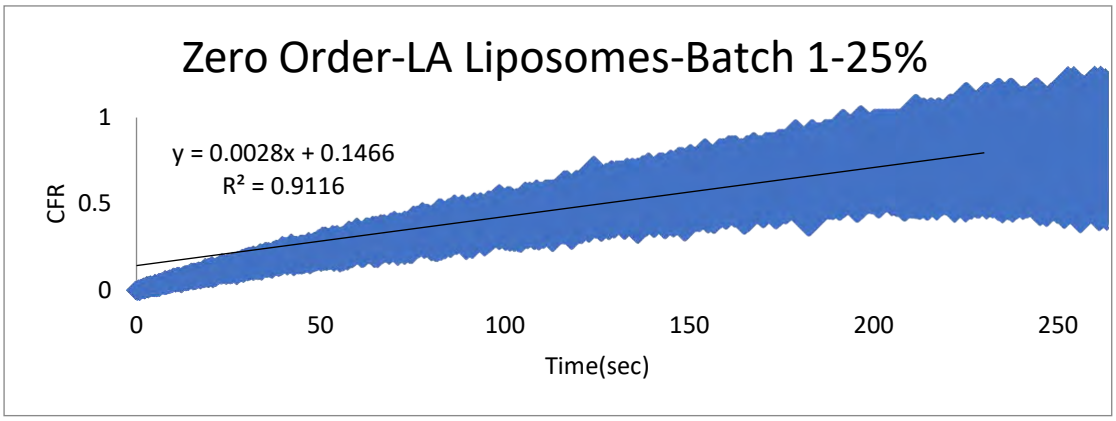

Figure 123: Zero order model applied on LA liposomes for a power intensity of 9.85 mW/cm^2

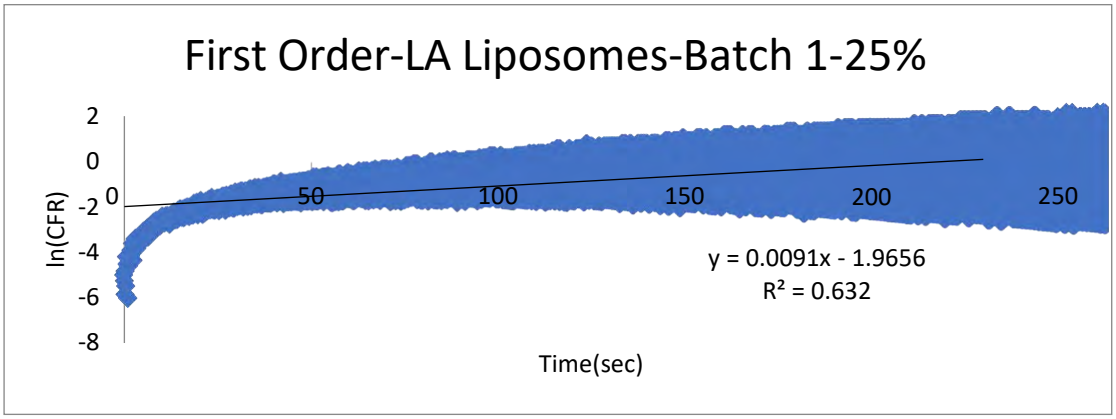

Figure 124: First Order model applied on LA liposomes for a power intensity of 9.85 mW/cm^2

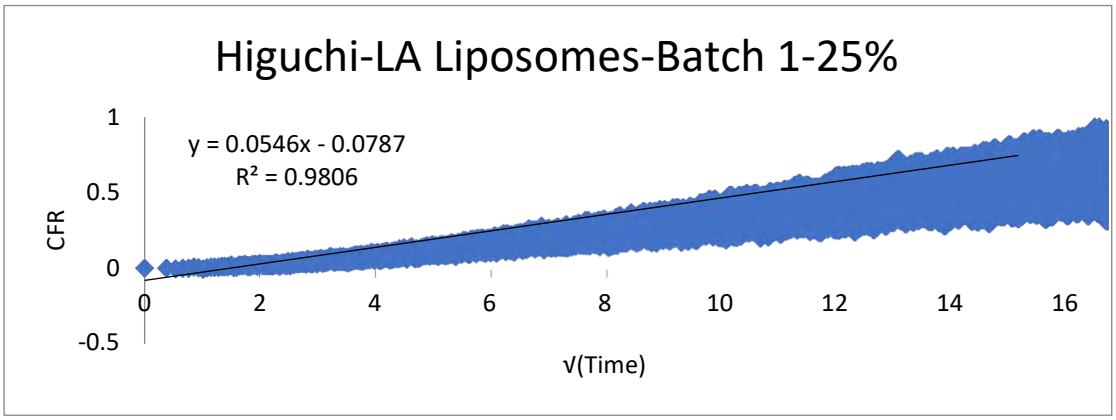

Figure 125:Higuchi model applied on LA liposomes for a power intensity of 9.85 mW/cm^2

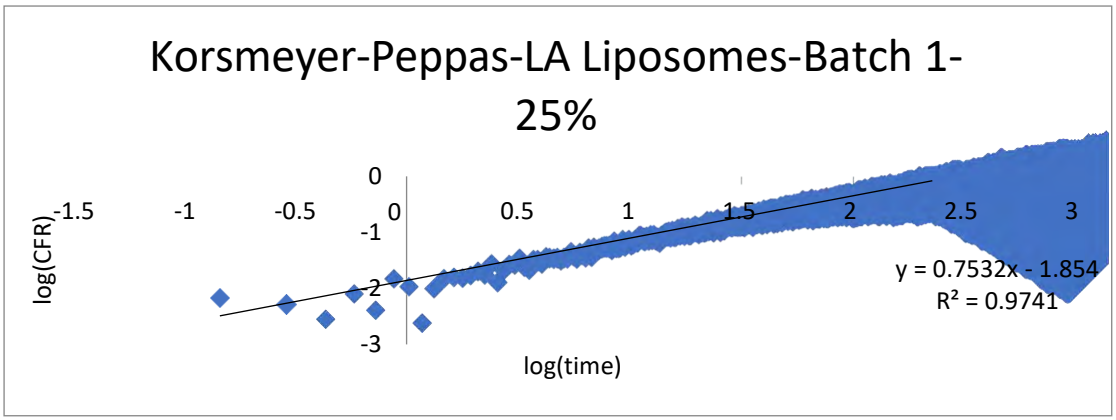

Figure 126:Korsmeyer-Peppas model applied on LA liposomes for a power intensity of 9.85 mW/cm^2

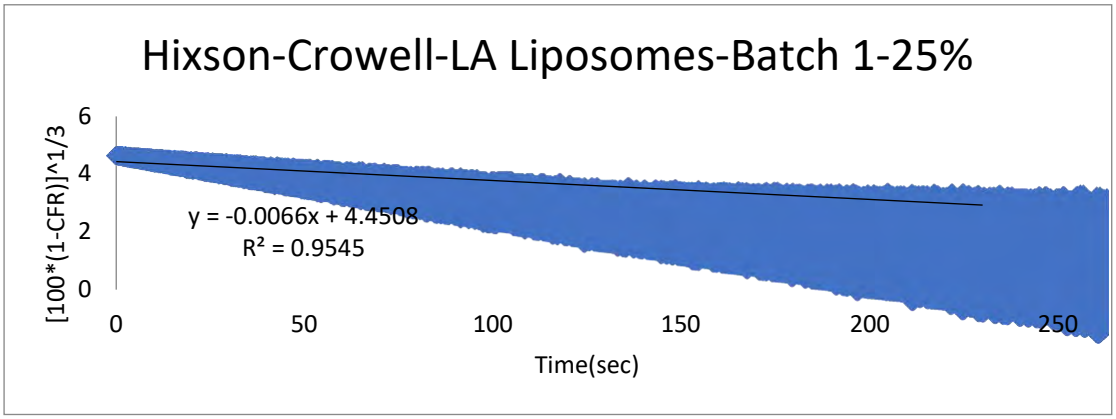

Figure 127: Hixson-Crowell model applied on LA liposomes for a power intensity of 9.85 mW/cm^2

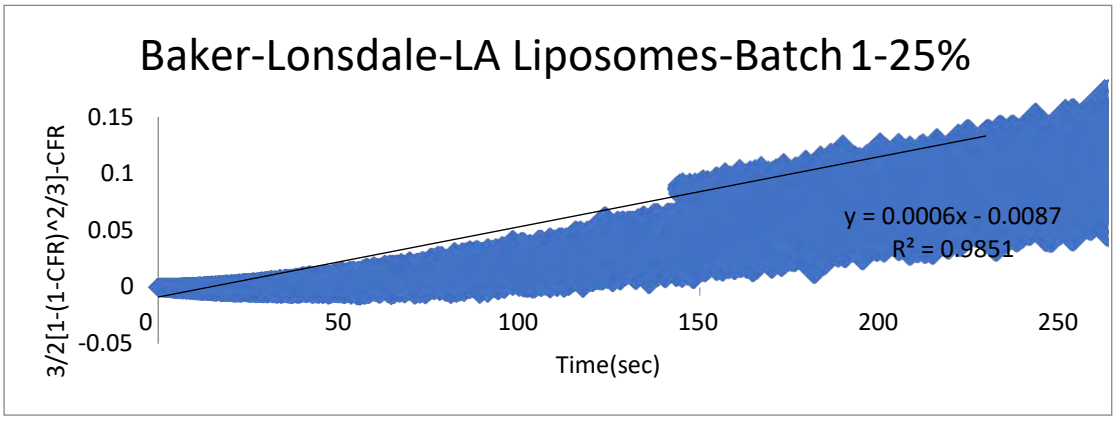

Figure 128: Baker-Lonsdale model applied on LA liposomes for a power intensity of 9.85 mW/cm^2

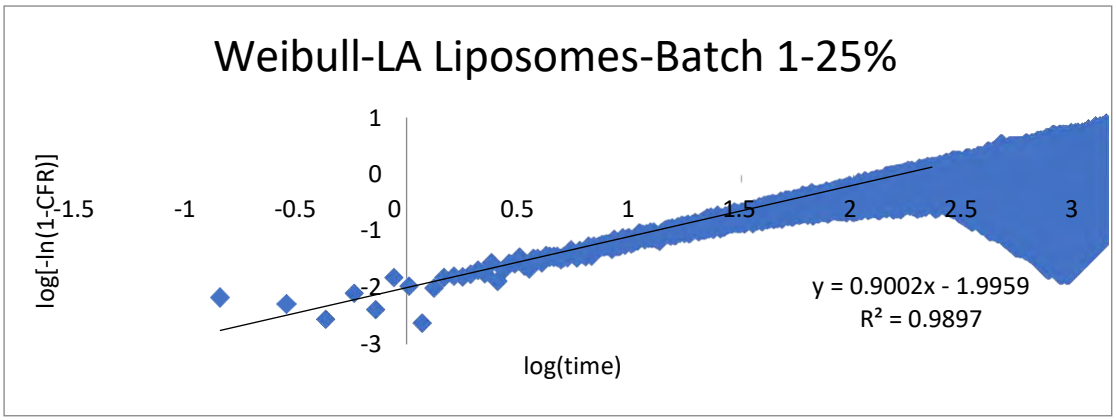

Figure 129:Weibull model applied on LA liposomes for a power intensity of 9.85 mW/cm^2

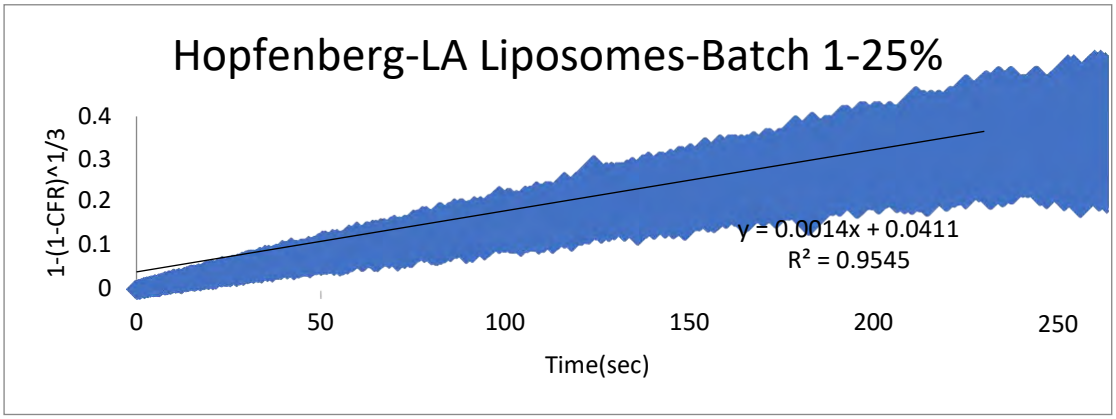

Figure 130: Hopfenberg model applied on LA liposomes for a power intensity of 9.85 mW/cm^2

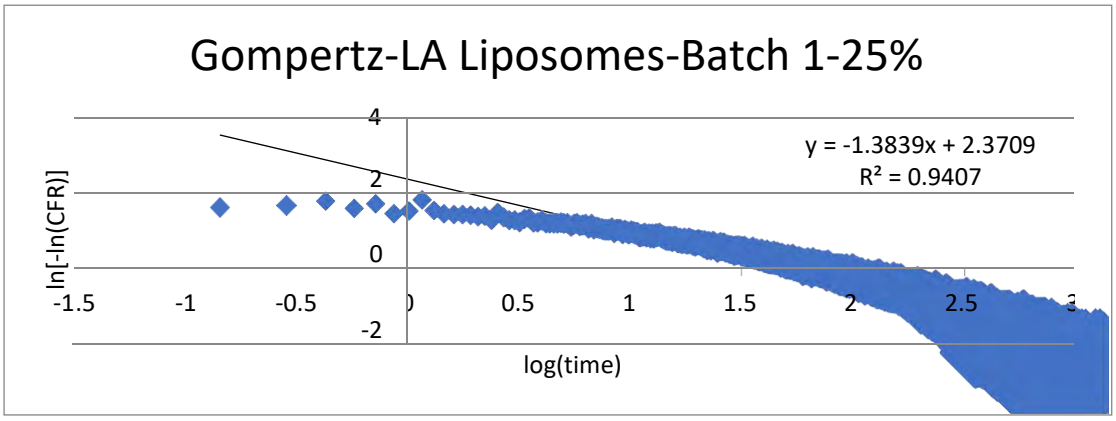

Figure 131: Gompertz model applied on LA liposomes for a power intensity of 9.85 mW/cm^2

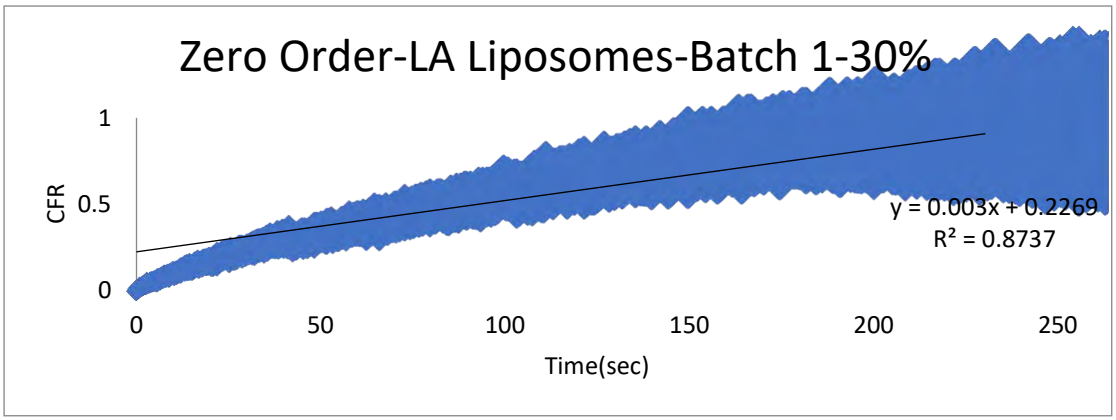

Figure 132:Zero order model applied on LA liposomes for a power intensity of 17.31mW/cm^2

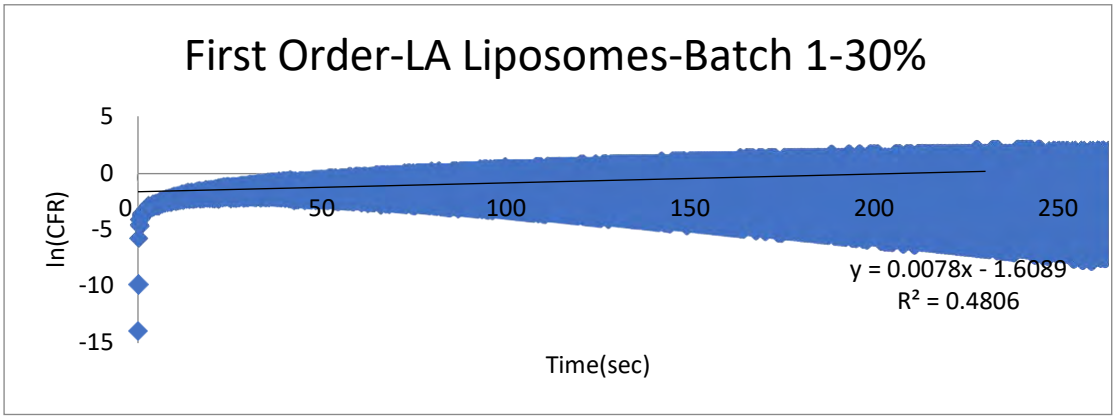

Figure 133:First order model applied on LA liposomes for a power intensity of 17.31mW/cm^2

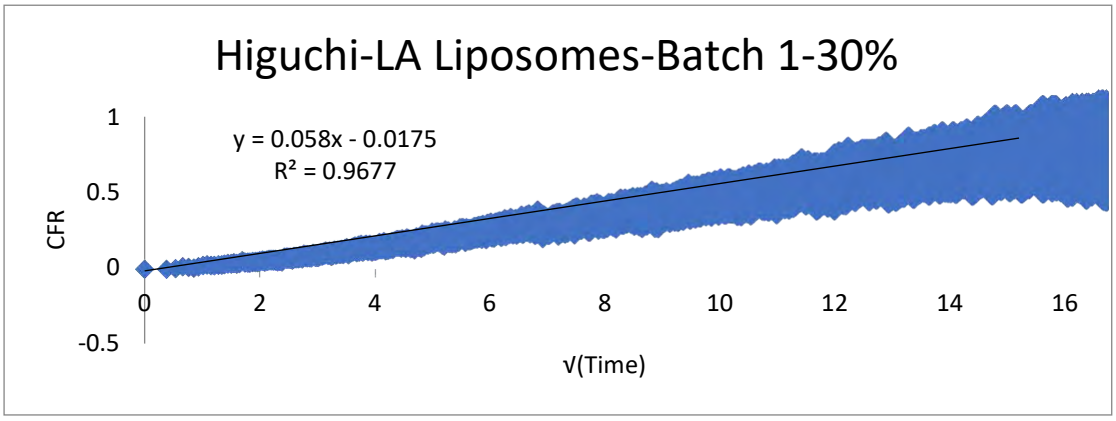

Figure 134:Higuchi model applied on LA liposomes for a power intensity of 17.31mW/cm^2

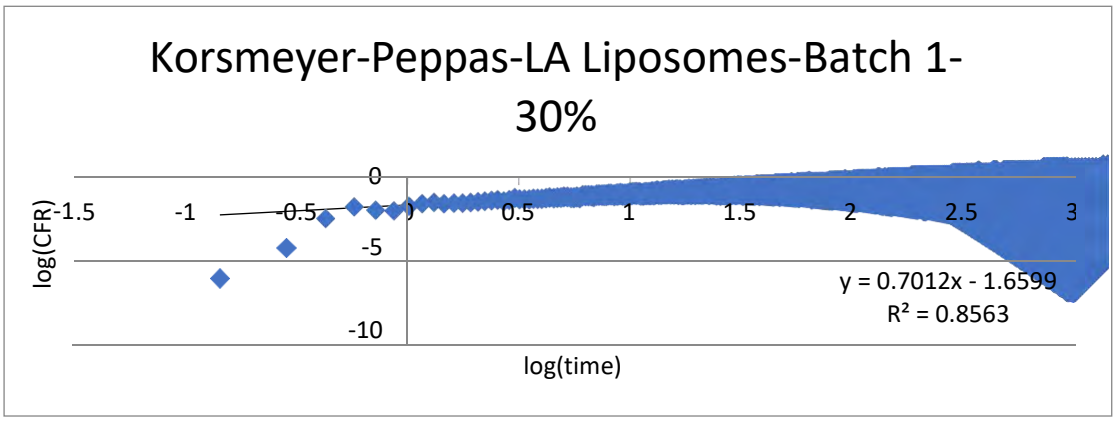

Figure 135:Korsmeyer-Peppas model applied on LA liposomes for a power intensity of 17.31mW/cm^2

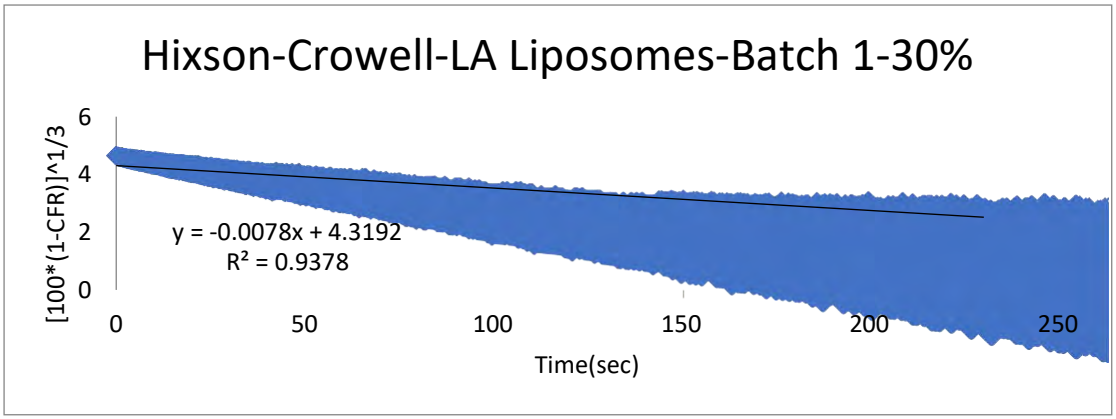

Figure 136:Hixson-Crowell model applied on LA liposomes for a power intensity of 17.31mW/cm^2

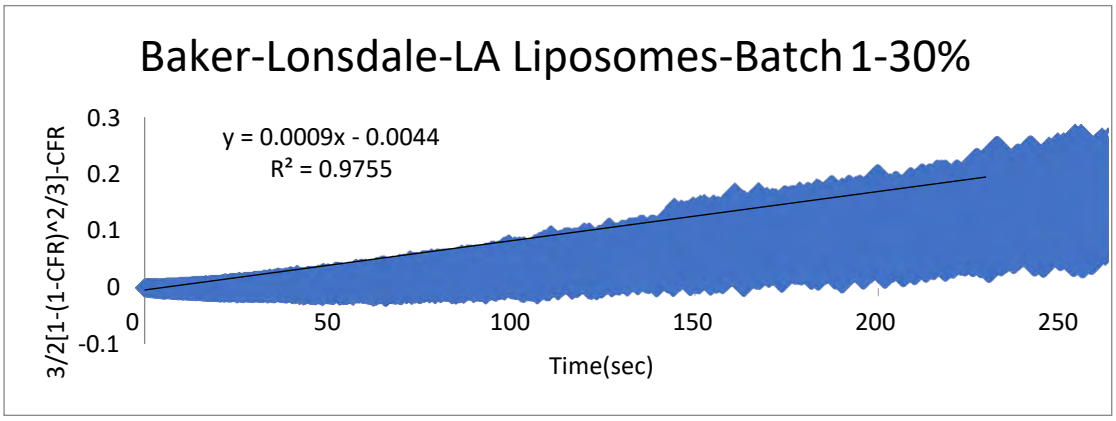

Figure 137:Baker-Lonsdale model applied on LA liposomes for a power intensity of 17.31mW/cm^2

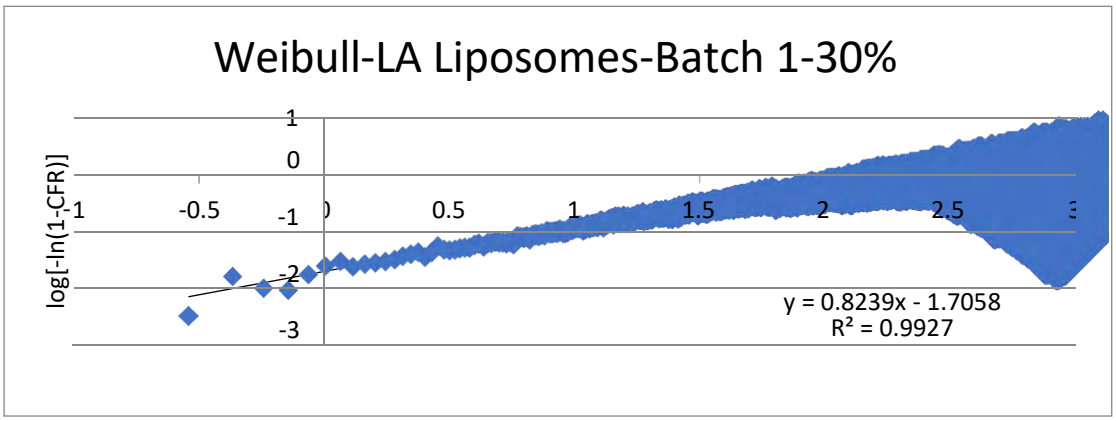

Figure 138:Weibull model applied on LA liposomes for a power intensity of 17.31mW/cm^2

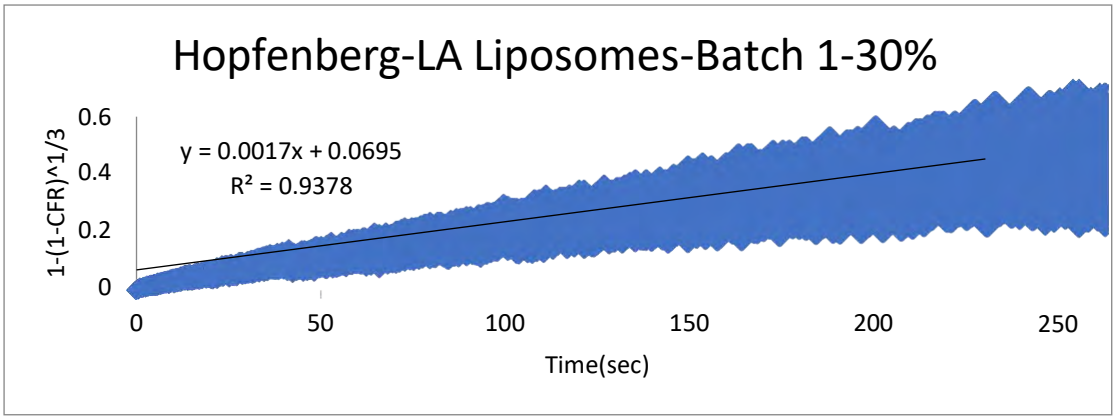

Figure 139:Hopfenberg model applied on LA liposomes for a power intensity of 17.31mW/cm^2

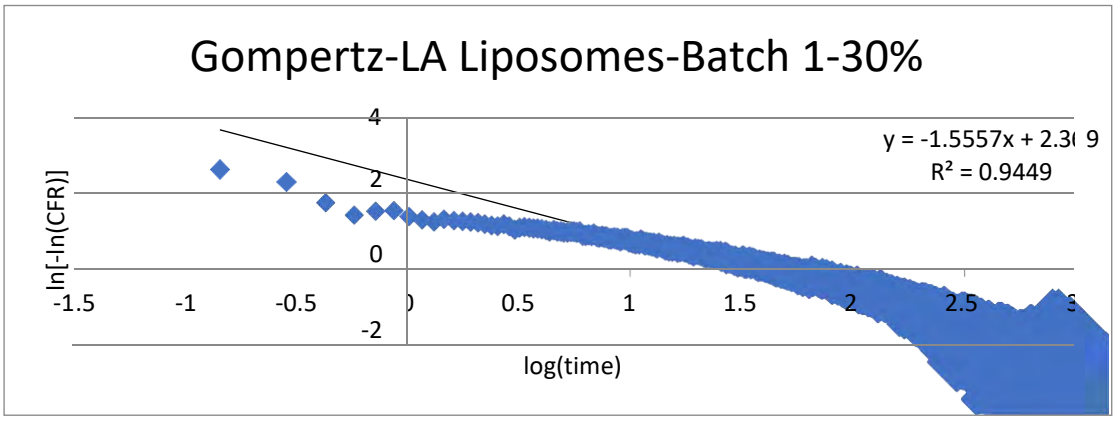

Figure 140:Gompertz model applied on LA liposomes for a power intensity of 17.31mW/cm^2

Appendix E: Plots of kinetic modeling for LA Liposomes Batch 2

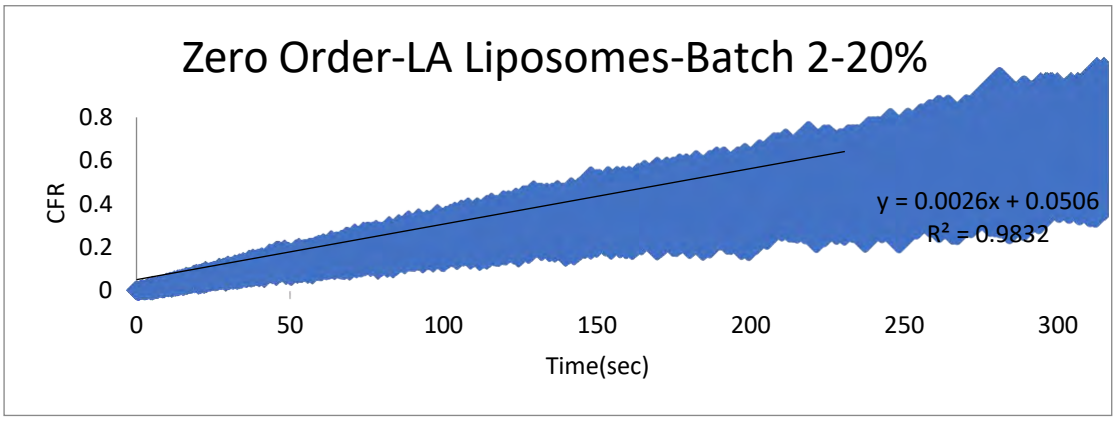

Figure 141: Zero Order model applied on LA liposomes for a power intensity of 7.46 mW/cm^2

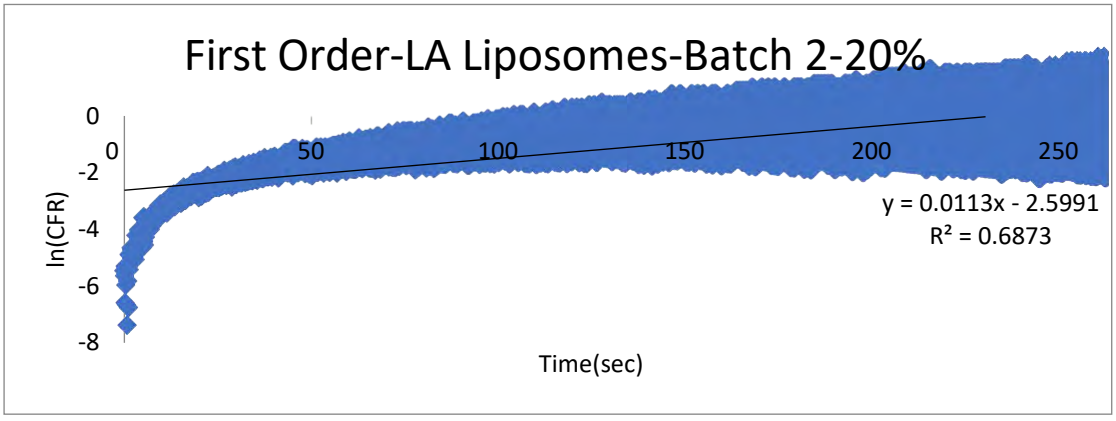

Figure 142:First Order model applied on LA liposomes for a power intensity of 7.46 mW/cm^2

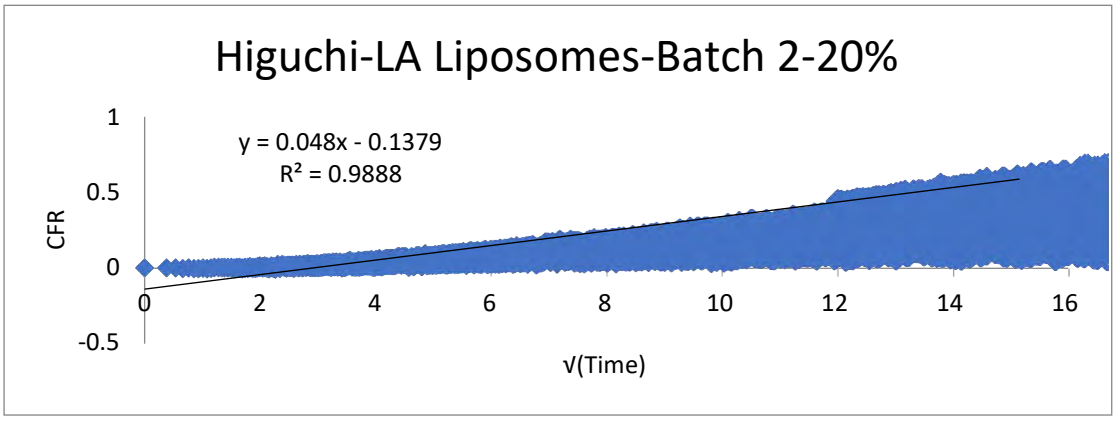

Figure 143:Higuchi model applied on LA liposomes for a power intensity of 7.46 mW/cm^2

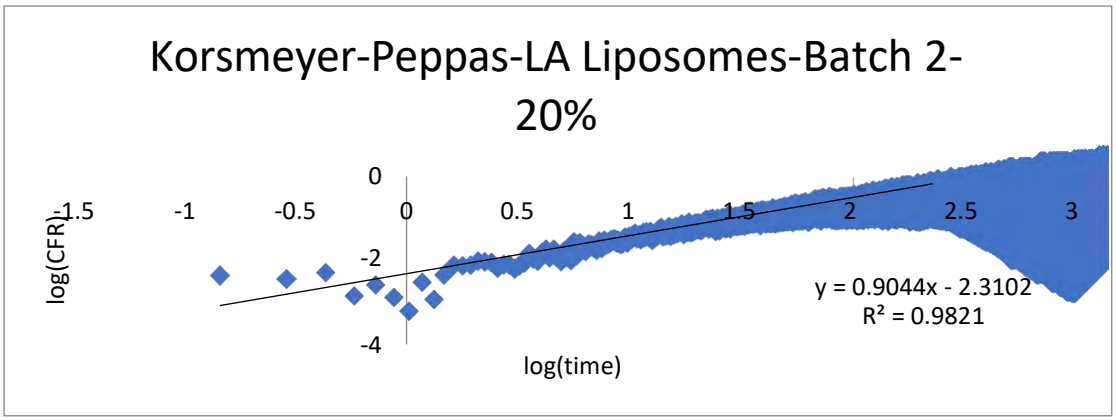

Figure 144: Korsmeyer-Peppas model applied on LA liposomes for a power intensity of 7.46 mW/cm^2

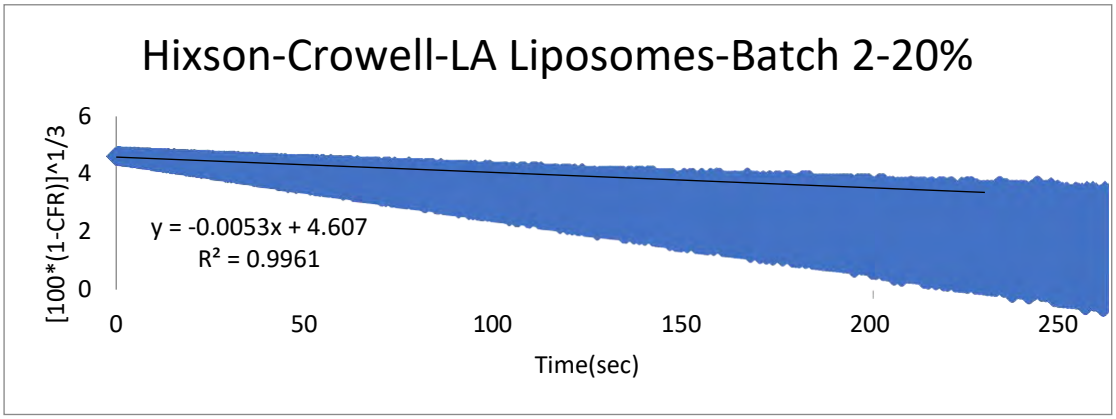

Figure 145:Hixson-Crowell model applied on LA liposomes for a power intensity of 7.46 mW/cm^2

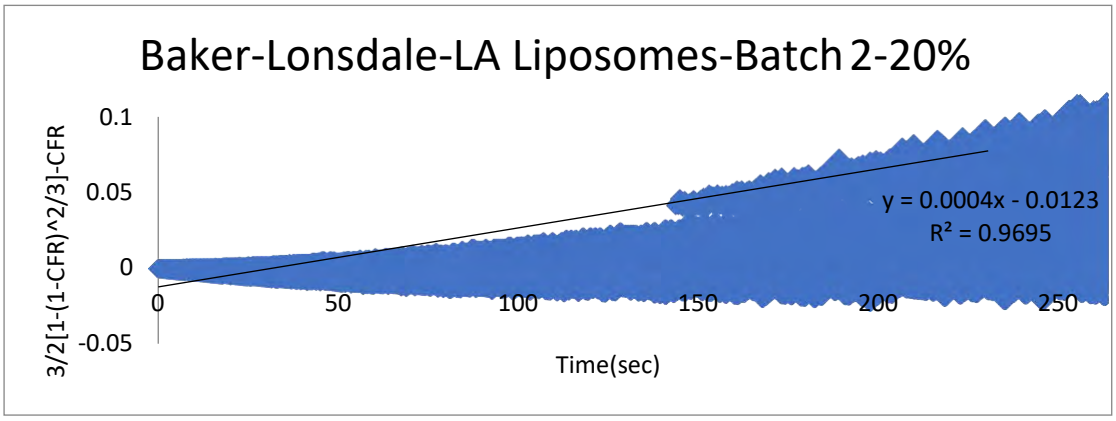

Figure 146:Baker-Lonsdale model applied on LA liposomes for a power intensity of 7.46 mW/cm^2

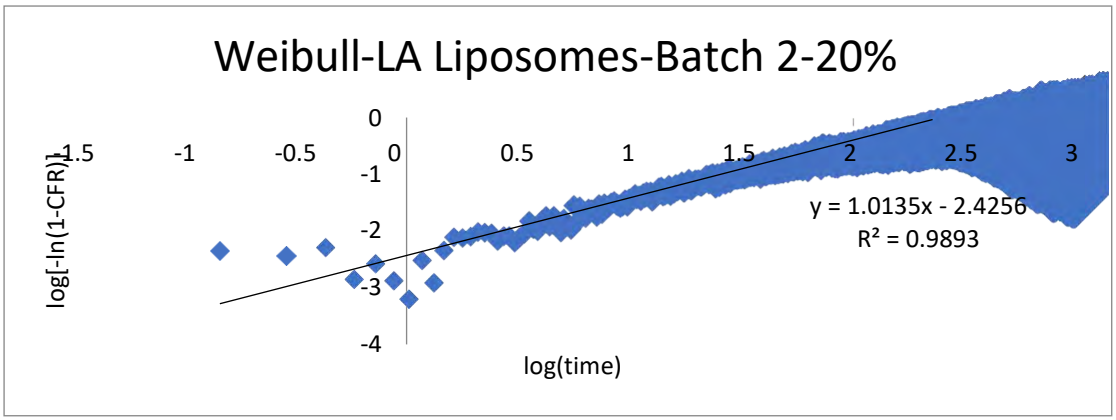

Figure 147:Weibull model applied on LA liposomes for a power intensity of 7.46 mW/cm^2

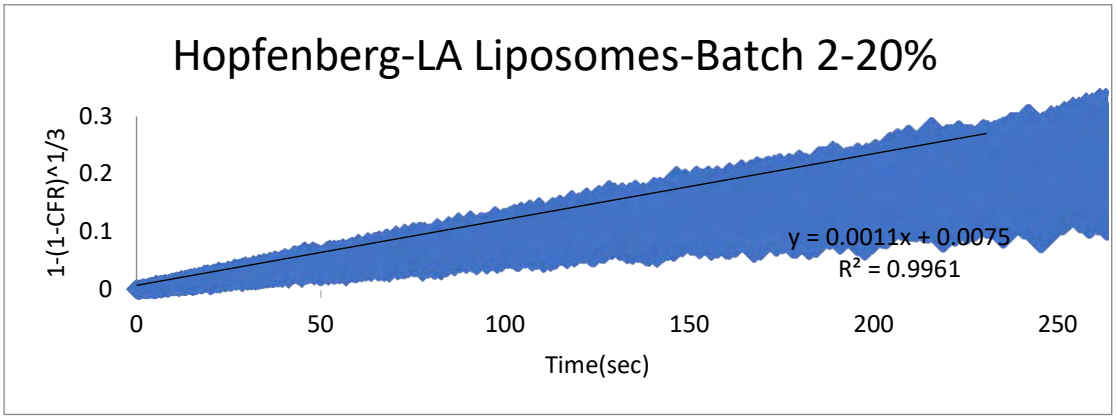

Figure 148:Hopfenberg model applied on LA liposomes for a power intensity of 7.46 mW/cm^2

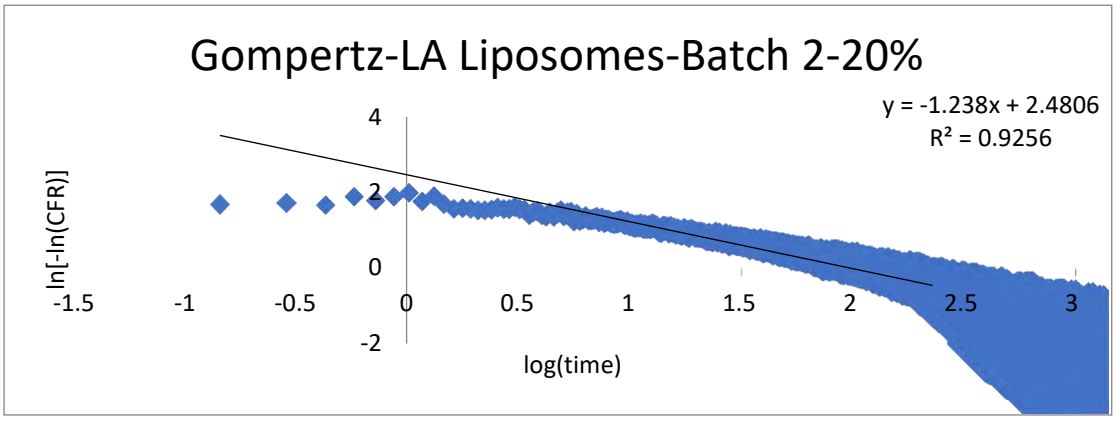

Figure 149: Gompertz model applied on LA liposomes for a power intensity of 7.46 mW/cm^2

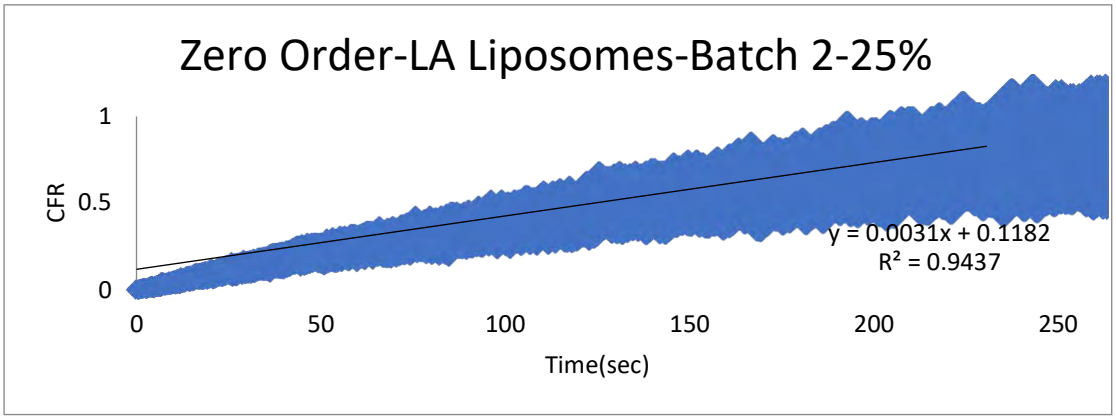

Figure 150:Zero Order model applied on LA liposomes for a power intensity of 9.85 mW/cm^2

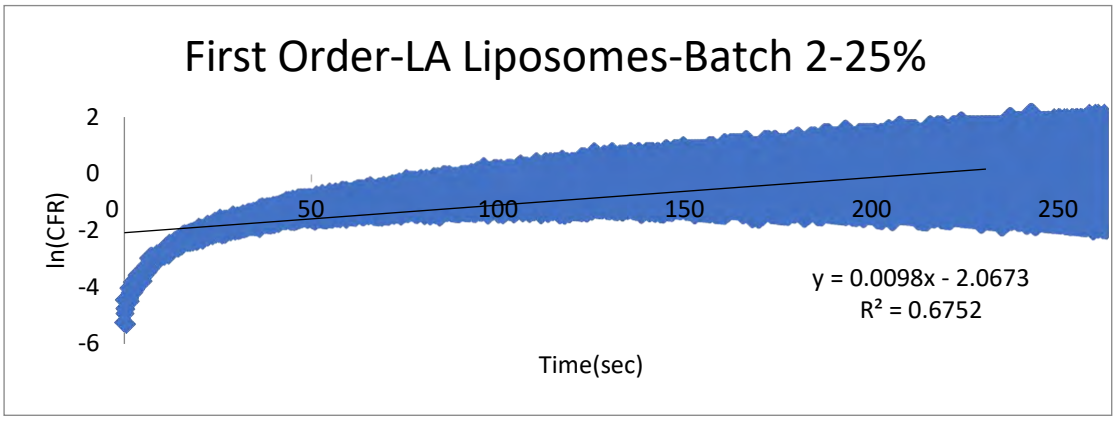

Figure 151:First Order model applied on LA liposomes for a power intensity of 9.85 mW/cm^2

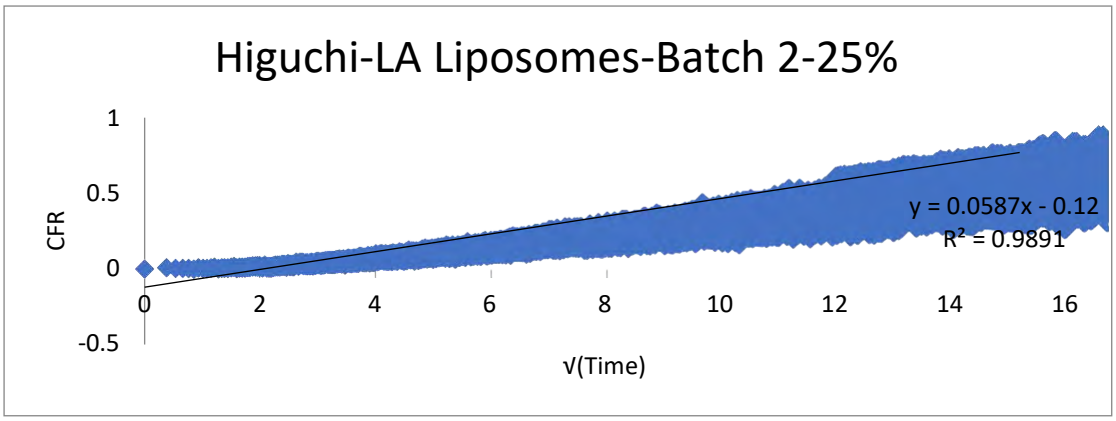

Figure 152:Higuchi model applied on LA liposomes for a power intensity of 9.85 mW/cm^2

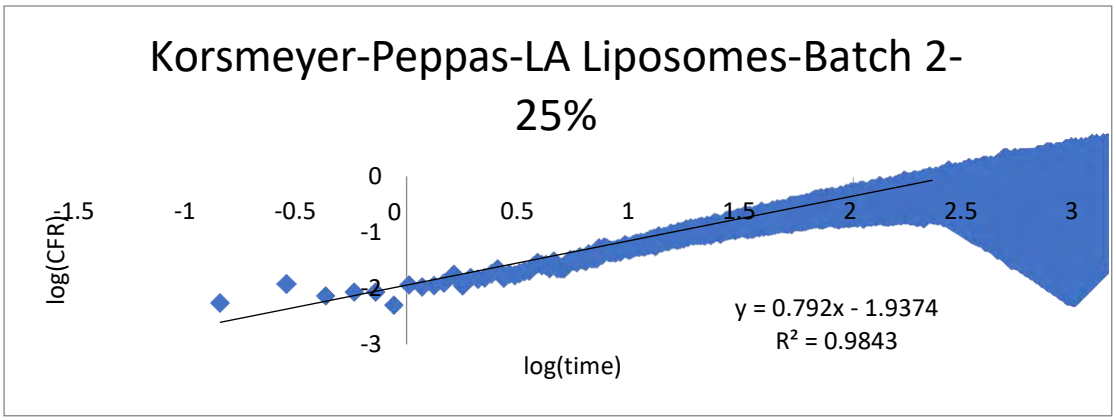

Figure 153: Korsmeyer-Peppas model applied on LA liposomes for a power intensity of 9.85 mW/cm^2

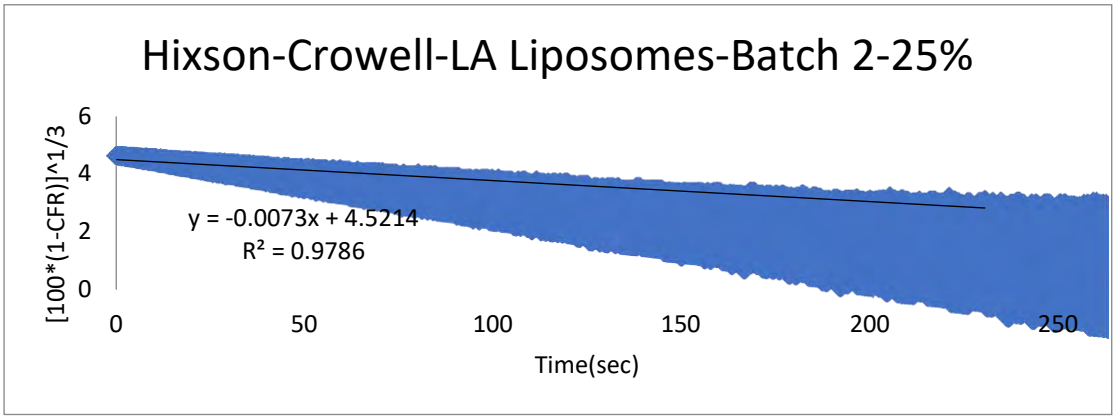

Figure 154: Hixson-Crowell model applied on LA liposomes for a power intensity of 9.85 mW/cm^2

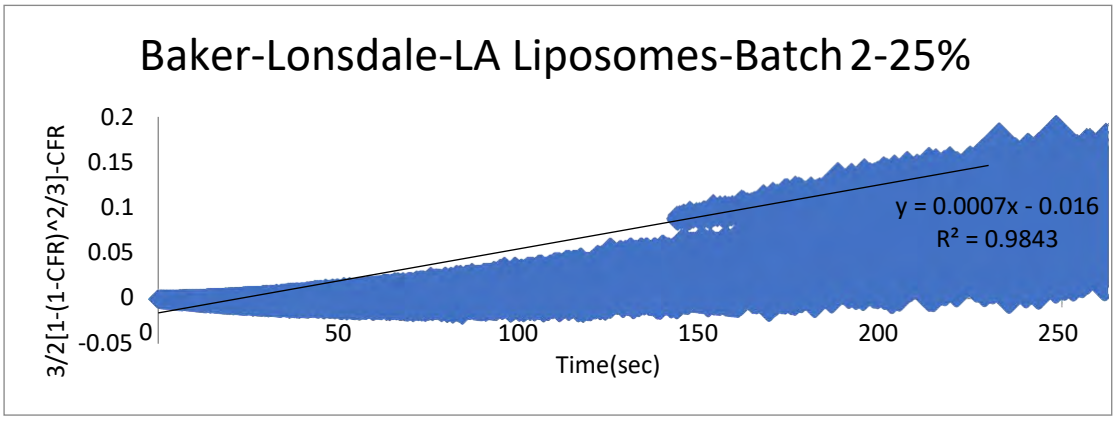

Figure 155:Baker-Lonsdale model applied on LA liposomes for a power intensity of 9.85 mW/cm$_2$

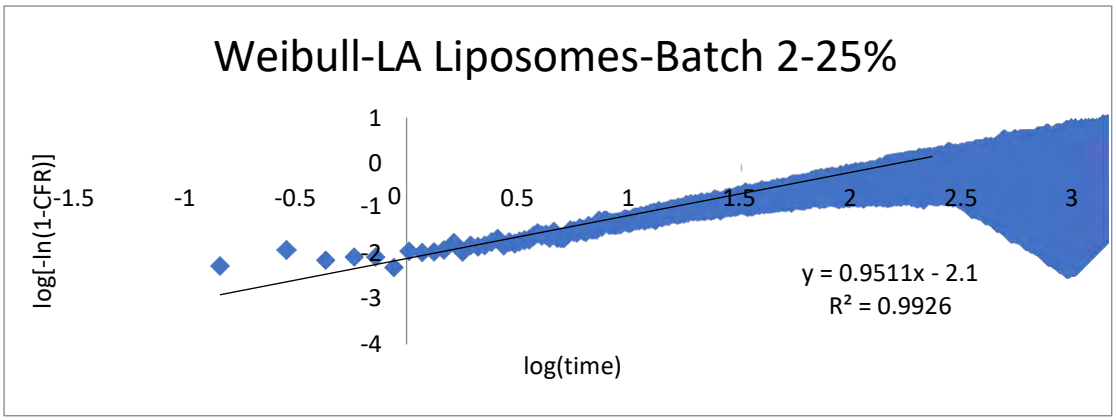

Figure 156:Weibull model applied on LA liposomes for a power intensity of 9.85 mW/cm^2

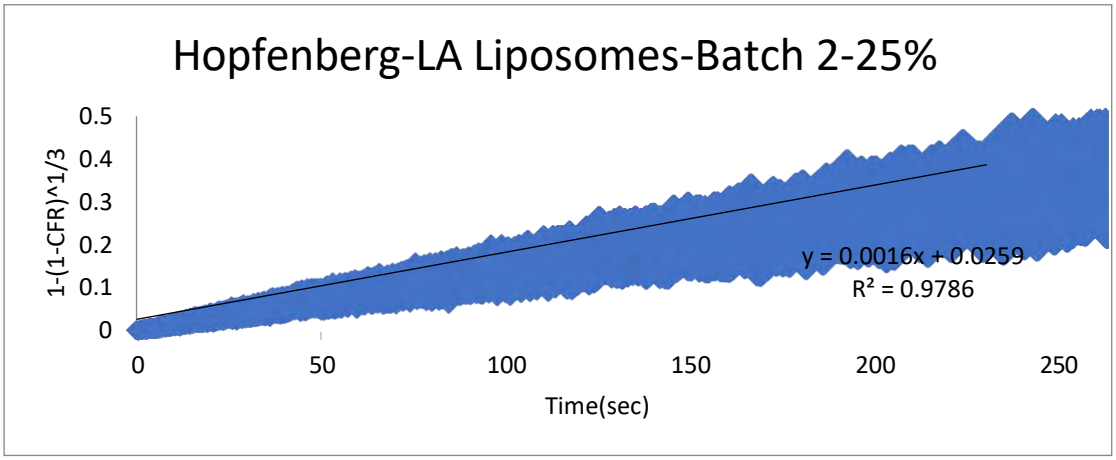

Figure 157:Hopfenberg model applied on LA liposomes for a power intensity of 9.85 mW/cm^2

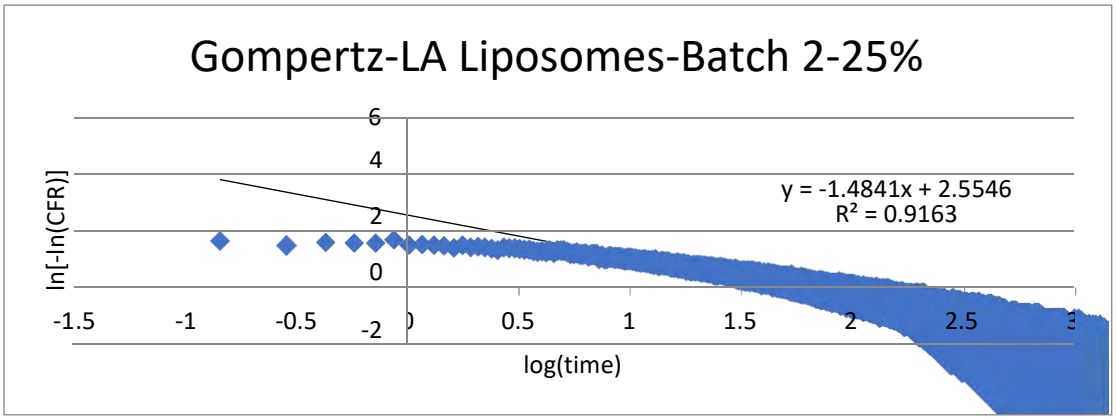

Figure 158: Gompertz model applied on LA liposomes for a power intensity of 9.85 mW/cm^2

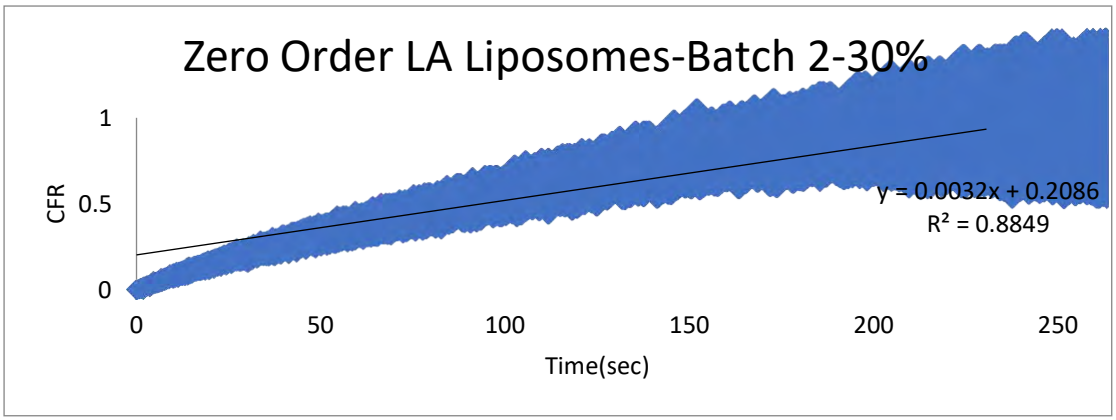

Figure 159:Zero Order model applied on LA liposomes for a power intensity of 17.31 mW/cm^2

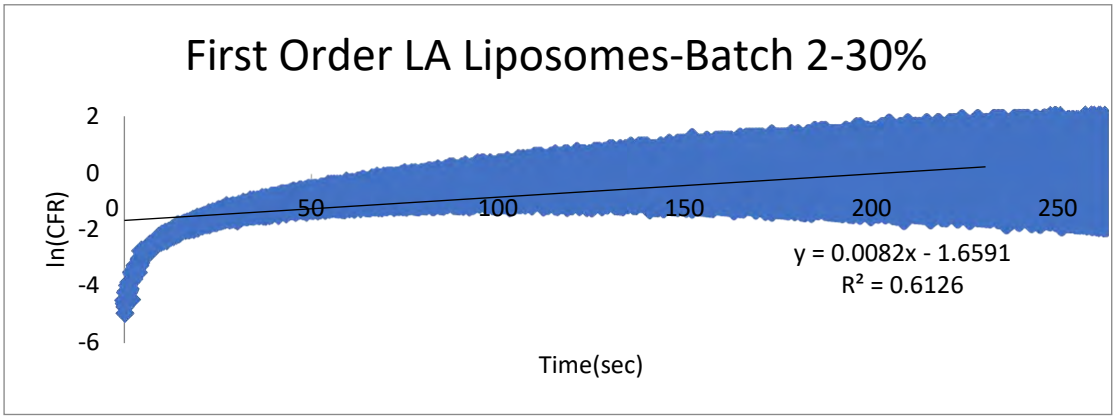

Figure 160:First Order model applied on LA liposomes for a power intensity of 17.31 mW/cm^2

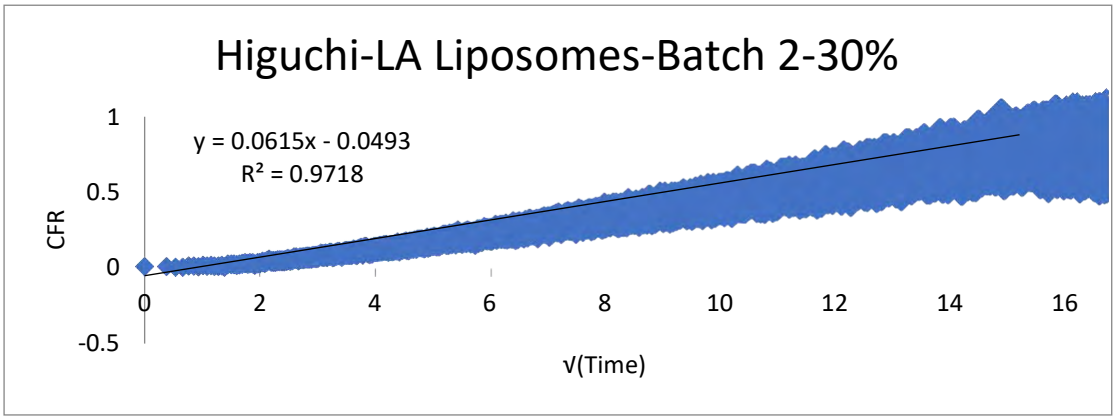

Figure 161: Higuchi model applied on LA liposomes for a power intensity of 17.31 mW/cm^2

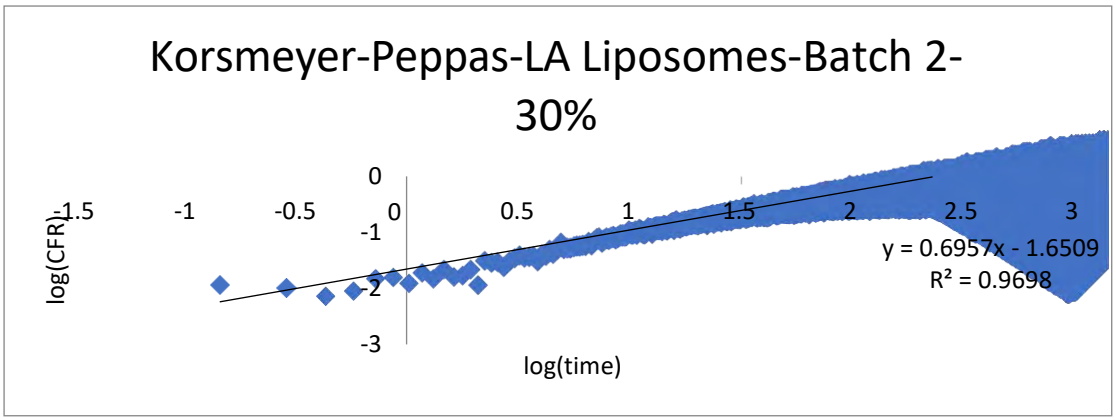

Figure 162:Korsmeyer-Peppas model applied on LA liposomes for a power intensity of 17.31 mW/cm^2

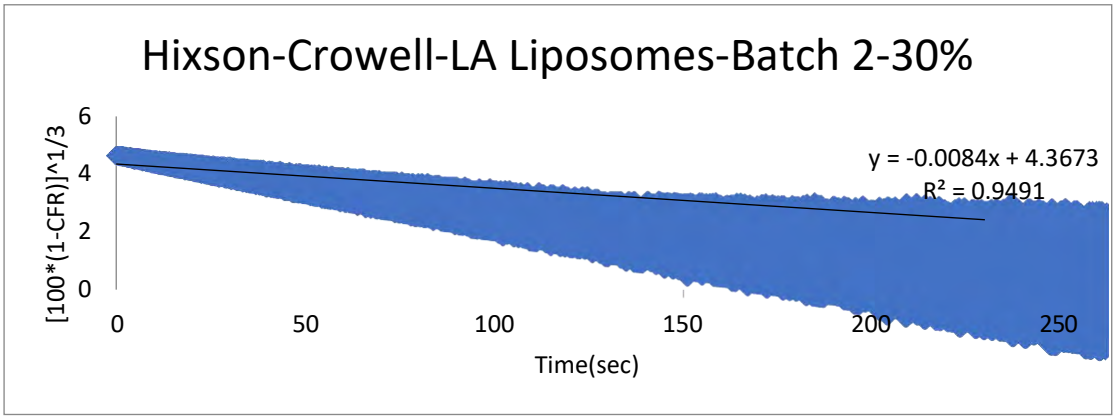

Figure 163: Hixson-Crowell model applied on LA liposomes for a power intensity of 17.31 mW/cm^2

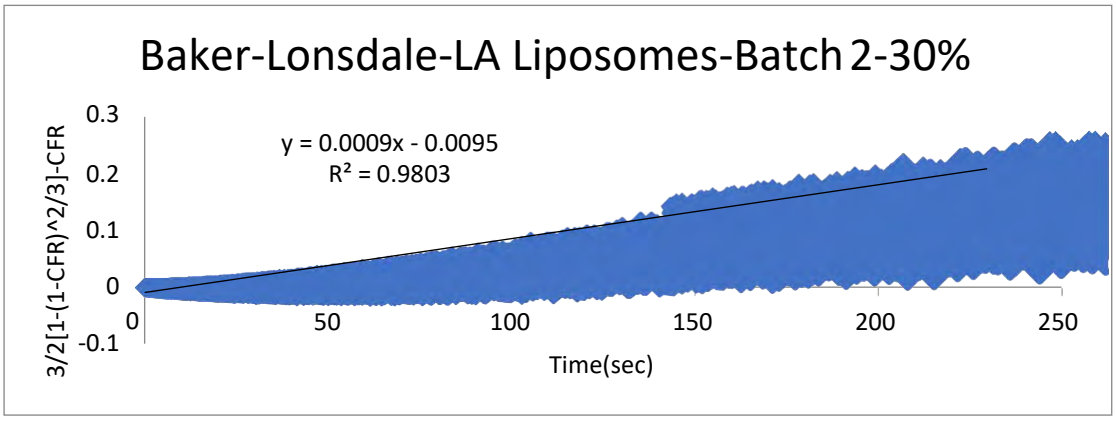

Figure 164: Baker Lonsdale model applied on LA liposomes for a power intensity of 17.31 mW/cm^2

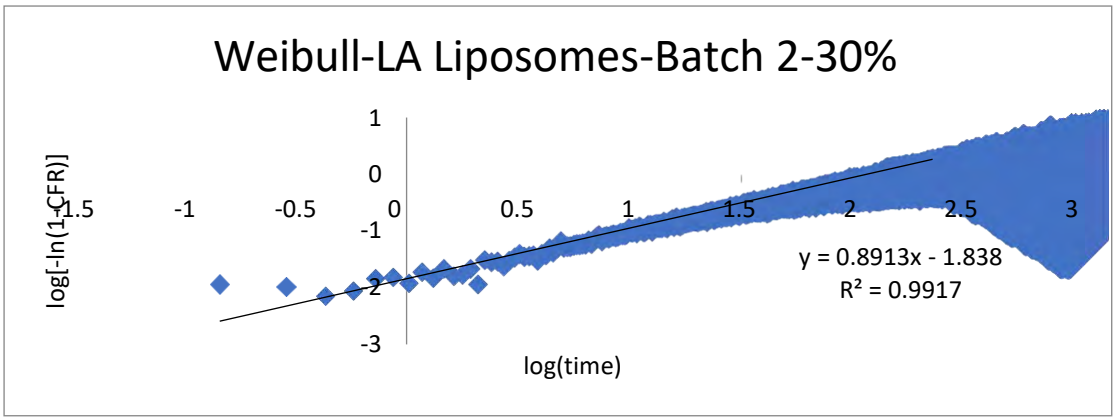

Figure 165: Weibull model applied on LA liposomes for a power intensity of 17.31 mW/cm^2

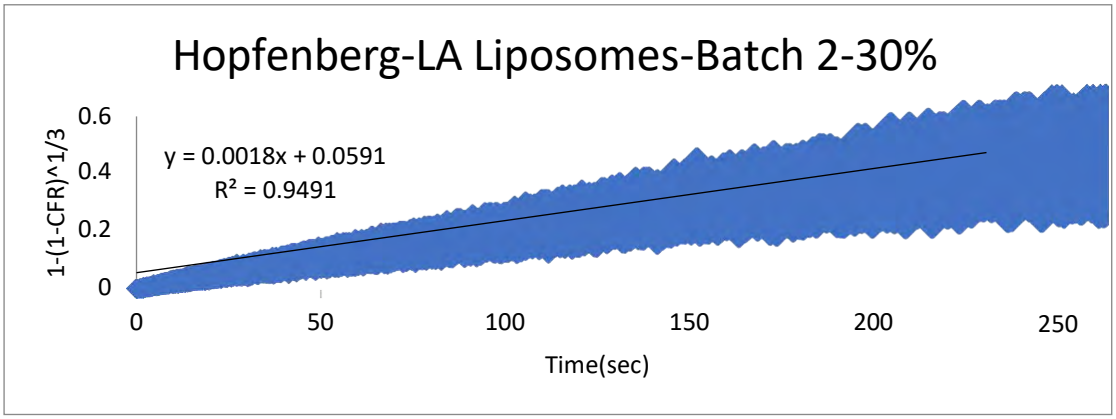

Figure 166:Hopfenberg model applied on LA liposomes for a power intensity of 17.31 mW/cm^2

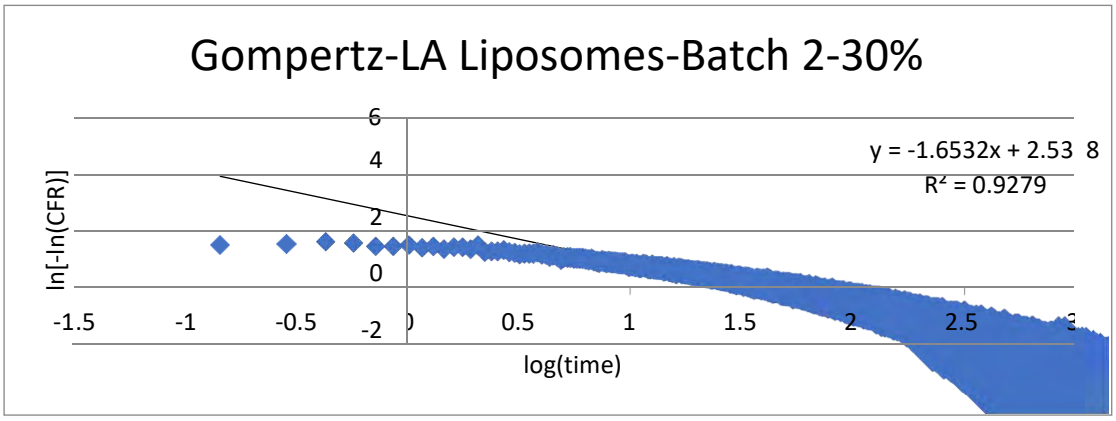

Figure 167: Gompertz model applied on LA liposomes for a power intensity of 17.31 mW/cm^2

Appendix F: Plots of kinetic modeling for LA Liposomes Batch 3

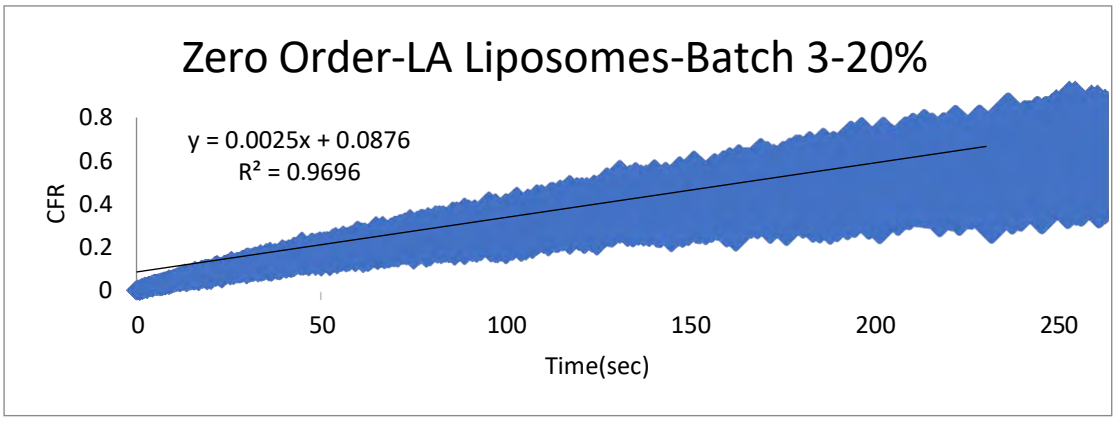

Figure 168:Zero Order model applied on LA liposomes for a power intensity of 7.46 mW/cm^2

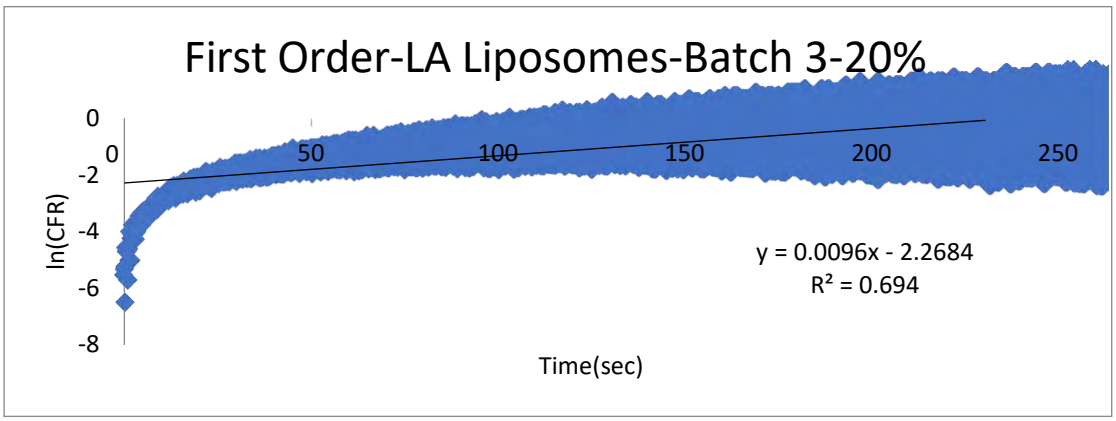

Figure 169:First Order model applied on LA liposomes for a power intensity of 7.46 mW/cm^2

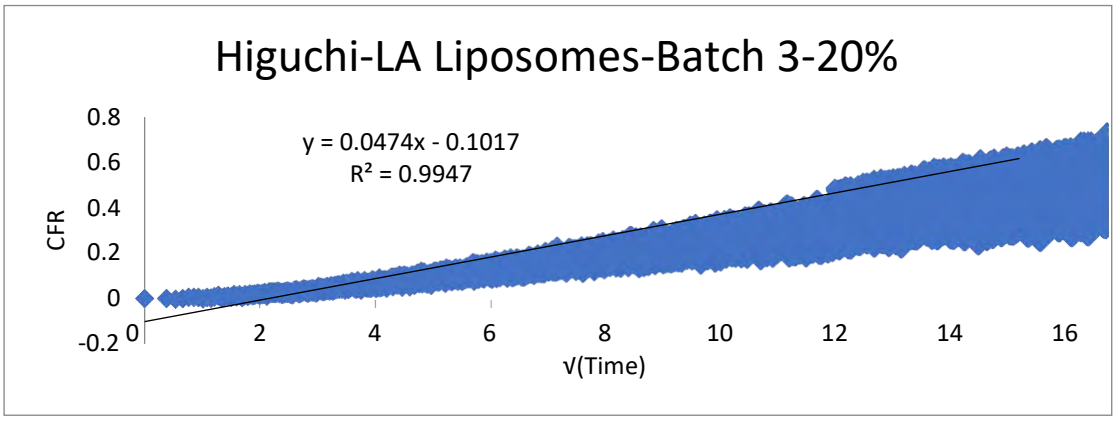

Figure 170:Higuchi model applied on LA liposomes for a power intensity of 7.46 mW/cm^2

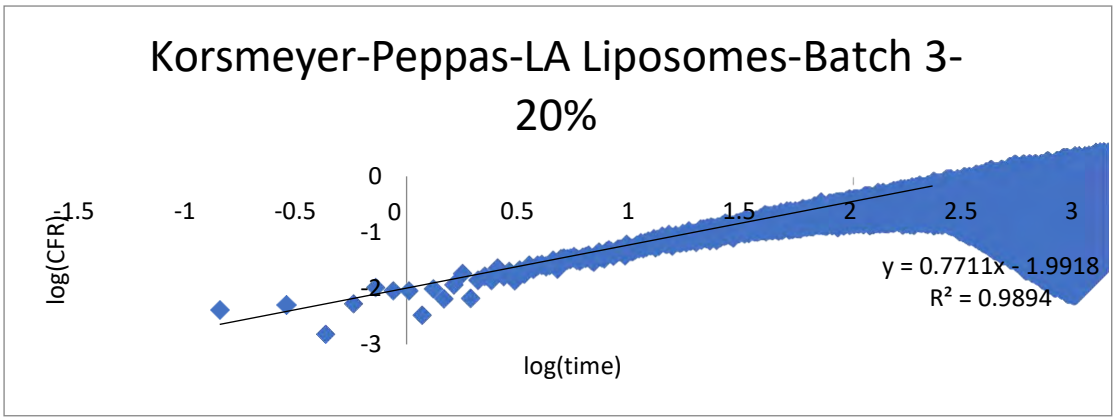

Figure 171: Korsmeyer-Peppas model applied on LA liposomes for a power intensity of 7.46 mW/cm^2

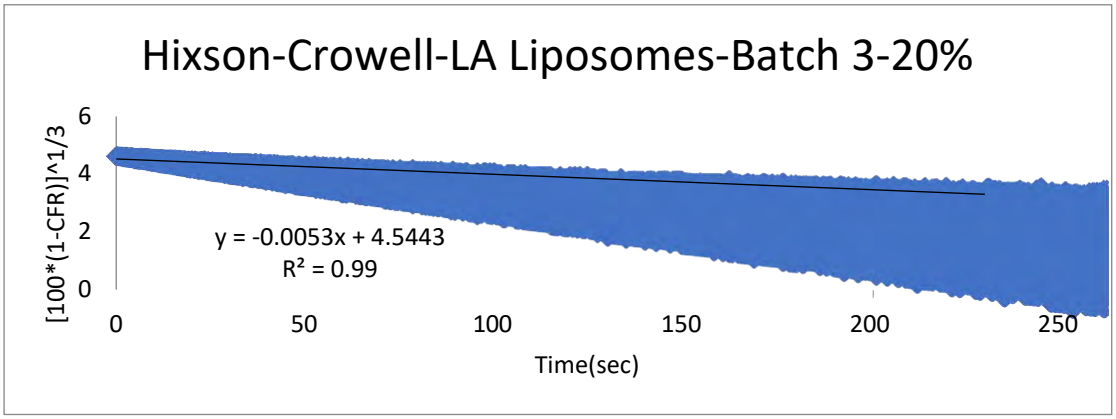

Figure 172:Hixson Crowell model applied on LA liposomes for a power intensity of 7.46 mW/cm^2

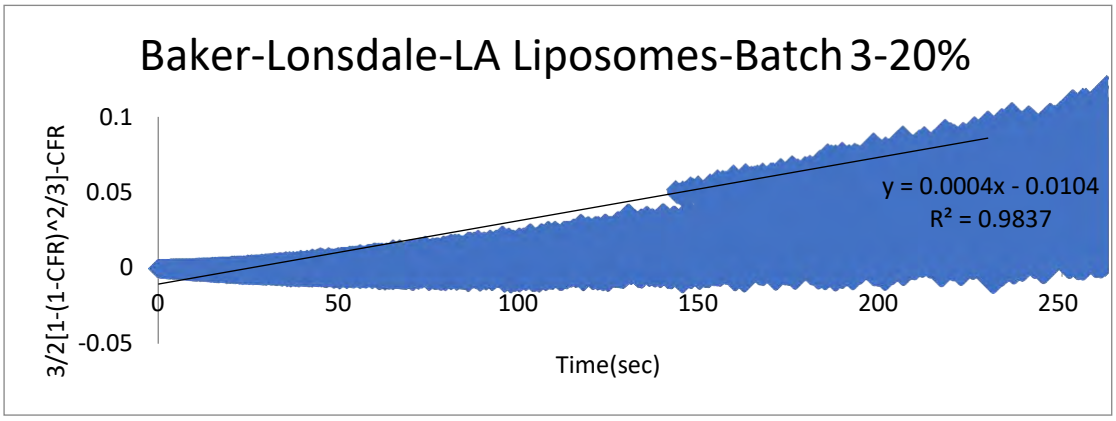

Figure 173: Baker-Lonsdale model applied on LA liposomes for a power intensity of 7.46 mW/cm^2

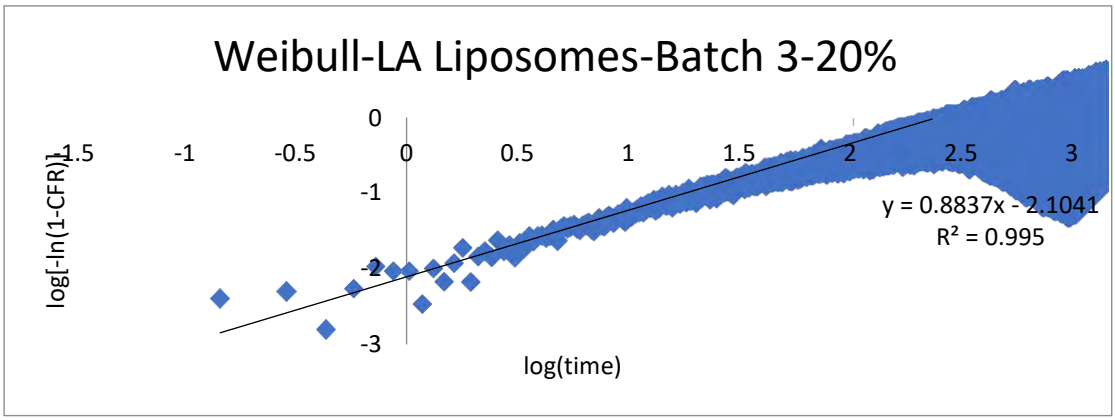

Figure 174:Weibull model applied on LA liposomes for a power intensity of 7.46 mW/cm^2

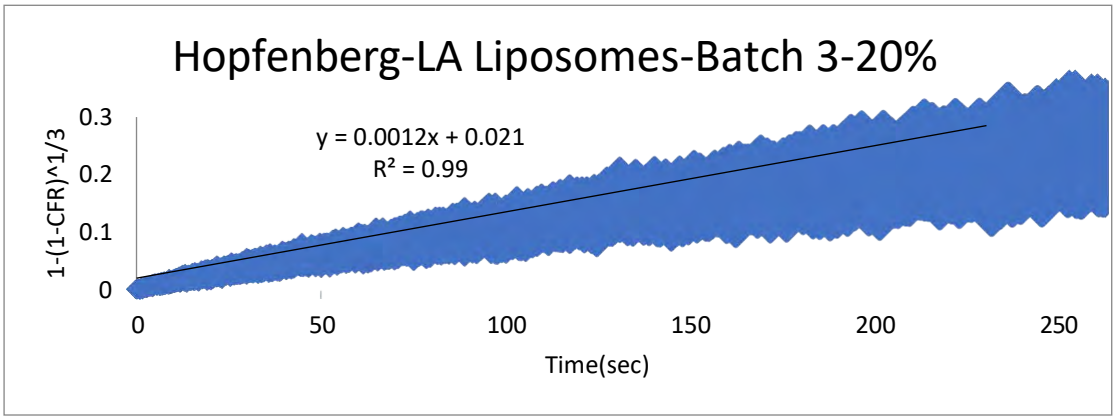

Figure 175:Hopfenberg model applied on LA liposomes for a power intensity of 7.46 mW/cm^2

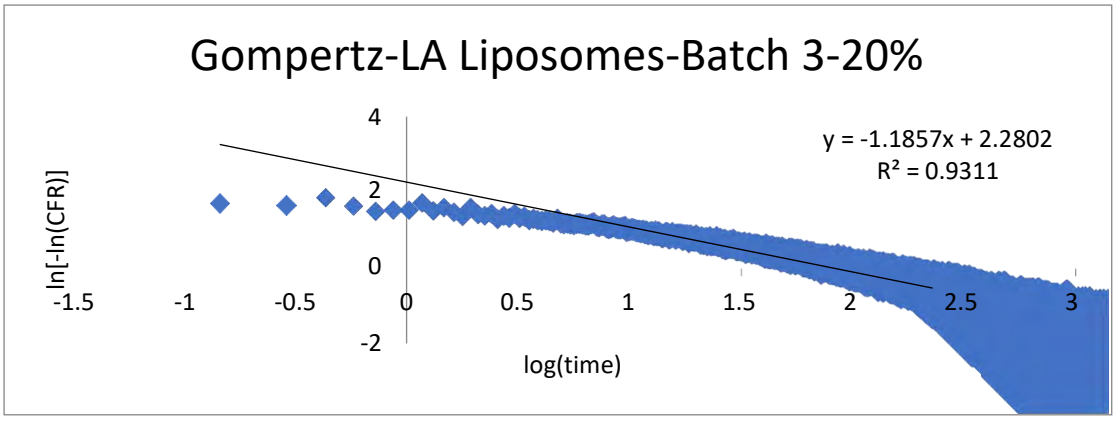

Figure 176: Gompertz model applied on LA liposomes for a power intensity of 7.46 mW/cm^2

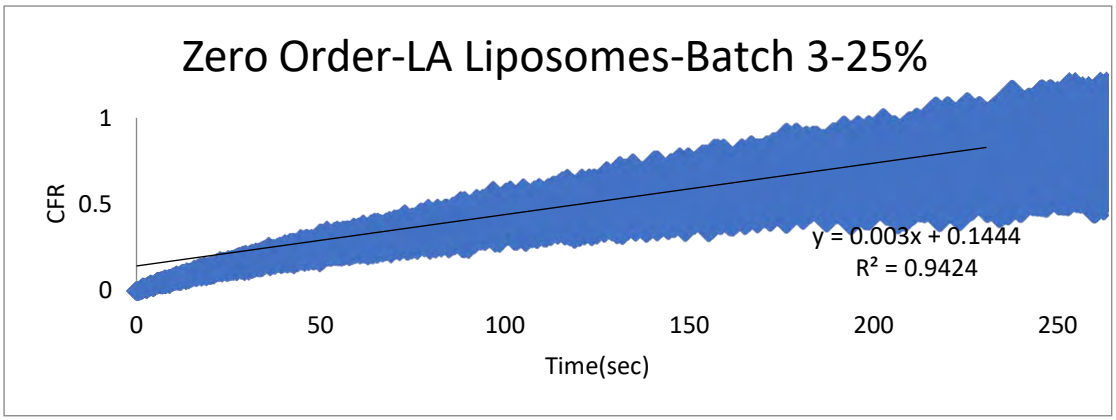

Figure 177:Zero order model applied on LA liposomes for a power intensity of 9.85 mW/cm^2

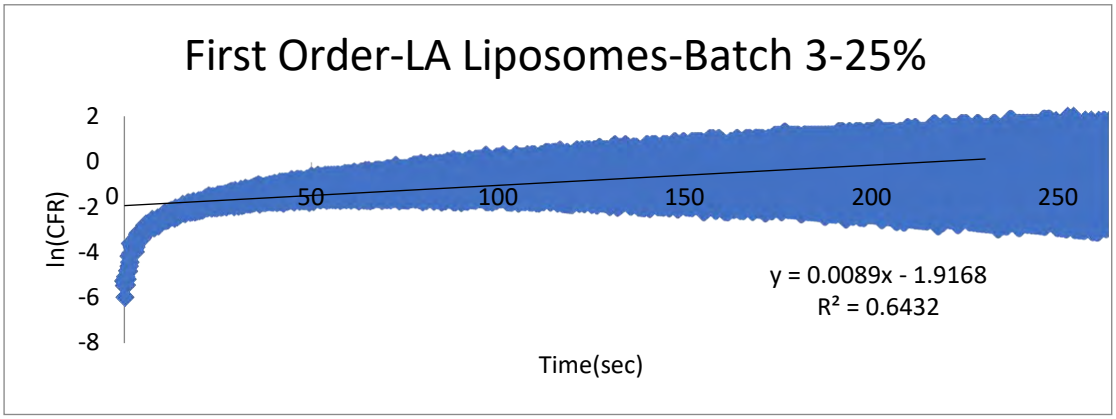

Figure 178:First Order model applied on LA liposomes for a power intensity of 9.85 mW/cm^2

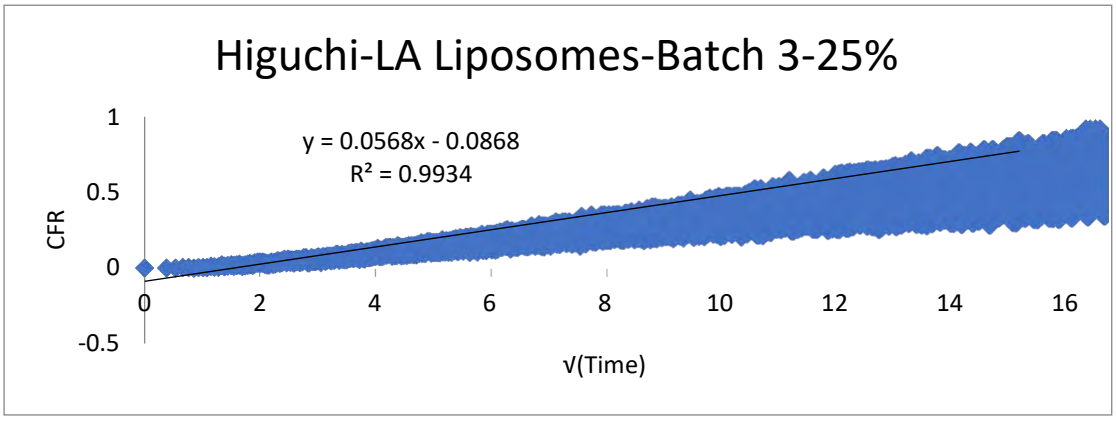

Figure 179:Higuchi model applied on LA liposomes for a power intensity of 9.85 mW/cm^2

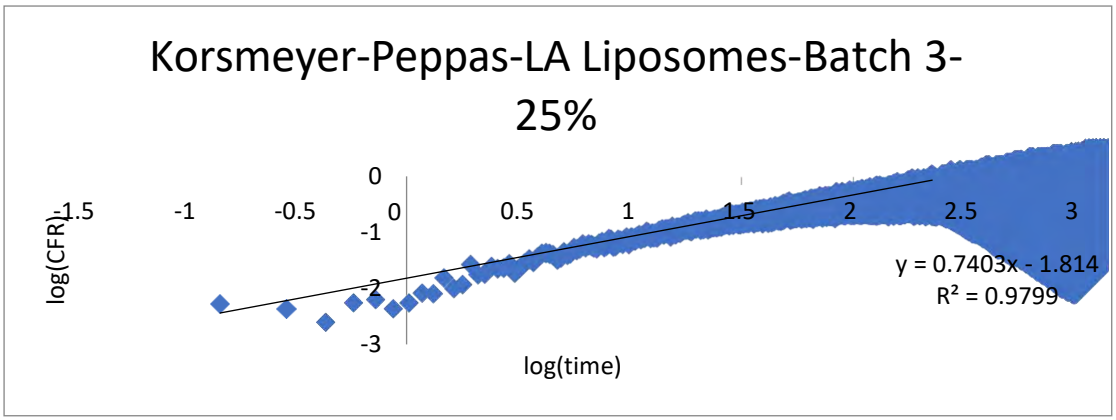

Figure 180:Korsmeyer-Peppas model applied on LA liposomes for a power intensity of 9.85 mW/cm^2

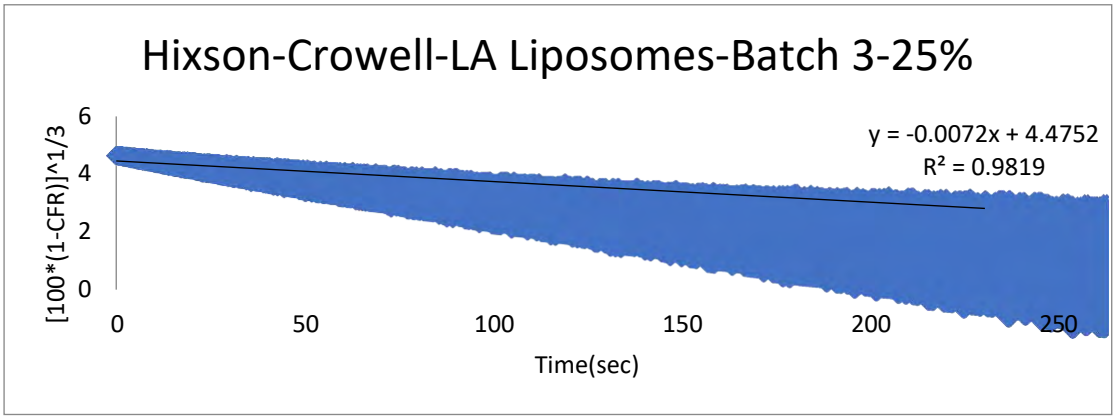

Figure 181:Hixson model applied on LA liposomes for a power intensity of 9.85 mW/cm^2

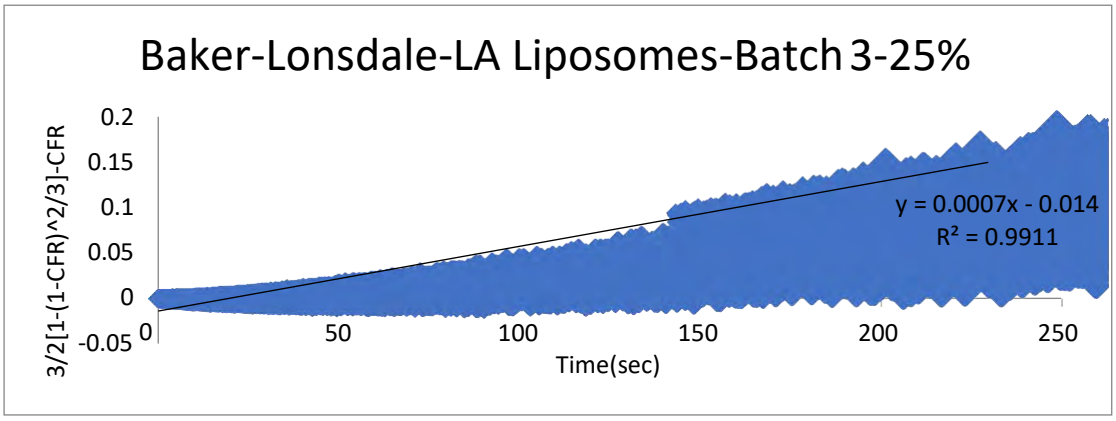

Figure 182:Baker-Lonsdale model applied on LA liposomes for a power intensity of 9.85 mW/cm^2

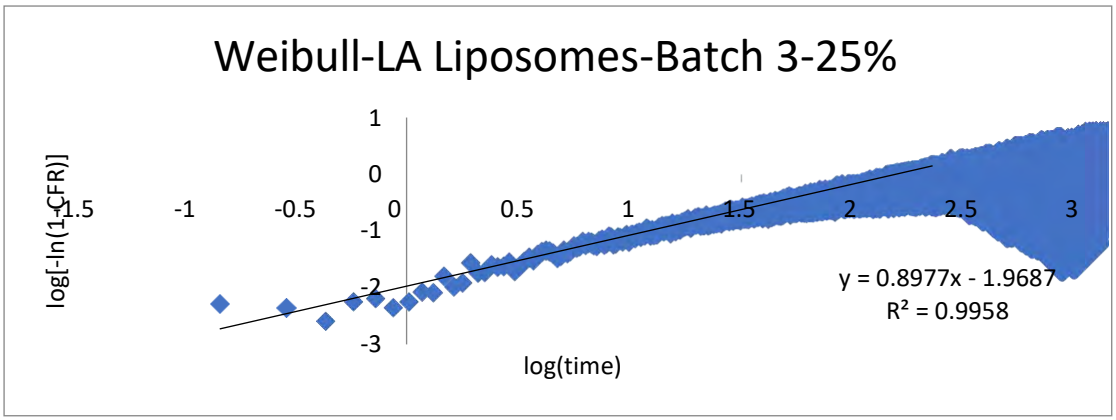

Figure 183:Weibull model applied on LA liposomes for a power intensity of 9.85 mW/cm^2

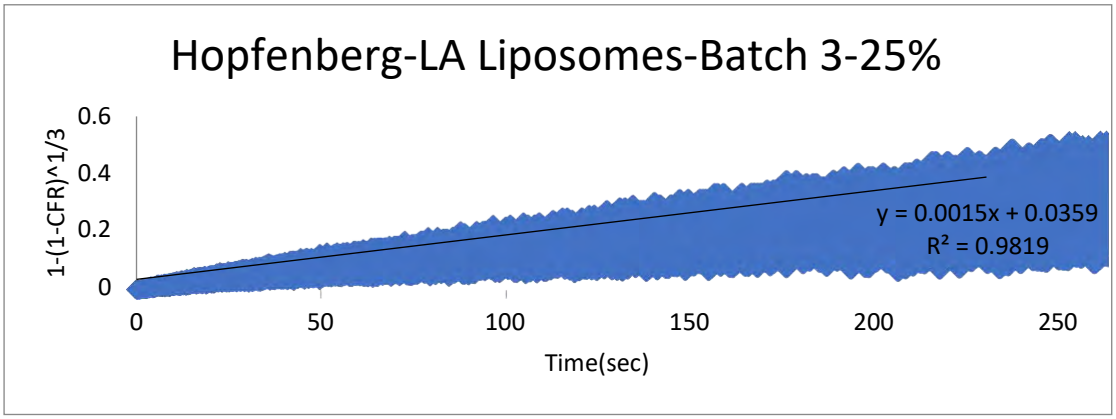

Figure 184:Hopfenberg model applied on LA liposomes for a power intensity of 9.85 mW/cm^2

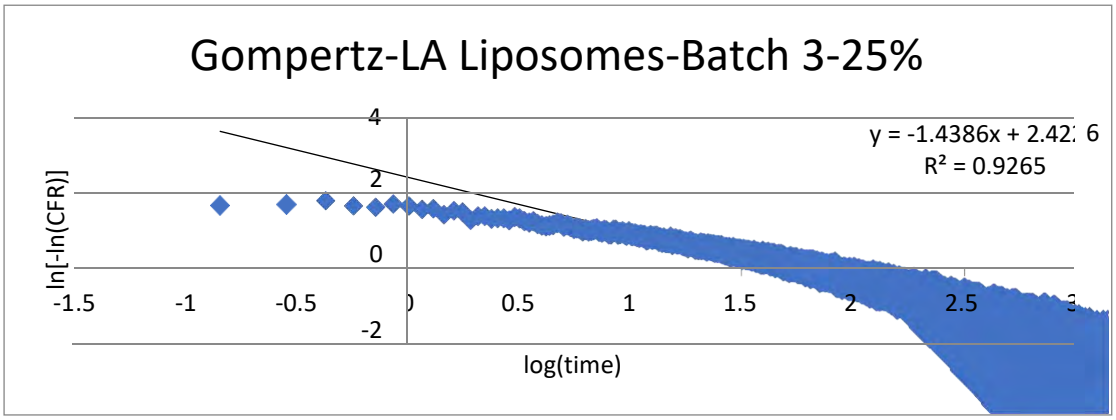

Figure 185:Gompertz model applied on LA liposomes for a power intensity of 9.85 mW/cm^2

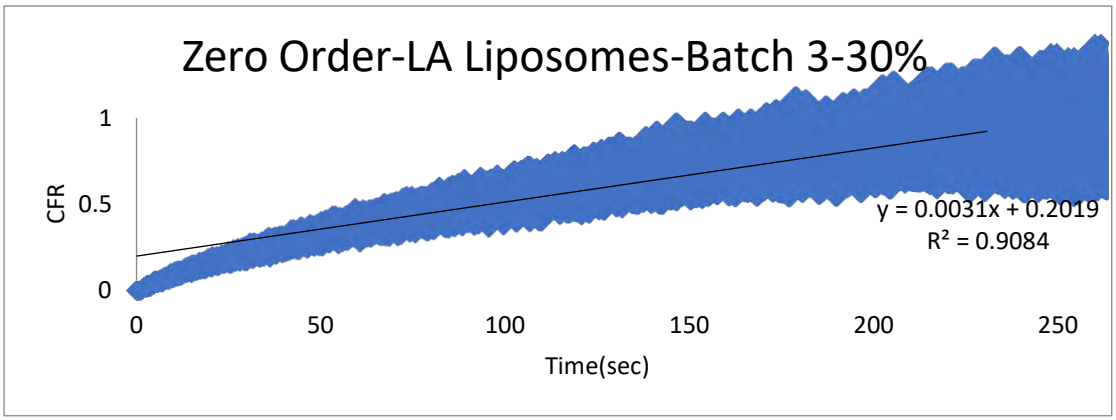

Figure 186:Zero Order model applied on LA liposomes for a power intensity of 17.31 mW/cm^2

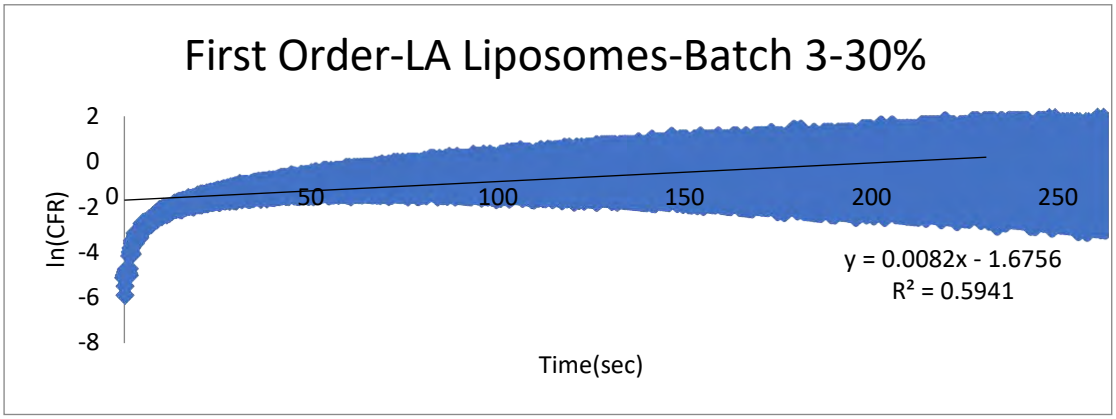

Figure 187:First Order model applied on LA liposomes for a power intensity of 17.31 mW/cm^2

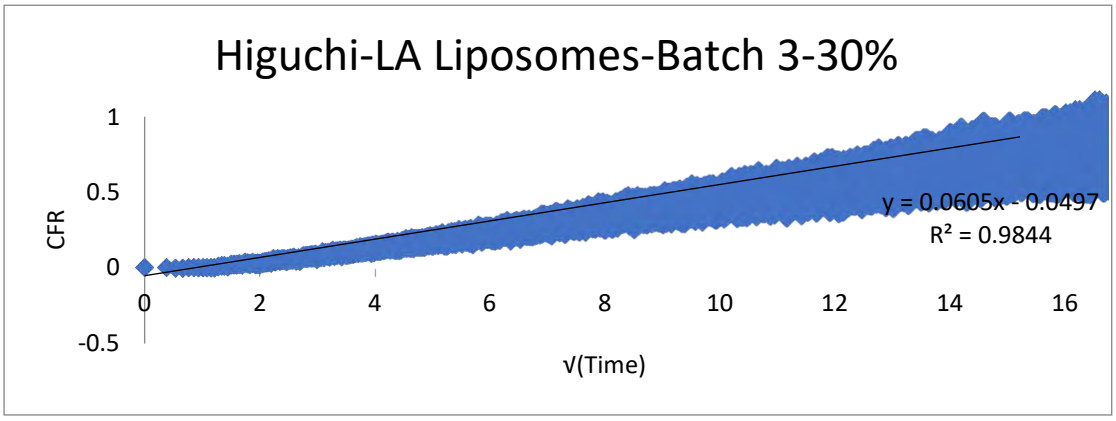

Figure 188:Higuchi model applied on LA liposomes for a power intensity of 17.31 mW/cm^2

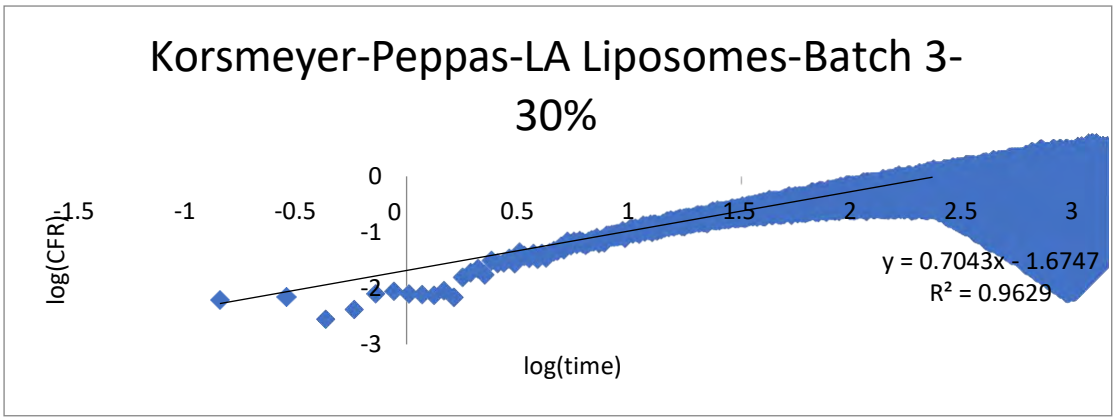

Figure 189:Korsmeyer-Peppas model applied on LA liposomes for a power intensity of 17.31 mW/cm^2

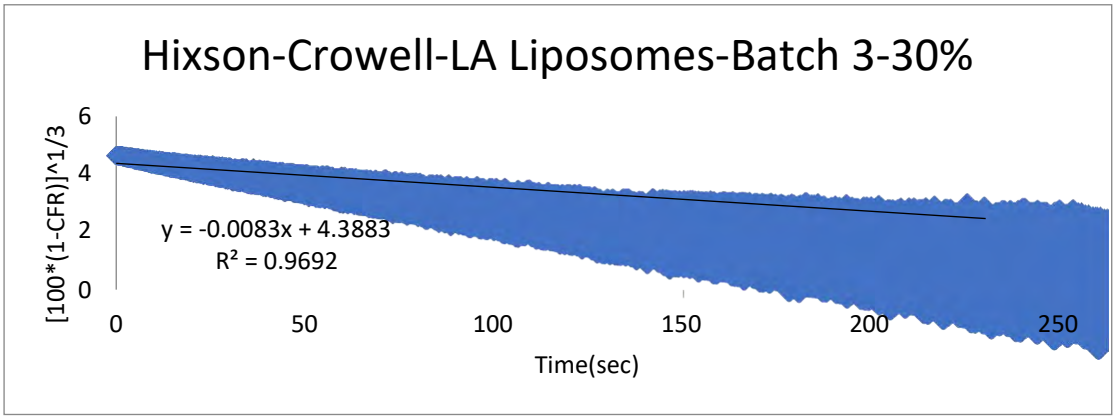

Figure 190:Hixson model applied on LA liposomes for a power intensity of 17.31 mW/cm^2

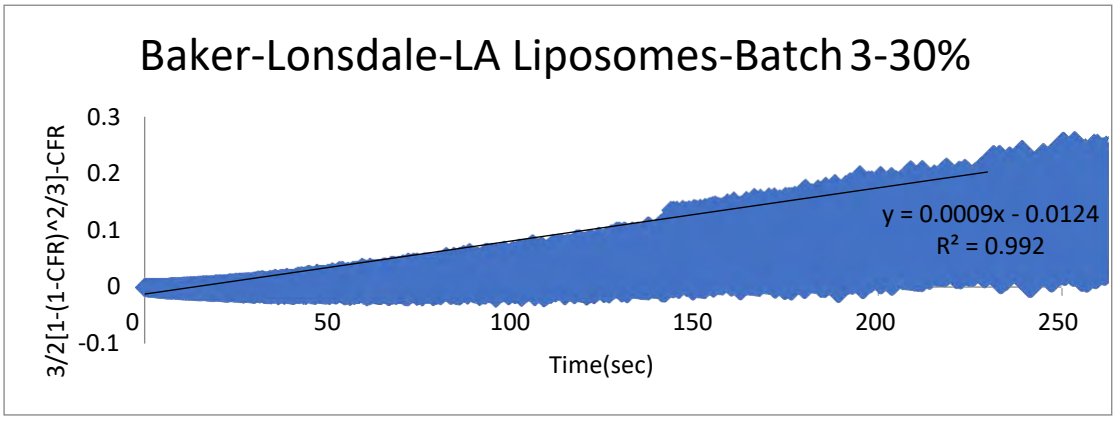

Figure 191:Baker-Lonsdale model applied on LA liposomes for a power intensity of 17.31 mW/cm^2

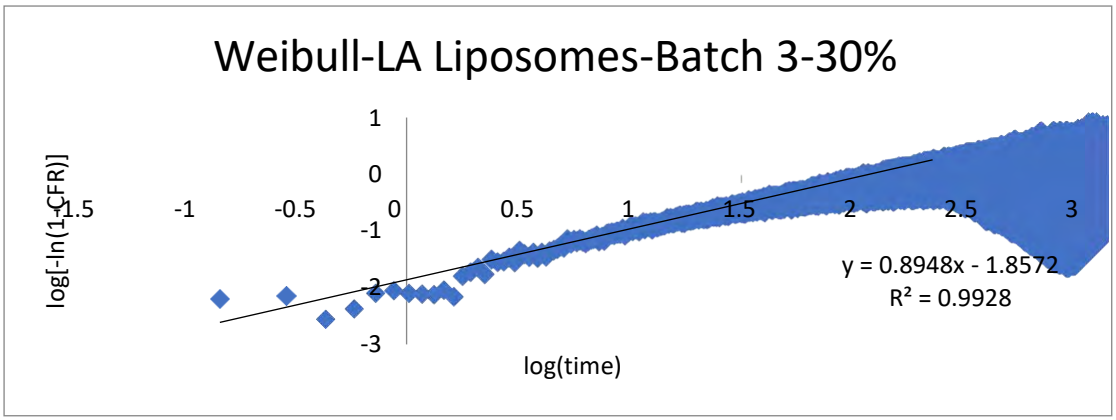

Figure 192:Weibull model applied on LA liposomes for a power intensity of 17.31 mW/cm^2

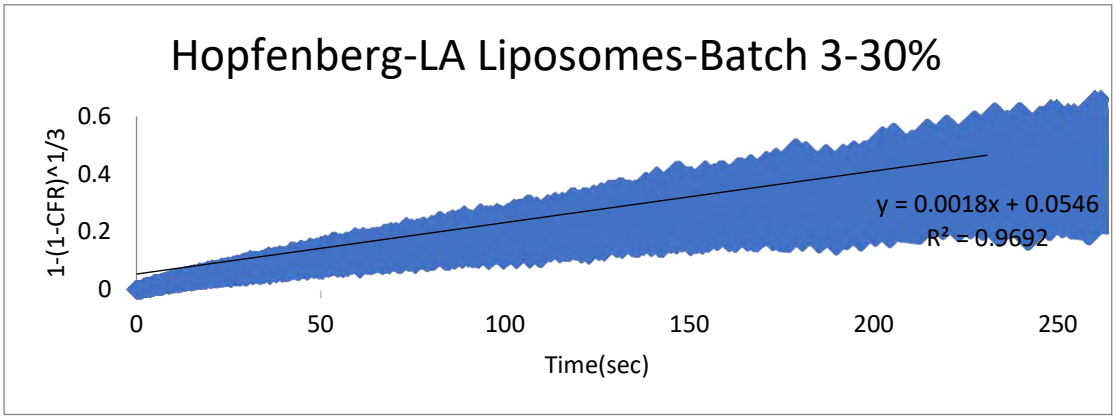

Figure 193:Hopfenberg model applied on LA liposomes for a power intensity of 17.31 mW/cm^2

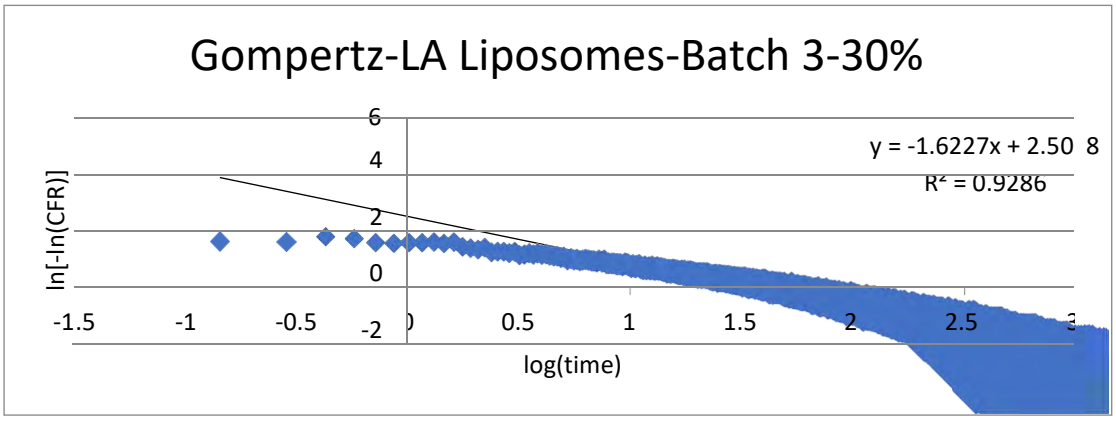

Figure 194:Gompertz model applied on LA liposomes for a power intensity of 17.31 mW/cm^2

Vita

Rand Abusamra, a Jordanian national that was born and raised in Al-Ain, United Arab Emirates. She received her undergraduate Bachelor of Science degree in chemical engineering from the American University of Sharjah in 2012. Next, she gained her professional experience in Hikma Pharmaceutical-Amman, Jordan for 3 years as an Analytical Researcher in the department of Research and Development.

In August 2017, she joined the master's program in Biomedical Engineering at the American University of Sharjah, where she worked as a graduate teaching and research assistant. Her research work and theses focused on the targeted delivery of chemotherapeutics using ultrasound and nanoparticles for cancer treatment.